

Hyperfine Structure of Cs₂ Molecules in Electronically Excited States

Diplomarbeit in der Studienrichtung Physik
zur Erlangung des akademischen Grades Magister der
Naturwissenschaften

eingereicht an der
**Fakultät für Mathematik, Informatik und Physik der
Universität Innsbruck**

von

Oliver Krieglsteiner

Betreuer der Diplomarbeit:

Univ. Prof. Dr. Hanns-Christoph Nägerl

Institut für Experimentalphysik

Innsbruck, November 2011

Abstract

Despite the fact that alkali metal dimers are in the focus of molecular quantum gas research, not much data is available on the hyperfine structure of these molecules in particular for their electronically excited states. Here, we present our approach for a quantitative treatment of the hyperfine structure of the Cs_2 dimer in electronically excited states. The understanding of the hyperfine splitting in conjunction with the knowledge of the selection rules for optical transitions is of importance for the state control of molecules.

In the thesis, the theory needed to understand and perform the calculations is described as well as a discussion of the results. The main simplification of our approach is that we assume that the molecular hyperfine interactions are determined by the hyperfine interactions of individual atoms, which is the case when the molecules are in vibrational levels near the dissociation limit. Some of our results are important for our absolute ground-state transfer experiment. In this experiment, we transfer ultracold molecules from an initially very loosely bound vibrational level of the electronic ground state to the absolute ground state. To do so, we use a coherent optical process that couples rotational and vibrational states of the electronic ground state to electronically excited states that are strongly mixed by spin-orbit interaction. We center the discussion of our results on the electronically excited states that we exploit for the ground-state transfer. However, our calculations give simultaneously the hyperfine structure for all molecular potentials that are correlated for large internuclear separations to the two-atom state in which one Cs atom is the $6s$ state and the other in the $6p$ state.

Zusammenfassung

Obwohl Moleküle aus Alkalimetallatomen eine wichtige Stellung im Forschungsgebiet der molekularen Quantengase einnehmen, ist ihre Hyperfeinstruktur bisher nur spärlich erforscht worden. Vor allem auf die Behandlung der Hyperfeinstruktur von elektronisch angeregten Zuständen ist nur wenig eingegangen worden. Im Rahmen dieser Arbeit präsentieren wir unseren Ansatz zur Beschreibung der Hyperfeinstruktur von elektronisch angeregten Zuständen des Cs_2 -Moleküls. Durch ein besseres Verständnis der Hyperfeinstruktur wird eine feinere Kontrolle der Molekülzustände möglich.

In dieser Diplomarbeit erklären wir die Theorie hinter unseren Näherungen, die Rechnungen und diskutieren unsere Resultate. Unsere Berechnungen bauen auf der Annahme auf, dass die molekularen Hyperfeinwechselwirkungen durch die Hyperfeinwechselwirkungen in den einzelnen Atomen, aus denen die Moleküle zusammengesetzt sind, bestimmt werden. Einige unserer Resultate sind für unser Grundzustandstransfer-Experiment von Bedeutung. In diesem Experiment führen wir durch einen kohärenten Prozess den Zustand von anfänglich schwach gebundenen Cs_2 -Molekülen in den absoluten Grundzustand über. Dabei werden Schwingungs- und Rotationszustände aus dem elektronischen Grundzustand mit elektronisch angeregten Zuständen gekoppelt. In der Diskussion unserer Resultate setzen wir den Schwerpunkt auf die in diesem Grundzustandstransfer verwendeten elektronisch angeregten Zustände. Wir haben aber auch die Hyperfeinstruktur der anderen elektronisch angeregten Zustände berechnet, deren Molekülpotentiale für große Kernabstände mit dem selben Dissotiationlimit, i.e. ein Atom im $6s$ Zustand das andere im $6p$ Zustand, korrelieren.

Contents

1	Introduction	6
1.1	Applications of Cold and Ultracold Molecules	7
1.2	Production of Cold and Ultracold Molecules	9
1.3	The Ground-State Transfer Experiment and the Molecular Hyperfine Structure of Cs ₂ Molecules	11
1.4	Hyperfine Structure of Cs ₂ Molecules in Electronically Excited States	17
2	Theory	20
2.1	Angular Momenta in Quantum Mechanics	20
2.1.1	Orbital Angular Momentum	20
2.1.2	General Form of Angular Momenta	21
2.1.3	Coupling of Angular Momenta	22
2.2	The Cesium Atom	27
2.3	Description of Diatomic Molecules	28
2.3.1	The Diatomic Molecule	29
2.3.2	The Adiabatic or Born-Oppenheimer Approximation	31
2.3.3	Electronic States and Electronic Potentials	33
2.3.4	Labeling of Electronic States	36
2.3.5	Nuclear Motion	41
2.4	Hund's Coupling Cases	43
2.4.1	Hund's Coupling Case <i>a</i>	44
2.4.2	Hund's Coupling Case <i>c</i>	45
2.4.3	Extensions of Hund's Coupling Cases	45
2.5	Spin-Orbit Interaction	46
2.5.1	Spin-Orbit Interaction in Cs ₂	48
2.6	Molecular Hyperfine Structure	51
2.6.1	Hyperfine Structure of Homonuclear Diatomic Molecules	51
2.6.2	Calculation of the Matrix Elements	54
2.6.3	Approximate Matrix Elements	54
3	Model	57
3.1	Hamiltonian	57
3.1.1	Hyperfine and Spin-Orbit Interactions	57
3.1.2	H_0 , the Electronic Hamiltonian	59
3.1.3	Diagonalization of the Complete Hamiltonian H_e	61
3.2	Calculation of the Hyperfine Splitted Adiabatic Potentials	62
4	Results and Discussion	63
4.1	Calculations without Hyperfine Interactions	63
4.2	Hyperfine Structure in the Long-Range Region	68
4.3	Hyperfine Structure in the Short-Range Region	73
4.3.1	Investigation of the Hyperfine Structure at $R = 12a_0$	74

4.3.2	Focus on $(A - b)0_u^+$ System	78
4.3.3	Maximum Splitting	84
5	Perspectives	89
5.1	Variable Spin-Orbit Interaction	89
5.2	Calculation of the Hyperfine Structure of Vibrational Levels	90
5.3	Inclusion of Rotation and Magnetic Fields into the Calculations	91
5.4	Comparison of the Results of the Model with Spectroscopic Data	92
6	Appendix	94
6.1	Additional Relative Hyperfine Plots	94

1 Introduction

The research field of molecular quantum gases is one of the hot topics of today's physics research. Cold and ultracold molecules have the potential to revolutionize physics and chemistry. Cold molecular gases are of great interest in high precision measurements in which one searches for a possible permanent electrical dipole moment of the electron [1] or one tries to test for a time variation of fundamental constants [2, 3, 4, 5, 6]. Ultracold molecular gases open up the field of (quantum-)controlled chemistry [7]. The hope is to prepare molecules in well defined quantum states and to open or close chemical reaction channels via external fields. Furthermore, ultracold molecular quantum gases make new investigations in the domain of matter-wave physics and many-body physics possible. A special focus is set on ultracold polar molecules that possess large permanent electrical dipole moments. These hold the promise to allow the study of yet uninvestigated quantum phases and quantum phase transitions [8] and it is expected that polar molecules will be exploited in quantum information science [9, 10, 11]. For review articles of the rapidly growing field of cold and ultracold ¹ molecules the reader is referred to Ref. [12, 13, 14, 15]

Until today, most ultracold matter experiments have been performed on samples of ultracold atoms. Laser cooling in combination [16] with evaporative cooling [17] and trapping by magnetic and light fields have made it possible to reach high phase-space densities with atomic samples. Examples for pioneering experiments with ultracold atoms are the formation of Bose-Einstein condensates (BECs), almost simultaneously by Anderson et al. (1995) [18] and Davis et al. (1995) [19], and the fundamental investigations of the intriguing properties of BECs. Such as, the superfluid character, which was tested by the formation of vortex lattices in rotating BECs [20, 21] and the macroscopic matter-wave character of BECs, as exemplified by interference patterns for colliding BECs [22]. A further highlight from the first years of ultracold quantum gas research was the formation of degenerate atomic Fermi gases [23, 24, 25]. A fascinating prospect of research activities on atomic Fermi gases was the possibility to observe the Bardeen-Cooper-Schrieffer (BCS) state [26, 27]. Probing and understanding the BCS state is of great importance because BCS theory serves as the foundation of our understanding of superconductivity in metals and of superfluidity in ³He.

A major reason for the importance of research on ultracold quantum gases for many- and few-body physics is given by the fact that ultracold quantum gases can be controlled and manipulated with extraordinary precision. Feshbach resonances (FR) [28] are one of the most important tools that enable this control. By the use of FRs it becomes possible to tune atomic interactions and to create samples of weakly bound Feshbach molecules [29]. A breakthrough in the area of many-body physics was made by the observation of the BEC-BCS crossover [30, 31]. Using a FR in a degenerate atomic Fermi gas, it was possible to create BECs of very loosely bound dimer molecules on the

¹The distinction whether a gas is considered ¹ cold or ultracold is roughly given by the following rule of thumb: a gas is cold if its temperature is around and below 1 mK and it is ultracold if its temperature is around or below some μK .

repulsive side of the FR [32]. In addition, it was possible to form the BCS state on the attractive side of the FR and to observe the smooth crossover between the two states (BEC-BCS crossover). In the domain of few-body physics, FRs also provide a unique tool for investigations. For instance, the combination of ultracold atoms and FR makes it possible to study properties of three-body Efimov states [33]. In our experiment, FRs play a leading role. We use a FR to create Feshbach molecules from a Cs BEC.

Another important tool for quantum gas control and manipulation are optical lattice potentials [34]. Optical lattice potentials are used in order to produce periodic potentials for particles. Ultracold quantum gases loaded into an optical lattice can serve as quantum simulators for many-body physics. One of the most famous physical systems that was realized with ultracold atoms in an optical lattice is the Bose-Hubbard (BH) model [35]. The BH model describes the hopping of bosonic atoms between the lowest vibrational states of the lattice sites. Essentially, two parameters determine the many-body state: The hopping matrix element J given by the kinetic energy and the depth of the lattice and the on site interaction U (the repulsion between the atoms). By variation of the ratio of J and U (for example by variation of the lattice depth) one can drive a phase transition from a superfluid (SF) phase to a Mott-insulator (MI) phase. In the SF phase the atoms are delocalized over the lattice. In the MI phase every lattice site is occupied with the same number n (for $n = 1, 2, 3, \dots$) of atoms. If an external trap is superimposed on the optical lattice, a series of MI domains with different n values separated by SF regions can be observed [36]. The first who observed the superfluid-to-Mott-insulator phase transition on ultracold atoms in a three dimensional optical lattice were Greiner et al. (2002) [37]. Later the transition was observed also in one and two dimensions [38, 39] and for fermionic atoms [40]. We are also exploiting an optical lattice in our ground-state transfer experiment. We use the optical lattice to produce a Mott-insulator state with two atoms per lattice cite ($n = 2$).

1.1 Applications of Cold and Ultracold Molecules

In current research one is trying to extend the experiments on ultracold matter from atomic to molecular gases. Molecules greatly enrich the range of quantum gas applications because they have properties that are not found in atoms. In addition to the molecular electronic structure and the molecular fine and hyperfine structure, which have their counterparts in the atomic energy structure, molecules can rotate and vibrate. For example, these additional degrees of freedom are important in tests of fundamental physical laws [1, 2, 3, 4, 5, 6]. Furthermore heteronuclear molecules typically have permanent electrical dipole moments that are much larger than the dipole moments of atoms. (An exception are atoms in Rydberg states, which also have a very large electrical dipole moment [41] but low lifetimes.) Such polar molecules are then subject to dipole-dipole interactions that is anisotropic and of long-range character. Molecules should thus, in contrast to atoms, for which interactions are isotropic and short range, allow the study of new phases in many-body physics [8, 42, 43] and new quantum computing schemes [9, 10, 11].

At low and ultralow temperature thermal perturbations are reduced to a minimum. Therefore, molecular spectroscopy with ultrahigh resolution becomes possible, helping to improve our knowledge of molecular structure and molecular dynamics. An important application of ultrahigh resolution spectroscopy lies in tests of fundamental physical laws

[1, 2, 3, 4, 5, 6]. For example, spectroscopy of rotational and vibrational (rovibrational) levels might contribute to answering the question whether fundamental constants are indeed *constant* [44]. It is possible that the values of fundamental constants vary with time. Accurate measurements on rovibrational spectra of ultracold molecules can help answering this question for the fine structure constant α and the electron-proton mass ratio μ . For example, some rovibrational levels are very strongly affected by changes of μ and others not. Comparison of the frequencies for transitions into strongly and weakly affected rovibrational levels would be a possible measurement that can detect a change of μ . Another test of fundamental physics is the search of a possible electric dipole moment of the electron [1]. It is thought that measurements on the electric dipole moment of the electron can help to understand the difference in amount of matter to antimatter. When an external electrical field is applied to an atom or a molecule the effect of the field on the dipole moment of the electron would be strongly enhanced by relativistic effects. This enhancement is much stronger in polar molecules than in atoms. Spectroscopy of rovibrational levels of heavy polar molecules should be many orders of magnitude more sensitive to the electron dipole moment than atomic spectroscopy.

Further applications for ultracold molecules originate from the prospect of quantum-controlled chemistry [7, 13]. With almost perfect control of the external and internal degrees of freedom, it will be possible to prepare ultracold molecules in well defined quantum states. Thus, one can observe how the chemical reactions are modified by state preparation at ultralow temperatures. For example, Ospelkaus et al. (2010) [45] recently investigated chemical reactions of ultracold fermionic $^{40}\text{K}^{87}\text{Rb}$ molecules. They observed that quantum statistics and tunneling through angular momentum barriers play a crucial role in the reactions of ultracold molecules. When the molecules were prepared in different hyperfine states reaction rates were very high. However, just a tiny modification of the molecular state, namely a flip of the nuclear spin of the Rb nucleus so that the molecules were identical fermions, led to a decrease of the chemical reaction rate by a factor of 10-100. The reaction rates were reduced by the angular momentum barrier that arises from Pauli blocking. It is also important to point out, that even in the case of identical fermions the reaction rates were still quite high since the molecules are able to tunnel through the barrier. In addition to the precise state preparation prospects, it will also be possible to control the possible reaction channels by application of electric, magnetic, and light fields.

The large permanent electric dipole moment of polar molecules is of interest in quantum information science and in quantum simulation science. Polar molecules trapped in optical lattice potentials can be used as qubits for quantum information processes [9, 10, 11]. Polar molecules can be stored in scalable systems and are expected to have good coherence properties. Quantum simulators could be used instead of computer calculations to simulate quantum mechanical problems. The idea is to directly build a Hamiltonian that matches the properties of another Hamiltonian of interest, whose properties are not fully understood. The re-built Hamiltonian can then give insights similar to computer simulations. The long-range, anisotropic dipolar interactions expand the range of Hamiltonians that can be modeled. For example, polar molecules in optical lattices can be used to model spin systems [43, 46]. An extended Bose-Hubbard Hamiltonian in which not only nearest neighbor interactions but also next nearest neighbor interactions are taken into account can possibly also be modeled with polar molecules in optical lattices [8]. Further prospects for cold and ultracold molecules can be found in reviews like [13, 14, 15].

1.2 Production of Cold and Ultracold Molecules

At the present, there are several procedures tested to create samples of cold and ultracold molecules that are dense enough for the various applications. A quantity that characterizes a gas simultaneously by its temperature and density is the phase-space density D , given by the formula $D = n\lambda_T^3$. Here, n is the number density and $\lambda_T = (2\pi\hbar^2/mk_B T)^{1/2}$ is the thermal de Broglie wavelength, which determines the average extension of the particles wave packets in thermal equilibrium. For $D \approx 1$ and higher, one speaks of a quantum gas or the regime of quantum degeneracy. Generally, one intends to have a high phase-space density. But, in many aspects the control of the external degrees of freedom of molecules and consequently of phase-space density is an unsolved problem.

The difficulties mainly result from the complex internal structure of molecules. Firstly, the complex internal structure makes the use of laser cooling an almost impossible task. Excited molecular states can decay into many lower lying states and thus closed cooling cycles are hard to find. However, for a specific diatomic molecule laser cooling of the motional states has recently been demonstrated [47], but the phase-space densities that are achieved in this way are negligible. The second difficulty, is the fact that molecules in rovibrationally excited states are very sensitive to collisional relaxation. It is very likely that, as a result of a collision, rovibrationally excited molecules change their state to a lower lying rovibrational state. The released energy increases the kinetic energy of the molecules. The effect generally is heating and trap loss. It is certainly a limiting factor for the production of dense and ultracold molecular samples. Especially, in production schemes of molecular quantum gases one has to avoid collisional relaxation. Collisional relaxation reduces n and λ_T . Furthermore, it increases the overall number of internal molecular states that are populated. This is very cumbersome for the production of degenerate gases because preferably only one state should be populated. One can suppress collisional relaxation if one transfers the molecules to the absolute ground state i.e. the lowest hyperfine state of the rotational, vibrational and electronic (rovibronic) ground state. However, the complex structure of molecules, with its myriad of close lying molecular energy levels, makes it very difficult to prepare molecules in the absolute ground state. An exceptional case of suppression of collisional relaxation is given by loosely bound dimer molecules, where the components of the molecules are fermions of the same species. Here, the Pauli blocking stabilizes the molecules against collisional relaxation [48]. BECs of vibrationally highly excited Feshbach molecules have been produced in Innsbruck [32] and Boulder [25].

There exist several approaches that aim at the efficient production of cold and ultracold molecules and try to overcome the difficulties of laser cooling. Generally, one distinguishes between direct cooling methods and indirect cooling and deceleration methods. In direct methods one *directly* cools molecules whereas the indirect methods rely first on the production of ultracold atoms. The ultracold atoms are then associated to ultracold molecules. Thus, ultracold molecules are gained *indirectly*. In deceleration techniques one slows the particles of a beam of cold molecules down.

In Stark [49] and Zeeman [50] deceleration schemes, rapidly switching electric or magnetic fields are applied to a supersonic beam of molecules to slow the beam particles down. In the moving frame of the beam the temperature of the beam is on the order of 1 K. If the beam is slowed down, one obtains a sample of rather cold molecules.

A prominent example of a direct cooling technique is the buffer gas cooling technique. A pioneering experiment is for instance detailed in Ref. [51]. In this technique, pre-cooled atoms collide with hot molecules. By thermalization of the molecules with the cold atoms the molecules simply become colder. Afterwards one separates the molecules from the atoms by magnetic and electric guiding fields.

The photoassociation (PA) technique and the Feshbach association (FA) technique belong to the indirect cooling techniques. In PA experiments a photon is absorbed by two colliding ultracold atoms. By absorption of the photon, the atom pair is bound to a molecule in an electronically excited state. Some of the molecules spontaneously decay into bound levels of the electronic ground-state potentials and form stable ultracold electronic ground-state molecules. Such a process is also called a one-color PA process. The first samples of ultracold cesium dimers were produced at the Laboratoire Aimé Cotton (Orsay, France) by the PA technique [52]. The efficiency of PA experiments depends on the overlap of vibrational states in the electronically excited potential and in the electronic ground-state potential. Often good overlap is obtained by employing special properties of electronic potentials. For example, the existence of purely long-range vibrational states [53] and resonant coupling [54], which are consequences of spin-orbit interaction, increases the efficiency of PA experiments. Two-color PA processes are coherent and use stimulated Raman transitions to produce molecules. Two color PA has also been successfully demonstrated [55].

Today, the technique that produces the highest value of phase-space density is the Feshbach-association technique. For this technique even the regime of quantum degeneracy is in reach. In the FA technique magnetic fields are used to tune the relative energy between bound molecular states and the state of colliding atoms (see figure 1.1). This is possible when the magnetic moments of the two states are different. If coupling is also allowed between the two states, a FR occurs when the relative energy is tuned to zero. By adiabatically tuning the magnetic field over the FR, one can associate ultracold atoms to weakly bound but translationally ultracold molecules. Evidence for the first production of Feshbach molecules was reported in Ref. [29] and a review on the whole topic of FR and FA is given by Ref. [28].

This diploma thesis is embedded in a research project investigating techniques for the production of quantum gases of ultracold ground-state molecules. The central idea is to associate molecules from an atomic BEC that already possesses high phase-space density, to preserve the high phase-space density for the molecular sample and subsequently transfer the molecules to the absolute ground state in order to produce a ground-state molecular BEC (mBEC). Specifically, an ensemble of Cs_2 molecules in the lowest hyperfine state of the rovibronic ground state ($\nu = 0$, $N = 0$) shall be put in the state of an mBEC. In the limit of weakly bound molecules, the production of an mBEC was already demonstrated [32, 57]. In contrast, the production of ground-state mBECs requests additional efforts because Pauli blocking is not assuring collisional stability, as is the case for Feshbach molecules composed of fermions [32, 57]. The production of a tightly bound mBEC has not been reported yet. In our experiment, ultracold atoms of a Cs BEC are transferred by the use of an optical lattice to a Mott-insulator state. The atoms are then associated by FA to Cs_2 Feshbach molecules. The Feshbach molecules are then coherently transferred to the absolute ground state by exploiting the stimulated Raman adiabatic passage (STIRAP) technique [58]. The experiment serves as a proof-of-principle demonstration that shows that the production scheme followed by us can indeed be used to produce molecular ground-state BECs. It serves as a testbed

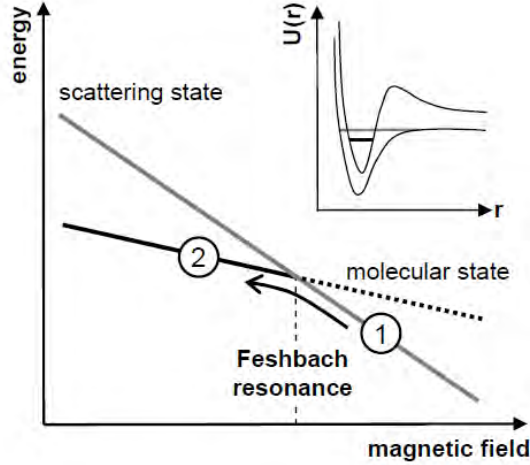


Figure 1.1: **Energy diagram for the state of the colliding atoms and the molecular bound state.** By variation of the magnetic field B the energy difference of the bound molecular state and the state of the colliding atoms can be tuned to zero. The atoms in (1) are associated to the molecular state (2) by sweeping the magnetic field downwards across the resonance. Figure is taken from Ref. [56]

for the production of molecular quantum gases that are formed out of polar molecules. A similar production scheme for a ground-state mBEC of polar molecules is evidently more complicated because one has to deal with the more complex situation of mixing two different atom species. Despite this fact, the route of mixing two species is already followed by our group in Innsbruck [59, 60] and by the group around D.S. Jin and J. Ye [61]. In the next section we explain the ground-state transfer experiment and highlight the relevance of this diploma thesis.

1.3 The Ground-State Transfer Experiment and the Molecular Hyperfine Structure of Cs_2 Molecules

The procedures of the experiment are summarized in figure 1.2 and detailed in Ref. [62] and Ref. [63].

The first step is to cool and trap Cs atoms to produce a cesium BEC. The BEC is then loaded into an optical lattice potential by adiabatically switching on the lattice. The frequency of the lattice light is far detuned from atomic resonances. In this way heating by the lattice light is kept at a minimum. The lattice depth is increased to drive the superfluid-to-Mott insulator phase transition. Due to the effect of the confining trapping potential not all atoms are put into MI phase. MI regions of different occupation number are separated by atoms in the SF phase. The situation for our set-up is illustrated in figure 1.3.

In the center of the trap we produce a MI region with $n = 2$ surrounded by a SF phase, then a MI region with $n = 1$ and again a SF phase. We adjust the lattice and the external trap parameters to optimize the population of the two-atom Mott shell. Experimentally, we find that we can populate 45% of the lattice sites with exactly two

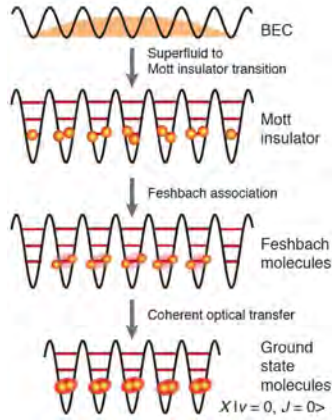


Figure 1.2: **Experimental procedure for the ultracold molecule production.** A BEC of Cs atoms is loaded into an optical lattice potential. Then the superfluid-to-Mott insulator phase transition is driven by increasing the depth of the lattice. By Feshbach association, weakly bound molecules are produced. They are then coherently transferred to the rovibrational ($\nu = 0, N = 0$) ground state of the lowest electronic state $X^1\Sigma_g^+$ using the STIRAP technique. Figure taken from Ref. [63]

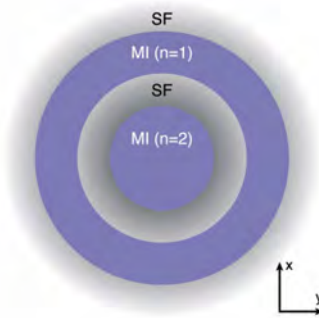


Figure 1.3: **Schematic illustration of particles in the ground state of an optical lattice with a superimposed external trap.** The external trap and the lattice is adjusted in such a way that in the center a Mott insulator with two atoms ($n = 2$) per lattice site is created. On going toward the edge of the particle sample a series of superfluid and Mott insulating domains occur. In our experiment we try to maximize the region in the center. Figure is taken from Ref. [36]

atoms, close to the theoretical limit of 53% given by the harmonic, non-homogeneous initial conditions [64].

Following again figure 1.2, the next experimental step is to associate the atoms to molecules. We apply a magnetic field ramp to exploit a FR in order to bind the Cs atoms to Cs_2 Feshbach molecules. The associated atom pairs are kept at the individual lattice sites where they populate the vibrational ground state of the lattice site. Since the molecules rest at the sites and are not hopping, the optical lattice shields the Feshbach molecules against disruptive collisional relaxation.

In a final stage of the experiment, we intend to remove the lattice in order to produce an mBEC state [65]. However, if we removed the lattice, the molecules could undergo collisional relaxation processes. Therefore, we first transfer the molecules to the absolute ground state, which is collisionally stable and then remove the lattice. The transfer is made by application of the STIRAP technique with which we coherently transfer the Feshbach molecules to a specific hyperfine state of the rovibronic ground state that is characterized by the quantum numbers $|I = 6, m_I = 6\rangle$. (I stands for the total nuclear spin and m_I is its projection on the direction of the magnetic field.) The Zeeman splitting of the hyperfine states of the rovibronic ground state ($\nu = 0, N = 0$) can be seen in figure 1.4. The addressed state $|I = 6, m_I = 6\rangle$, colored in red, becomes the absolute ground state when the magnetic field B is increased to $B \approx 13$ mT.

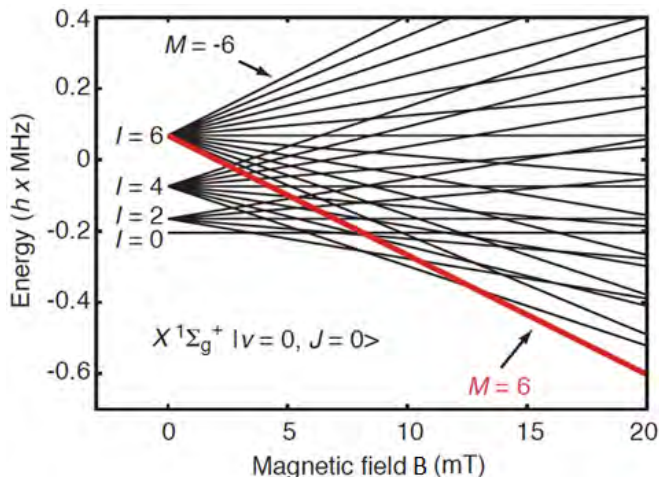


Figure 1.4: **Zeeman splitting of the hyperfine states of the rovibronic ground state** ($\nu = 0, N = 0$). The STIRAP process transfers the molecules to the $|I = 6, m_I = 6\rangle$ hyperfine state (I stands for the total nuclear spin and m_I is its projection on the direction of the magnetic field.) of the rovibronic ground state (indicated in red). At magnetic field strengths of approximately 13 mT, this hyperfine state becomes the absolute ground state. Figure is taken from Ref. [63]

The standard STIRAP process involves three states: an initial state $|i\rangle$, a final state $|f\rangle$, and an intermediate excited state $|e\rangle$ that has a finite lifetime $1/\Gamma$. We assume that the states $|i\rangle$ and $|f\rangle$ are stable. Their lifetimes are large compared to the duration of the STIRAP transfer. We illustrate the STIRAP principle in figure 1.5. For a review on coherent population transfers see Ref. [58].

Two lasers are used to couple the three states in a Λ -type configuration. Due to the coupling a so-called dark state $|d\rangle = \cos\theta|f\rangle - \sin\theta|i\rangle$ is formed. The angle θ is given by $\tan\theta = \frac{\Omega_1(t)}{\Omega_2(t)}$, where $\Omega_1(t)$ and $\Omega_2(t)$ are the time dependent Rabi frequencies of

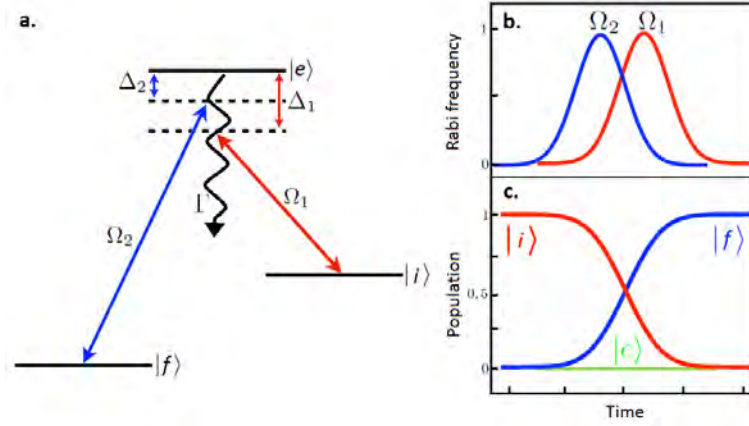


Figure 1.5: **Illustration of the standard STIRAP process.** **a.** The three states $|i\rangle$, $|f\rangle$, and $|e\rangle$ are coupled in a Λ -type configuration by the lasers L_1 and L_2 . Δ_1 and Δ_2 are the single-photon detunings of laser 1 and 2 respectively. Γ indicates decay processes from state $|e\rangle$. **b.** Rabi frequencies corresponding to laser 1 and 2 as a function of time. In a counterintuitive pulse scheme, first laser 2 is switched on and after a certain time laser 1. **c.** State population during the process. Note that the excited state $|e\rangle$ is never populated. Figure is adapted from Ref. [66]

laser 1 coupling the state $|i\rangle$ and $|e\rangle$ and the laser 2 coupling the state $|e\rangle$ and $|f\rangle$. The dark state has no admixture of the excited state and can therefore not decay during the transfer period. The Rabi frequencies are varied in a counterintuitive way as shown in figure 1.5. First, laser 2 is switched on and then after a short delay laser 1 while laser 2 is switched off again. As a consequence of this pulse sequence the dark state is coherently rotated from purely initial to purely ground state character with a maximum theoretical efficiency of 100%. To optimize the efficiency of the STIRAP, two conditions have to be fulfilled. Condition (i) the two-photon resonance condition $\Delta_1 = \Delta_2$ has to apply. Δ_1 (Δ_2) is the detuning of laser 1 (2) from the transition frequency between state $|i\rangle$ and $|e\rangle$ ($|e\rangle$ and $|f\rangle$). (ii) The criterion of adiabaticity $\tau\Omega^2 \gg (2\pi)^2\Gamma$, where τ is the transfer time and $\Omega \approx \Omega_1 \approx \Omega_2$ has to be fulfilled. Thus, the Rabi frequencies have to be as large as possible and the transfer time long. However, an upper limit for the transfer time is given by the coherence time of the laser.

In Cs_2 no three levels are known to provide sufficient wave function overlap for a direct STIRAP transfer from the Feshbach-molecule state to the absolute ground state. The difference in the average extension of the loosely bound Feshbach molecules and the tightly bound ground-state molecules is too large. Instead of the three states of the standard STIRAP, we use five states, where always two states have a wave function overlap that is good enough for a transfer. The five states that are used in our ground-state transfer are illustrated in figure 1.6. Three states ($|1\rangle$, $|3\rangle$ and $|5\rangle$) belong to the electronic ground-state potential and two belong to the electronically excited potentials ($|2\rangle$ and $|4\rangle$). State $|1\rangle$ is the initial Feshbach-molecule state. State $|3\rangle$ is an intermediate rovibrational state of the $X^1\Sigma_g^+$ potential with quantum numbers ($\nu = 73, N = 2$) and state $|5\rangle$ is the rovibronic ground state $X^1\Sigma_g^+$ ($\nu = 0, N = 0$). The states $|2\rangle$ and $|4\rangle$ are rovibrational states of the coupled $(A - b)0_u^+$ system. This system is formed by spin-orbit coupling of the $A^1\Sigma_u^+$ and the $b^3\Pi_u$ electronic potentials. State $|2\rangle$ has quantum numbers ($\nu = 225, N = 1$) and $|4\rangle$ has quantum numbers ($\nu = 61, N = 1$). The coupling is of high importance. The Feshbach molecules are predominantly formed in the $a^3\Sigma_u^+$

potential. Spin-orbit coupling allows the transfer of molecules from singlet to triplet potentials, which would be forbidden otherwise. Moreover, the avoided crossing that occurs as a result of the spin-orbit coupling (see figure 1.6) increases the probability for a state transfer into deeply bound rovibrational states of the electronic ground state. The five states are coupled by four lasers with time dependent Rabi frequencies Ω_1 , Ω_2 , Ω_3 , and Ω_4 .

Two transfer schemes are possible. One transfer scheme is the sequential STIRAP (s-STIRAP) the other one is the four-photon STIRAP (4p-STIRAP). With s-STIRAP the molecules are transferred with a standard STIRAP process from $|1\rangle$ to $|3\rangle$ and with an additional standard STIRAP process from $|3\rangle$ to $|5\rangle$. In a 4p-STIRAP all five states are coupled in one step by the four lasers in a distorted M-type configuration as indicated in figure 1.6. Thus, the dark state is formed by a superposition of the states $|1\rangle$, $|3\rangle$, and $|5\rangle$ and has the form $|d\rangle = (\Omega_2\Omega_4|1\rangle - \Omega_1\Omega_4|3\rangle + \Omega_1\Omega_3|5\rangle)/A$ where A is a time dependent normalization factor. By variation of the four Rabi-frequencies Ω_i in a counterintuitive way similar to the standard STIRAP process, the initial state $|1\rangle$ is adiabatically rotated into the final state $|5\rangle$ [67]. The time-dependent variation scheme of the Rabi-frequencies for the 4p-STIRAP is illustrated schematically in figure 1.6 for a transfer from the Feshbach-molecule state to the rovibrational ground state and (after a hold time τ_h) back. We transfer the molecules back to state $|1\rangle$ to determine the efficiency of the STIRAP process by measuring the number of re-occurring Feshbach molecules. We observe that more than 30% of the molecules can be transferred by our set up to the ground state and back [62, 63]. This corresponds to a single pass efficiency of about 60%, assuming that for both transfers we have equal efficiencies.

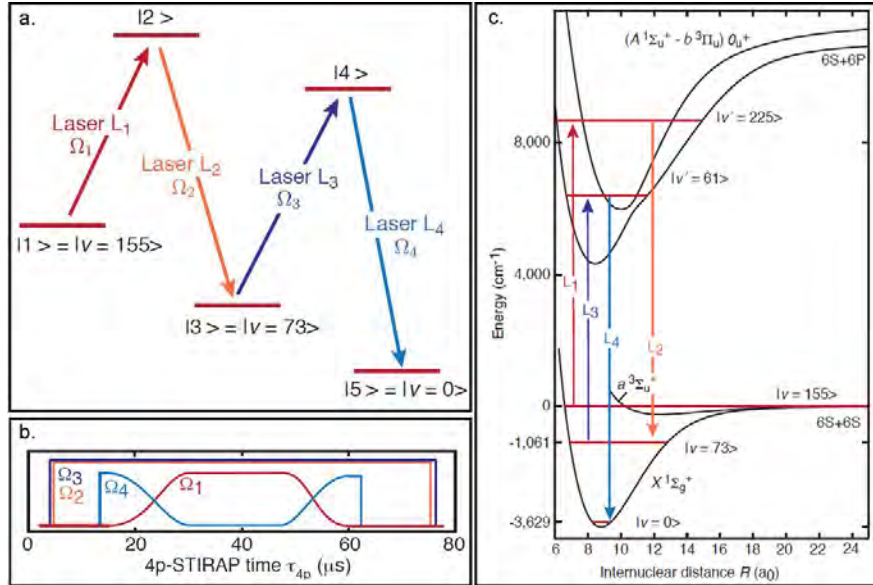


Figure 1.6: **Illustration of the 4p-STIRAP scheme.** **a**) The five rovibrational levels are coupled in a distorted M-type configuration. **b**) Time-dependent variation of the Rabi frequencies that rotates state $|1\rangle$ into state $|5\rangle$ and back. **c**) The five levels are integrated in a plot of the molecular potentials. Figures are adapted from Ref. [63]

The rovibrational states that allow STIRAP transfers with good efficiencies were identified in optical loss spectroscopy [68] and in dark-state spectroscopy [69] experiments. The optical loss spectroscopy is achieved by irradiating the molecules with a laser. After a certain time the number of the remaining molecules is determined. Then one

repeats the experiment with a different frequency. When the laser frequency can excite a transition, the molecules are transferred to this state and subsequently decay. The probability is low to decay into the initial state and thus, they are not contributing when the number of molecules in the initial state is determined (for example by absorption images). This can be observed in the form of loss resonances when one plots the number of molecules in the original state against the laser wavelength/frequency. An example for loss resonances where molecules are excited from the initial state to the $(A - b)0_u^+$ system is shown in figure 1.7.

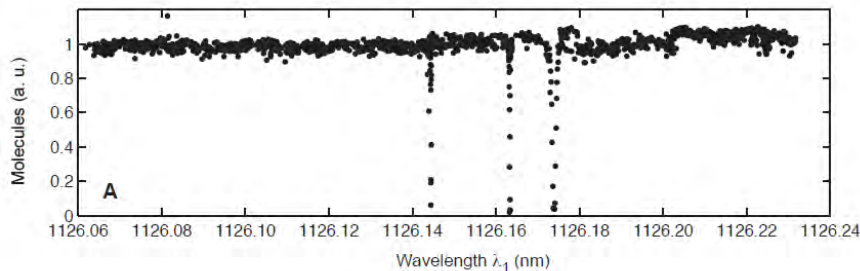


Figure 1.7: **Loss resonances of excitations from the initial Feshbach molecule to rovibrational levels of the $(A - b)0_u^+$ system.** A Feshbach-molecule sample is irradiated with a laser. When the laser frequency matches a transition frequency the number of molecules in the Feshbach-molecule state drops sharply. The figure is taken from Ref. [68]

In dark-state spectroscopy the molecular sample is simultaneously illuminated with two lasers (1 and 2). Like in the standard STIRAP process (see figure 1.5), the two lasers can couple three rovibrational states ($|i\rangle$, $|f\rangle$, and $|e\rangle$) in a Λ -type configuration. The spectroscopy is performed by switching on laser 2 that couples the state $|f\rangle$ to the state $|e\rangle$ and then scanning the frequency of laser 1. Like in the above described loss spectroscopy, one determines the number of the molecules that remain in the initial state after the irradiation. When laser 1 is detuned from the two-photon resonance, molecules are excited and lost by spontaneous emission. On two-photon resonance the molecules are in a dark state formed by the initial state and the final state and remain in the initial state when the lasers are switched off. Thus, a sharp peak becomes visible when the initial molecules are plotted as a function of the detuning of laser 1 from two-photon resonance (see figure 1.8).

For an efficient STIRAP transfer, knowledge of the states involved at the level of the hyperfine structure is needed. Insufficient understanding of the hyperfine structure and of the selection rules for optical transitions can lead to a population transfer into unwanted hyperfine levels. The knowledge of the hyperfine structure of the rovibronic ground state is given by calculations performed by J. Hutson and J. Aldegunde [70]. They use density functional theory to calculate the hyperfine splitting of the lowest and the second lowest rotational levels of the vibrational and electronic ground state for all alkali metal dimers - with and without the presence of external magnetic fields.

The theoretical description of the hyperfine structure of the excited molecular potentials and of the rovibrational state with quantum numbers ($\nu = 73, N = 2$) has not been achieved yet. The aim of this diploma thesis is to start to fill this gap. We give a description of the hyperfine structure of molecular states of the Cs_2 dimer that are correlated at large interatomic distances to a two atom-state with one atom in the ground state $6s$ and the other atom in the excited state $6p$. We refer to these states by

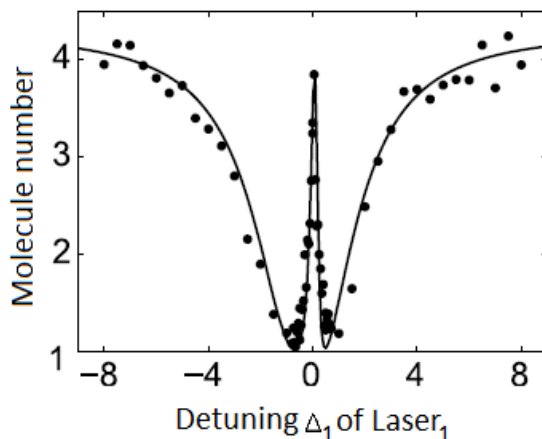


Figure 1.8: **Dark-state resonance involving three rovibrational states ($|i\rangle$, $|f\rangle$, and $|e\rangle$).** As long as laser 1 is detuned from the two-photon resonance, strong loss of molecules is observed. When the two-photon resonance condition is fulfilled, a dark state is formed and the molecules survive in the initial state $|i\rangle$. The figures are adapted from Ref. [69]

$\text{Cs}_2(6s+6p)$. Thus, not only the $(A-b)0_u^+$ system, used in the STIRAP, is investigated. In the same calculation we get simultaneously the hyperfine structure of all $\text{Cs}_2(6s+6p)$ states.

Knowledge of the hyperfine structure is important to correctly interpret the data of high resolution spectroscopy and helps to setup and plan STIRAP processes for state transfer experiments. The maximum splitting of the hyperfine structure is of special importance. Often, spectroscopic experiments cannot resolve the hyperfine structure in all its details. If the hyperfine lines are not resolved, it results in a broadened line equal to the maximum hyperfine splitting. Moreover, if the maximum splittings of calculations and spectroscopic experiments match, it helps to identify the measured electronic states. Additionally, it is a good indication that the measurement has revealed the whole hyperfine structure of a molecular state.

1.4 Hyperfine Structure of Cs_2 Molecules in Electronically Excited States

The hyperfine structure is a consequence of the interaction between electric and magnetic multipoles of a nucleus and electric and magnetic fields created by the electrons and the other nucleus [71]. In the history of hyperfine structure Pauli [72] was the first to propose that a nucleus may have a spin and thus a magnetic moment. The first quantitative theoretical descriptions of the resulting interactions between the electrons and a nucleus were given in the 1930ies (for example by Fermi [73]). In 1952, Frosch and Foley published a very important work on the magnetic interactions between electrons and nuclei in diatomic molecules [74]. M. Broyer et al. presented in 1977 a general derivation of the effective hyperfine Hamiltonian in the case of homonuclear diatomic molecules [71]. We use many points from this text in our treatment of the hyperfine

structure.

The highest energy scales within a molecule are set by the electrostatic interactions of the charged particles. Separations of electronic states are often on the order of 100 to 1000 THz large. The depth of electronic potentials can also be more than 100 THz deep. Smaller in energy scale is the molecular fine structure. The origin of the fine structure is the interaction between the electron spin and the orbital angular momentum in conjunction with relativistic effects. It lifts the degeneracy of electronic states with different electron spin parts. The fine structure of molecules varies between approximately 100 GHz and 10 THz. Due to the hyperfine interactions the degeneracy of the electronic molecular states according to the various orientations of the nuclear spins is lifted. The hyperfine structure splitting varies between approximately 1 MHz and some GHz. As we see, the hyperfine structure is rather tiny compared to the other energies. The term *hyperfine* is chosen because of the hyperfine splittings' tiny magnitudes.

The hyperfine structure is a result of many different interactions, for example magnetic dipole interactions between the electrons and the nuclei or interactions between the electric quadrupole moments of the nuclei. The calculation of the individual parts is very difficult because it requires knowledge of the electronic wave function, which is a function of the internuclear distance. If one knows the electronic wave function, it would in principle be possible to calculate the strength of the interaction for any nuclear separation. However, at the present we lack this ingredient.

Taking this into account, at the very beginning of the treatment of the hyperfine structure we make the simplification that the strength of the hyperfine interactions is determined by the strength of the atomic hyperfine interactions. More accurately speaking, we assume that the wave function of a given diabatic potential can be approximated by linear combinations of products of cesium $6s$ and cesium $6p$ orbitals. Furthermore, we assume that spin-orbit interactions and hyperfine interactions between the compounds of the two atoms are negligible for *any* internuclear separation. Thus, the hyperfine splitting of a single diabatic potential can be obtained from the atomic hyperfine splitting. The hyperfine structure of a single diabatic potential would be constant for any internuclear separation. However, our model allows that diabatic potentials and adiabatic potentials perturb each other. The magnitude of the perturbation depends on the energetic separation of the potentials. Hence, the hyperfine structure splitting of a specific adiabatic potential is a function of the internuclear distance. Our approach provides a rather good approximation for large internuclear separations, but it becomes worse for smaller ones, since in general the molecular interactions and molecular states differ more and more from the separated atom case.

As a result of our investigations, we can calculate the hyperfine structure of the $\text{Cs}_2(6s+6p)$ states. Without fine and hyperfine structure, the $\text{Cs}_2(6s+6p)$ electronic potentials are made up by eight potentials. Spin-orbit interaction partly lifts their degeneracy, resulting in 16 potentials. Our results show further splittings of these 16 potentials due to the inclusion of the hyperfine interactions. The calculations result in 854 distinct adiabatic potentials correlated to the possible energies that can be made up by the energies of a $\text{Cs}(6s)$ atom and a $\text{Cs}(6p)$ atom in their hyperfine states. We show and describe how the potentials emerge from the energies of the $(6s+6p)$ dissociation limits and what effect the increasing electronic interaction has on the general form of the hyperfine potentials. For electronic energies larger than the hyperfine splittings, the

hyperfine potentials form the hyperfine structure of the 16 adiabatic potentials.

We also illustrate in which regions it is not possible to speak of the hyperfine structure of a specific adiabatic potential because two adiabatic potentials come too close to each other and share their hyperfine structures. Moreover, we discuss the magnitude of the hyperfine structure of the various potentials by the use of perturbation theory. Finally, we also look closer at potentials that are used in the ground-state transfer experiment in Innsbruck. We describe and explain the shape of their hyperfine potentials in detail and estimate their maximum hyperfine splitting. This was the initial main motivation of this diploma thesis. We also give an estimate of the maximum splitting of the hyperfine structure of the exploited vibrational levels. As an outlook, we explain how our model can be improved and what improvements have already been made. In the Appendix we also illustrate the hyperfine splitting of the other adiabatic potentials that were not discussed in detail in Chapter 4.

The diploma thesis is structured as follows. In the second Chapter, we provide a background that is needed to understand the main ideas of this diploma thesis. These are general theoretical concepts like the Born-Oppenheimer approximation or details about spin-orbit interaction and hyperfine interactions. In Chapter 3, we present our approximations and show calculation details, for example the basis sets employed as well as where and how we implement the hyperfine interactions. The results are illustrated and discussed in Chapter 4. Chapter 5 covers the outlook. It points out how to improve the calculations. The Appendix summarizes our results of the hyperfine structure of potentials that are not discussed in the precedent chapters.

2 Theory

This Chapter gives an overview of the basic concepts that are important in the description of the structure of diatomic molecules. The Chapter begins with an introduction into the theory of angular momenta in quantum mechanics. This subject is explained in more detail in standard textbooks on quantum mechanics like Ref. [75, 76, 77] in books specialized on angular momenta in quantum mechanics like Ref. [78] and in books specialized on molecular spectroscopy like Ref. [79]. The second section presents characteristics of the cesium atom, such as the spin-orbit splitting and the hyperfine structure of the atomic states that are of interest for the diploma thesis. This is followed by a description of diatomic molecules in the third section. It includes the Born-Oppenheimer approximation as well as methods and principles of the treatment of the electronic and the nuclear motion. The fourth section describes Hund's coupling cases and extensions to the usual coupling cases that include the nuclear spin. Finally, in section five and six, a presentation of the spin-orbit interaction and the hyperfine interaction is given.

2.1 Angular Momenta in Quantum Mechanics

2.1.1 Orbital Angular Momentum

In classical mechanics angular momenta \vec{l} are defined by the cross product:

$$\vec{l} = \vec{r}' \times \vec{p}', \quad (2.1)$$

with \vec{r}' the position of the particle and \vec{p}' its momentum. By canonical quantization of the classical angular momentum, we obtain the quantum mechanical angular momentum operator \vec{l} :

$$\vec{l} = \vec{r}' \times \vec{p}' \longrightarrow \hbar \vec{l} = \vec{r} \times \vec{p} = -i\hbar \vec{r} \times \vec{\nabla} \quad (2.2)$$

\vec{r} and \vec{p} stand for the quantum mechanical operators of the position of a particle and its momentum respectively. i is the imaginary quantity, \hbar is Planck's constant divided by 2π , it has the value $\hbar = h/2\pi = 1.0545714810^{-34}$ Js and $\vec{\nabla}$ is defined in real space as the vector $\vec{\nabla} = \vec{e}_x \partial_x + \vec{e}_y \partial_y + \vec{e}_z \partial_z$. \vec{e}_x, \vec{e}_y and \vec{e}_z are an ortho-normal basis of real space. One can show that the components of \vec{l} , \hat{l}_x , \hat{l}_y and \hat{l}_z obey the commutation relation:

$$[\hat{l}_i, \hat{l}_k] = i\hbar \sum_{l=1}^3 \epsilon_{jkl} \hat{l}_l. \quad (2.3)$$

Thus, the values of two \hat{l}_i cannot be determined simultaneously. However, every component of \vec{l} commutes with the square of \vec{l} defined as

$$\vec{l}^2 = \hat{l}_x^2 + \hat{l}_y^2 + \hat{l}_z^2 \quad (2.4)$$

and

$$[\vec{l}^2, \hat{l}_k] = 0. \quad (2.5)$$

One of the components of \vec{l} , usually one chooses \hat{l}_z , and the operator \vec{l}^2 form a set of commuting operators. Hence, an eigenvector of one of the operators is also an eigenvector of the other and the eigenvalues of an eigenvector can be determined simultaneously. In spherical coordinates, $x = r \sin\theta \cos\phi$, $y = r \sin\theta \sin\phi$ and $z = r \sin\theta$, one can write \hat{l}_z and \vec{l}^2 as

$$\hat{l}_z = -i \frac{\partial}{\partial \theta} \quad (2.6)$$

and

$$\vec{l}^2 = - \left\{ \frac{1}{\sin\theta} \frac{\partial}{\partial \theta} \left(\sin\theta \frac{\partial}{\partial \theta} \right) + \frac{1}{\sin^2\theta} \frac{\partial^2}{\partial \phi^2} \right\}. \quad (2.7)$$

Solving the differential equations $\hat{l}_z \Phi_m(\phi) = \hbar m \Phi_m(\phi)$ and $\vec{l}^2 \Theta_{lm}(\theta) = \hbar^2 l(l+1) \Theta_{lm}(\theta)$, the well known spherical harmonics $Y_{lm}(\theta, \phi) = \Phi_m(\phi) \Theta_{lm}(\theta)$ are yielded as eigenvectors common to both operators. $\Theta_{lm}(\theta)$ are the associated Legendre polynomials and $\Phi_m(\phi)$ are functions proportional to $e^{im\phi}$. The possible values for the eigenvalues l and m are

$$l = 0, 1, 2, \dots \quad (2.8)$$

and

$$m = -l, -(l-1), \dots, l-1, l, \text{ for } l \text{ fixed.} \quad (2.9)$$

Figure 2.1 illustrates the eigenvalues of an angular momentum with quantum number $l = 3$ and $|\vec{l}| = \hbar\sqrt{3 \times 4} = \hbar\sqrt{20}$.

2.1.2 General Form of Angular Momenta

Additional to the orbital angular momentum, particles also have an *intrinsic* angular momentum \vec{s} . \vec{s} is called *spin*. It is not connected to the motion in real space and therefore cannot be described by the formalism given above. However, the components of \vec{s} obey the same commutation relations as the orbital angular momenta. Consequently, one uses these commutation relations to generally define angular momentum operators. The operators of any set of three Hermitian operators, \hat{J}_1 , \hat{J}_2 and \hat{J}_3 are called angular momentum operators if they follow the commutation relation:

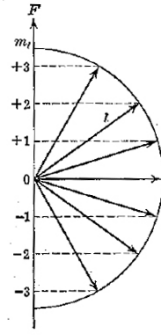


Figure 2.1: **Illustration of the eigenvalues of the angular momentum operators l and m for $l=3$.** The picture is adapted from Ref. [80]

$$\left[\hat{J}_i, \hat{J}_k \right] = i\hbar \sum_{l=1}^3 \epsilon_{jkl} \hat{J}_l. \quad (2.10)$$

The set \hat{J}_1 , \hat{J}_2 and \hat{J}_3 describes the components of the angular momentum vector \vec{J} . The square of \vec{J} is defined as

$$\vec{J}^2 = \hat{J}_1^2 + \hat{J}_2^2 + \hat{J}_3^2. \quad (2.11)$$

The ladder operators defined as

$$\hat{J}_{\pm} = \hat{J}_1 \pm i\hat{J}_2 \quad (2.12)$$

are also useful. An important property of the above definitions is

$$\left[\vec{J}^2, \hat{J}_k \right] = 0. \quad (2.13)$$

This means that \vec{J}^2 and one of the above defined angular momenta, for example \hat{J}_3 , share a set of common eigenvector $|jm\rangle$ s:

$$\vec{J}^2 |jm\rangle = \hbar^2 j(j+1) |jm\rangle \quad (2.14)$$

$$\hat{J}_3 |jm\rangle = \hbar m |jm\rangle, \quad (2.15)$$

with $j = 0, \frac{1}{2}, 1, \frac{3}{2}, 2, \frac{5}{2}, \dots \geq 0$ and $-j \leq m \leq +j$. Orbital angular momenta can only take on integer values, but the spin can take on integer and half-integer values.

2.1.3 Coupling of Angular Momenta

When dealing with more than two particles, one can define a total angular momentum by forming the sum of the single angular momenta. Such an addition of angular momenta is also called *coupling of angular momenta*. When two particles interact, it frequently occurs that the individual angular momenta are not constants of the motion, but the

total angular momentum commutes with the Hamiltonian of the system. It is then convenient to sum up the individual angular momenta in order to obtain the total angular momentum that can be worked with. The coupling of angular momenta is the issue of this subsection.

If two sets of angular momenta $\{\hat{J}_1^{(1)}, \hat{J}_2^{(1)}, \hat{J}_3^{(1)}\}$ and $\{\hat{J}_1^{(2)}, \hat{J}_2^{(2)}, \hat{J}_3^{(2)}\}$ are given by the two angular momentum vectors $\vec{J}^{(1)}$ and $\vec{J}^{(2)}$, every set has eigenvectors and eigenvalues:

$$\left(\vec{J}^{(1)}\right)^2 |j_1 m_1\rangle = \hbar^2 j_1(j_1 + 1) |j_1 m_1\rangle, \quad (2.16)$$

$$\hat{J}_3^{(1)} |j_1 m_1\rangle = \hbar m_1 |j_1 m_1\rangle \quad (2.17)$$

and

$$\left(\vec{J}^{(2)}\right)^2 |j_2 m_2\rangle = \hbar^2 j_2(j_2 + 1) |j_2 m_2\rangle, \quad (2.18)$$

$$\hat{J}_3^{(2)} |j_2 m_2\rangle = \hbar m_2 |j_2 m_2\rangle, \quad (2.19)$$

which form the Hilbert-spaces $\mathcal{H}_1(j_1) = \{|j_1 m_1\rangle\}_{m_1=-j_1\dots+j_1}$ and $\mathcal{H}_2(j_2) = \{|j_2 m_2\rangle\}_{m_2=-j_2\dots+j_2}$ for a fixed j_1 and j_2 .

As the operators act on distinct spaces, they commute:

$$\left[\hat{J}_k^{(1)}, \hat{J}_l^{(2)}\right] = 0. \quad (2.20)$$

The two sets share same eigenvectors that are defined by:

$$\left(\vec{J}^{(\nu)}\right)^2 |j_1 m_1 j_2 m_2\rangle = \hbar^2 j_\nu(j_\nu + 1) |j_1 m_1 j_2 m_2\rangle \quad (2.21)$$

and

$$\hat{J}_3^{(\nu)} |j_1 m_1 j_2 m_2\rangle = \hbar m_\nu |j_1 m_1 j_2 m_2\rangle \quad (2.22)$$

for $\nu = 1, 2$.

The eigenvectors span the Hilbert space $\mathcal{H}(j_1, j_2) = \mathcal{H}_1(j_1) \otimes \mathcal{H}_2(j_2) = \{|j_1 m_1 j_2 m_2\rangle\}_{m_1, m_2}$ for $m_1 = -j_1\dots + j_1$ and $m_2 = -j_2\dots + j_2$.

We can use the two sets to form a *coupled* angular momentum \vec{J} that is obtained by the addition of the two angular momenta $\vec{J} = \vec{J}^{(1)} + \vec{J}^{(2)}$. This coupling scheme is illustrated in figure 2.2

The components of the coupled operator

$$\hat{J}_k = \hat{J}_k^{(1)} + \hat{J}_k^{(2)}, \quad (2.23)$$

form a set of three operators $\{\hat{J}_1, \hat{J}_2, \hat{J}_3\}$ that obey the relations:

$$\left[\vec{J}^2, \hat{J}_k\right] = 0 \quad (2.24)$$

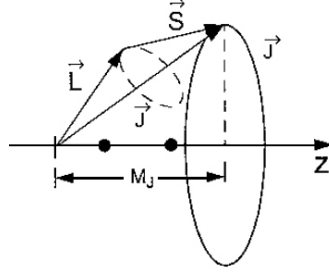


Figure 2.2: **Addition of two angular momenta** $\vec{j}^{(1)} = \vec{L}$ and $\vec{j}^{(2)} = \vec{S}$. The two coupled angular momenta form the resultant \vec{J} . \vec{J} is an angular momentum as well. The figure is taken from Ref. [81]

and

$$\left[\left(\vec{J}_k^{(\nu)} \right)^2, \hat{J}_k \right] = 0, (\nu = 1, 2). \quad (2.25)$$

Thus, $\left\{ \left(\vec{J}^{(1)} \right)^2, \left(\vec{J}^{(2)} \right)^2, \vec{J}^2, \hat{J}_3 \right\}$ form a set of commuting operators, which obey the equations:

$$\vec{J}^2 |(j_1, j_2)JM\rangle = \hbar^2 J(J+1) |(j_1, j_2)JM\rangle, \quad (2.26)$$

$$\hat{J}_3 |(j_1, j_2)JM\rangle = \hbar M |(j_1, j_2)JM\rangle \quad (2.27)$$

and

$$\left(\vec{J}^{(\nu)} \right)^2 |(j_1, j_2)JM\rangle = \hbar^2 j_\nu(j_\nu + 1) |(j_1, j_2)JM\rangle \quad (2.28)$$

for $\nu = 1, 2$. $J \geq 0$ and can take on the values $J = 0, \frac{1}{2}, 1, \frac{3}{2}, 2, \frac{5}{2}, \dots$ and $M = -J, \dots, +J$ for a given value of J . Moreover, further analysis shows that, for a given set of (j_1, j_2) , J can only take on the values:

$$J = |j_1 - j_2|, |j_1 - j_2| + 1, \dots, j_1 + j_2. \quad (2.29)$$

The braces in the notation $|(j_1, j_2)JM\rangle$ indicate that j_1 is coupled to j_2 in order to form J . Changing this order adds a phase $|(j_1, j_2)JM\rangle = (-1)^{j_1+j_2-J} |(j_2, j_1)JM\rangle$. The two sets of eigenvectors $|j_1 m_1 j_2 m_2\rangle$ and $|(j_1, j_2)JM\rangle$ form the basis of $\mathcal{H}(j_1, j_2)$. The transformation between these two bases is given by the formula:

$$|(j_1, j_2)JM\rangle = \sum_{m_1=-j_1}^{+j_1} \sum_{m_2=-j_2}^{+j_2} |j_1 m_1 j_2 m_2\rangle \langle j_1 m_1, j_2 m_2 | (j_1, j_2)JM\rangle \quad (2.30)$$

and the inversion

$$|j_1 m_1 j_2 m_2\rangle = \sum_{J=|j_1-j_2|}^{j_1+j_2} \sum_{M=-J}^{+J} |(j_1, j_2) JM\rangle \langle (j_1, j_2) JM | j_1 m_1 j_2 m_2\rangle. \quad (2.31)$$

The coefficients $\langle j_1 m_1 j_2 m_2 | (j_1, j_2) JM \rangle$ are called Clebsch-Gordan coefficients.

The Wigner 3j-symbols

There exists another quantity that is used instead of the Clebsch-Gordan coefficients to describe the coupling of angular momenta. It is called *Wigner 3j-symbol* and is defined by the formula:

$$\begin{pmatrix} j_1 & j_2 & J \\ m_1 & m_2 & -M \end{pmatrix} = (-1)^{j_1-j_2+M} \hat{J} \langle j_1 m_1 j_2 m_2 | (j_1, j_2) JM \rangle, \quad (2.32)$$

where $\hat{J} = \sqrt{2J+1}$. The Wigner 3j-symbols are used frequently because they have more symmetry relations than the Clebsch-Gordan coefficients.

Re-coupling of three angular momenta

Let us consider the case when the total angular momentum \vec{J} is formed by the sum of three angular momentum vectors, $\vec{J} = \vec{J}^{(1)} + \vec{J}^{(2)} + \vec{J}^{(3)}$. The components of \vec{J} , $\hat{J}_k = \hat{J}_k^{(1)} + \hat{J}_k^{(2)} + \hat{J}_k^{(3)}$ are angular momentum operators again. However, the state of the system cannot be unambiguously determined by just a given set (j_1, j_2, j_3, J, M) . It is also important to define in which way the three angular momenta are coupled. For example, two schemes would be: (I) one first adds $\hat{J}_k^{(2)}$ to $\hat{J}_k^{(1)}$ to give $\hat{J}_k^{(12)}$ and then forms the sum $\hat{J}_k^{(12)} + \hat{J}_k^{(3)}$ to form J_k ; or (II) add $\hat{J}_k^{(1)}$ to the sum of $\hat{J}_k^{(23)} = \hat{J}_k^{(2)} + \hat{J}_k^{(3)}$ and then form $J_k = \hat{J}_k^{(1)} + \hat{J}_k^{(23)}$. In scheme (I) (respectively (II)) $\hat{J}_k^{(12)}$ (respectively $\hat{J}_k^{(23)}$) has a definite value.

We get two bases of the Hilbert space $\mathcal{H}(j_1, j_2, j_3) = \mathcal{H}(j_1) \otimes \mathcal{H}(j_2) \otimes \mathcal{H}(j_3)$ due to the two different coupling schemes:

$$|((j_1, j_2) j_{12}, j_3) JM\rangle \quad (2.33)$$

for the case (I) and

$$|(j_1, (j_2, j_3) j_{23}) JM\rangle \quad (2.34)$$

for the case (II). Again, there exists a transformation between the two bases defined above:

$$|((j_1, j_2) j_{12}, j_3) JM\rangle = \sum_{j_{12}} \langle (j_1, (j_2 j_3) j_{23}) JM | ((j_1 j_2) j_{12}, j_3) JM \rangle \times |(j_1, (j_2 j_3) j_{23}) JM\rangle. \quad (2.35)$$

Such a transformation can be found by first de-coupling a basis vector and then re-coupling it in the desired manner. For example, a state $|((j_1, j_2)j_{12}, j_3)JM\rangle$ obtained by applying scheme (I) can be de-coupled into:

$$\begin{aligned} |((j_1, j_2)j_{12}, j_3)JM\rangle &= \sum_{m_{12}, m_3} |j_{12}m_{12}, j_3m_3\rangle \langle j_{12}m_{12}, j_3m_3 | ((j_1, j_2)j_{12}, j_3)JM\rangle \\ &= \sum_{m_{12}, m_3} \left(\sum_{m_1, m_2} |j_1m_1, j_2m_2\rangle \langle j_1m_1, j_2m_2, j_3m_3 | (j_1, j_2)j_{12}m_{12}\rangle \right) \\ &\quad |j_3m_3\rangle \langle j_{12}m_{12}, j_3m_3 | ((j_1, j_2)j_{12}, j_3)JM\rangle \end{aligned} \quad (2.36)$$

If we re-couple $|j_1m_1, j_2m_2, j_3m_3\rangle$ by using coupling scheme (II), we get a relation between (I) and (II). By using the orthogonality relations of the Clebsch-Gordan coefficients we obtain

$$\begin{aligned} |((j_1, j_2)j_{12}, j_3)JM\rangle &= \sum_{\substack{j_{23}, m_1, m_2, \\ m_3, m_{12}, m_{23}}} \langle (j_{12}, j_3)JM | j_{12}m_{12}j_3m_3\rangle \langle (j_1, j_2)j_{12}m_{12} | j_1m_1, j_2m_2\rangle \\ &\quad \langle j_2m_2j_3m_3 | (j_2, j_3)j_{23}\rangle \langle j_1m_1j_{23}m_{23} | (j_1, j_{23})JM\rangle \\ &\quad | (j_1, (j_2j_3)j_{23})JM\rangle. \end{aligned} \quad (2.37)$$

Thus, the transformation coefficient $\langle (j_1, (j_2j_3)j_{23})JM | ((j_1j_2)j_{12}, j_3)JM\rangle$ is given by

$$\begin{aligned} \langle (j_1, (j_2j_3)j_{23})JM | ((j_1j_2)j_{12}, j_3)JM\rangle &= \\ &\sum_{\substack{m_1, m_2, m_3, \\ m_{12}, m_{23}}} \langle (j_{12}, j_3)JM | j_{12}m_{12}, j_3m_3\rangle \langle (j_1, j_2)j_{12}m_{12} | j_1m_1, j_2m_2\rangle \\ &\quad \langle j_2m_2j_3m_3 | (j_2, j_3)j_{23}\rangle \langle j_1m_1, j_{23}m_{23} | (j_1, j_{23})JM\rangle \end{aligned} \quad (2.38)$$

From this transformation coefficient, one defines the $6j$ -symbols by the formula:

$$\left\{ \begin{array}{ccc} j_1 & j_2 & j_{13} \\ j_3 & J & j_{23} \end{array} \right\} = \frac{(-1)^{j_1+j_2+j_3+J}}{\sqrt{(2j_{12}+1)(2j_{23}+1)}} \langle (j_1, (j_2j_3)j_{23})JM | ((j_1j_2)j_{12}, j_3)JM\rangle. \quad (2.39)$$

They are defined in such a way so as to give the $6j$ -symbols the maximum number of symmetry relations.

Re-coupling of four angular momenta

In the case of four different sets of angular momenta $\{\vec{j}^{(1)}, \vec{j}^{(2)}, \vec{j}^{(3)}, \vec{j}^{(4)}\}$, there are even more coupling possibilities than in the case of the coupling of three angular momenta.

Again we find transformation relations by de- and re-coupling of angular momenta. To demonstrate this, we give an example for the transformation between two coupling schemes. The first one (I) leads to a basis set $|((j_1, j_2)j_{12}, (j_3, j_4)j_{34})JM\rangle$ and the second one (II) leads to the basis set $|((j_1, j_3)j_{13}, (j_2, j_4)j_{24})JM\rangle$. Both coupling schemes are illustrated in figure 2.3. Later we will need the transformation between these two sets in our calculations. One calculates transformations of the form:

$$|((j_1, j_2)j_{12}, (j_3, j_4)j_{34})JM\rangle = \sum_{j_{13}, j_{24}} \langle(j_{13}, j_{24})JM|(j_{12}, j_{34})JM\rangle |((j_1, j_3)j_{13}, (j_2, j_4)j_{24})JM\rangle.$$

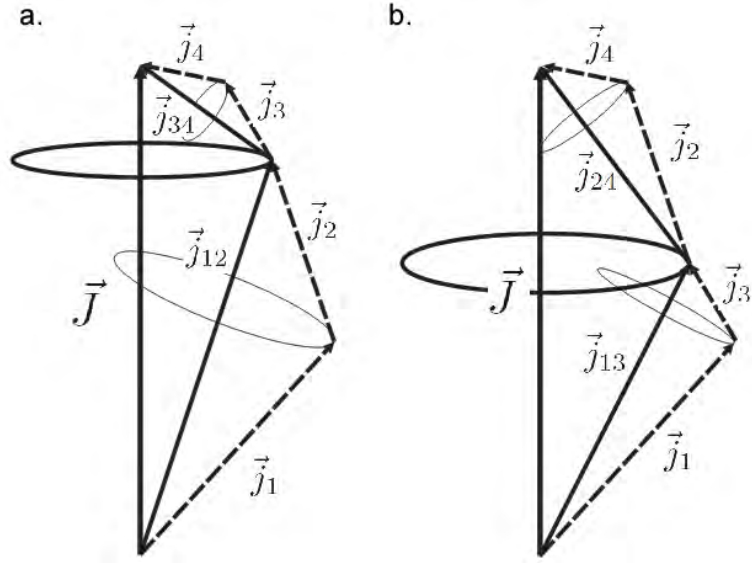


Figure 2.3: **Illustration of the coupling of four angular momenta $\vec{j}_1, \vec{j}_2, \vec{j}_3$ and \vec{j}_4 .** Panel **a** shows coupling scheme (I) and panel **b** shows coupling scheme (II).

By using the $9j$ -symbol,

$$\left\{ \begin{array}{ccc} j_1 & j_2 & j_{12} \\ j_3 & j_4 & j_{34} \\ j_{13} & j_{24} & J \end{array} \right\} = \sum_m (-1)^{2m} (2m+1) \left\{ \begin{array}{ccc} j_1 & j_3 & j_{13} \\ j_{24} & J & m \end{array} \right\} \left\{ \begin{array}{ccc} j_2 & j_4 & j_{24} \\ j_3 & m & j_{34} \end{array} \right\} \left\{ \begin{array}{ccc} j_{12} & j_{34} & J \\ m & j_1 & j_2 \end{array} \right\} \quad (2.40)$$

where m takes on all (integer or half integer) values that are allowed by the internal rules of the $6j$ symbols, one can denote the transformation coefficient as

$$\langle(j_{13}, j_{24})JM|(j_{12}, j_{34})JM\rangle = \sqrt{(2j_{12}+1)(2j_{34}+1)(2j_{13}+1)(2j_{24}+1)} \left\{ \begin{array}{ccc} j_1 & j_2 & j_{12} \\ j_3 & j_4 & j_{34} \\ j_{13} & j_{24} & J \end{array} \right\}.$$

2.2 The Cesium Atom

Like all alkali-metals, cesium has only one valence electron in the ground state. The electron configuration of the closed shell electrons is given by the same electron con-

figuration as for Xenon. The state of the valence electron is $6s$, where 6 is the value of the principal quantum number n and s denotes the eigenvalue of the square of the electrons orbital angular momentum \vec{l} . s means $l = 0$. This also determines the net-electron spin \vec{S} of cesium in its ground state, $S = 1/2$. It is made up by the spin \vec{s} of the valence electron only. All others add up to zero. Hence, the value of the total electronic angular momentum J , where \vec{J} is defined as $\vec{J} = \vec{l} + \vec{s}$, is $J = 1/2$. The state of the valence electron in the ground state is denoted in spectroscopic notation as $6s^2S_{1/2}$ and we refer to it by Cs($6s$) or equally Cs($6s^2S_{1/2}$). The eigenvalue I of the nuclear spin \vec{I} is $I = 7/2$. Due to hyperfine interactions, the ground state splits up into two hyperfine levels with $F = 3$ and $F = 4$, where F is the quantum number of the total angular momentum $\vec{F} = \vec{J} + \vec{I}$. The splitting between the $F = 3$ and $F = 4$ level is 9.192631770 GHz. The radiation corresponding to the transition between these two hyperfine levels is used to define the time unit *second*. One second is defined as the duration of 9192631770 periods of the radiation.

Important for this diploma thesis is the first excited state of the valence electron, $6p$, referred to as Cs($6p$). Since for Cs($6p$) $l = 1$, J can take on the values $1/2$ and $3/2$. By spin-orbit interaction, Cs($6p$) splits up into the two levels $6p^2P_{1/2}$ and $6p^2P_{3/2}$, which are separated by $\Delta = 554.039 \text{ cm}^{-1}$. We refer to these two states as Cs($6p^2P_{1/2}$) and Cs($6p^2P_{3/2}$). Due to hyperfine interactions Cs($6p^2P_{1/2}$) and Cs($6p^2P_{3/2}$) split up according to the possible values of F . The state Cs($6p^2P_{1/2}$) splits into two levels with $F = 3$ and $F = 4$. The splitting between these two levels is 1.167688 GHz. The state Cs($6p^2P_{3/2}$) splits up by hyperfine interactions into four levels with $F = 2, 3, 4, 5$. The splitting between $F = 2$ and $F = 3$ is 0.1512247 GHz, between $F = 3$ and $F = 4$ it is 0.2012871 GHz and between $F = 4$ and $F = 5$ it is 0.2510916 GHz.

The hyperfine structure of the Cs($6^2S_{1/2}$) state is illustrated in figure 2.4. The spin-orbit splitting of the Cs($6p$) state and the hyperfine structure of the Cs($6^2P_{1/2}$) state and Cs($6^2P_{3/2}$) state are illustrated in figure 2.5

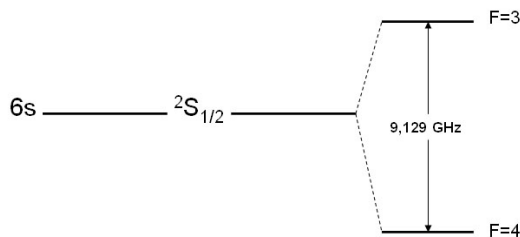


Figure 2.4: **Hyperfine structure of the state Cs($6^2S_{1/2}$)**. Spin-orbit interaction has no effect on the $6s$ state, however, hyperfine interactions split the $6s$ level into two levels with $F = 3$ and $F = 4$, which are separated by 9.192631770 GHz.

2.3 Description of Diatomic Molecules

In the book *Rotational Spectroscopy of Diatomic Molecules* ([79]) John Brown and Alan Carrington describe a molecule in the following way: A molecule is an assembly of positively charged nuclei and negatively charged electrons that form a stable entity through the electrostatic forces, which hold it all together. The aim of this section is to describe how to obtain an approximate, quantum mechanical description of such an entity. Firstly, we determine the problem by setting up the Schrödinger equation. Then,

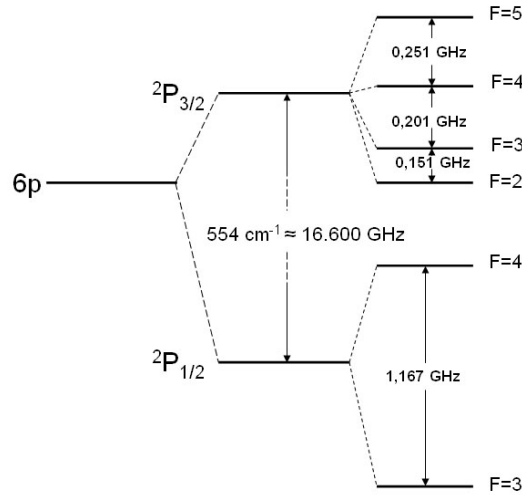


Figure 2.5: **Spin-orbit splitting of the $6p$ state of atomic cesium and hyperfine structure of the $\text{Cs}(6p^2P_{1/2})$ state and $\text{Cs}(6p^2P_{3/2})$ state.** Spin-orbit interaction splits the energy level of the $6p$ state into the energy levels of the $6p^2P_{1/2}$ state and the $6p^2P_{3/2}$ state. The splitting between the two states is quite large with $\Delta = 554.039 \text{ cm}^{-1}$. The hyperfine splitting of the $6p^2P_{1/2}$ and the $6p^2P_{3/2}$ state is also shown. The $6p^2P_{1/2}$ splits up into two levels with $F = 3$ and $F = 4$ and the $6p^2P_{3/2}$ splits up into 4 levels with $F = 2, 3, 4, 5$.

we explain the Born-Oppenheimer approximation, which enables us to separate the motion of the electrons from the motion of the nuclei, which is classified into vibration and rotation. This is followed by a description of the calculation of the electrons wave function and energy potential curves as well as an explanation of the symmetries and the state labeling. Lastly, we briefly introduce possible techniques to determine the wave function of the nuclei within the Born-Oppenheimer approximation.

2.3.1 The Diatomic Molecule

A diatomic molecule consists of two heavy nuclei and N much lighter electrons, which interact by electric forces. The nuclei carry the charge $+Z_\alpha e$ where Z_α is the number of protons in the nucleus $\alpha = A, B$ and $e = 1.60217646 \cdot 10^{-19} \text{ C}$ the elementary charge. The electrons are charged by $-e$. Figure 2.6 schematically displays the situation.

The Schrödinger equation reads as

$$\hat{H}\Psi = E\Psi, \quad (2.41)$$

where \hat{H} is the Hamiltonian of the system. It can be written as

$$\hat{H} = \hat{T}_e + \hat{T}_N + \hat{V}. \quad (2.42)$$

\hat{H} is a sum of the kinetic energy of the electrons \hat{T}_e , the kinetic energy \hat{T}_N of the two nuclei and the potential energy \hat{V} . In a more explicit way, we can write the Hamiltonian as

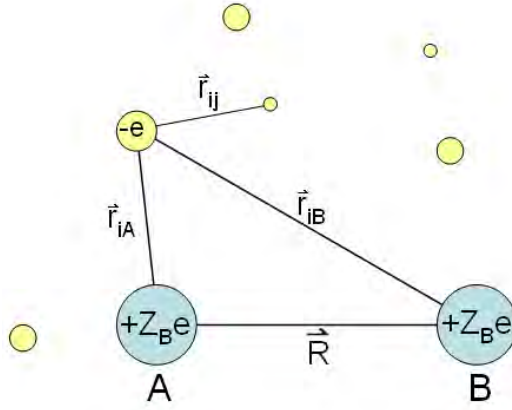


Figure 2.6: **Schematic sketch of a diatomic molecule.** The two nuclei A and B are separated by a vector \vec{R} and carry the charge $+Z_A e$ and $+Z_B e$. The electrons are charged with $-e$. The distance between the i^{th} electron and the nucleus α is given by the vector $\vec{r}_{i\alpha}$. The vector between the i^{th} and the j^{th} electrons is denoted by \vec{r}_{ij} .

$$\hat{H} = \underbrace{-\frac{\hbar^2}{2m} \sum_{i=1}^N \nabla_i^2}_{=T_e} - \underbrace{\frac{\hbar^2}{2} \sum_{\alpha=1}^2 \frac{1}{M_\alpha} \nabla_\alpha^2}_{=T_N} + \underbrace{V(\vec{r}, \vec{R}_A, \vec{R}_B)}_{=V}. \quad (2.43)$$

Here, m is the mass of an electron and M_α the mass of the α^{th} nuclei. The spatial vector \vec{r} stands symbolically for the positions of the electrons and the vectors \vec{R}_A and \vec{R}_B mean the position of the two nuclei. $V(\vec{r}, \vec{R}_A, \vec{R}_B)$ itself can again be separated into three parts:

$$V(\vec{r}, \vec{R}) = V_{\text{nucl,nucl}}(\vec{R}_A, \vec{R}_B) + V_{\text{nucl,el}}(\vec{r}, \vec{R}_A, \vec{R}_B) + V_{\text{el,el}}(\vec{r}). \quad (2.44)$$

$V_{\text{nucl,nucl}}(\vec{R}_A, \vec{R}_B)$ describes the interaction between the nuclei. $V_{\text{nucl,el}}(\vec{r}, \vec{R}_A, \vec{R}_B)$ is the potential energy for the interaction between the nuclei and the electrons and $V_{\text{el,el}}(\vec{r})$ is the interaction between all the electrons of the system.

The interactions considered here can be of various types. In general, the considered interactions depend on the desired level of accuracy. For example, one can consider Coulomb interactions only, with the nuclei treated as point-like particles. More realistic models include also relativistic effects or interactions between the molecular rotation and the orbital angular momentum of the electrons, etc. In this section we restrict ourselves to Coulomb interactions and include other interactions later by perturbation theory. The electrons and the nuclei are considered to be point-like particles. We do not include relativistic effects or coupling between any angular momenta. In this case the potential has the form:

$$V(\vec{r}, \vec{R}) = \frac{e^2}{4\pi\epsilon_0} \left(\frac{Z_A Z_B}{R} - \sum_{i=1}^N \frac{Z_A}{r_{Ai}} - \sum_{i=1}^N \frac{Z_B}{r_{Bi}} + \sum_{i>j} \sum_{j=1}^N \frac{1}{r_{i,j}} \right). \quad (2.45)$$

ϵ_0 is the vacuum permittivity, R is the separation between the nuclei, $r_{A,i}$ and $r_{B,i}$ are the distances between nucleus A or B and the i^{th} electron, and finally $r_{i,j}$ is the distance between the i^{th} and the j^{th} electron.

As this form of a $V(\vec{r}, \vec{R})$ already couples the motion of all particles, exact solutions for the Schrödinger equation 2.41 are impossible to obtain. Simplifications are needed in order to make statements about molecular states and energies.

In the following parts of this section we present the adiabatic or Born-Oppenheimer approximation. It provides us with an important concept in molecular physics and enables us to treat the motion of the nuclei separately from the motion the electrons.

2.3.2 The Adiabatic or Born-Oppenheimer Approximation

The adiabatic or Born-Oppenheimer approximation builds upon the fact that nuclei are much heavier than electrons. For example, in the case of the Hydrogen atom the ratio between the mass of the nucleus (a proton) m_p and the electron mass m_e is indeed $\frac{m_p}{m_e} \approx 1800$. For molecules, this number is much larger. As the Coulomb interaction acts with similar strength on all the particles, the electrons are accelerated faster than the nuclei by the electric forces. Therefore, the electron cloud adjusts more or less *instantaneously* to a change of the position of the nuclei [81]. One can assume that for every separation \vec{R} of the nuclei, there exists a well-defined electron distribution specified by the wave function $\Phi_n^{el}(\vec{r}, \vec{R})$ for the electronic state $|n\rangle$. (The characterization of such a state by its quantum numbers is explained later.) Once the electrons are in an electronic state $|n\rangle$, they adapt their wave function adiabatically to the slowly changing configuration of the nuclei. \vec{R} can be regarded as a parameter and one solves the electronic Schrödinger equation for different values of this parameter. One first solves the Schrödinger equation 2.41 for the electronic degrees of freedom, with the nuclei fixed at a separation \vec{R} , and afterward the motion of the nuclei is included as a perturbation.

The Schrödinger equation can be rewritten as

$$(\hat{H}_0 + \hat{H}_1)\Psi^{\text{tot}} = E\Psi^{\text{tot}}. \quad (2.46)$$

$\hat{H}_0 = \hat{T}_e + V$ is the unperturbed Hamiltonian and $\hat{H}_1 = \hat{T}_N$ the perturbative term. First one solves the unperturbed Schrödinger equation. As the vector \vec{R} is considered to be fixed, the eigenvalues $U_n(\vec{R})$ of the state $|n\rangle$ only depend parametrically on the internuclear distance R :

$$\hat{H}_0|n\rangle = U_n(R)|n\rangle. \quad (2.47)$$

The state $|n\rangle$ can be used to express the solution of the Hamiltonian 2.43 in the form:

$$\Psi^{\text{tot}}(\vec{r}, \vec{R}) = \sum_n \Psi_n(\vec{R}) |n\rangle. \quad (2.48)$$

$\Psi_n(\vec{R})$ is the wave function of the nuclei, when the electrons are in the state $|n\rangle$. Now one substitutes Ψ^{tot} in the Schrödinger equation 2.46 and one obtains

$$(\hat{H}_0 + \hat{H}_1 - E) \sum_n |n\rangle \Psi_n(\vec{R}) = 0. \quad (2.49)$$

Multiplication from the left by an arbitrary state $\langle m|$ and integration over the electronic coordinates yields

$$(U_m(R) - E) \Psi_m(\vec{R}) + \sum_n \langle m| H_1 |n\rangle \Psi_n(\vec{R}) = 0. \quad (2.50)$$

We use the definition of $\hat{H}_1 = T_N = -\frac{\hbar^2}{2} \sum_{k=1}^2 \frac{1}{M_k} \vec{\nabla}_k^2$ and obtain after some calculations:

$$\left[-\frac{\hbar^2}{2} \sum_{k=1}^2 \frac{1}{M_k} \vec{\nabla}_k^2 + U_m(R) - E \right] \Psi_m(\vec{R}) = \sum_n \Lambda_{mn} \Psi_n(\vec{R}), \quad (2.51)$$

with the non-adiabatic coupling matrix-elements Λ_{mn} , which are defined as

$$\Lambda_{mn} = \sum_k \frac{\hbar^2}{M_k} \langle m| \frac{\partial}{\partial R_k} |n\rangle \frac{\partial}{\partial R_k} + \langle m| \frac{\hbar^2}{2} \sum_{k=1}^2 \frac{1}{M_k} \vec{\nabla}_k^2 |n\rangle. \quad (2.52)$$

The Λ_{mn} describe how the electronic states $|n\rangle$ are coupled by the nuclear motion.

In the Born-Oppenheimer approximation we assume that the Λ_{mn} are negligibly small. Therefore, this approximation concerns the case where the electrons always stay in the same electronic state. In the Born-Oppenheimer approximation, the Schrödinger equation can be replaced by two equations. The first one is the Schrödinger equation for H_e and the second one is equation 2.51 with $\Lambda_{mn} = 0$:

$$\hat{H}_0 |m\rangle = U_m(R) |m\rangle \quad (2.53)$$

and

$$\left[-\frac{\hbar^2}{2} \sum_{k=1}^2 \frac{1}{M_k} \vec{\nabla}_k^2 + U_m(R) - E \right] \Psi_m(\vec{R}) = 0. \quad (2.54)$$

Equation 2.53 is providing us with the electronic states, whose energy eigenvalues as a function of R are called electronic potentials, Hund's case *a* potentials or diabatic potentials. The electronic potentials are used in equation 2.54 as a potential for the Schrödinger equation of the nuclei. The overall molecular state is a product of the considered electronic state and the eigenfunctions obtained by solving equation 2.54.

The use of the term *diabatic* is somewhat confusing. As a result of the adiabatic approximation we obtain diabatic potentials. This denomination comes from calculations in which the spin-orbit interaction is also taken into account. Usually, spin-orbit interaction leads only to small shifts of the electronic potentials, but the state can be considered as unchanged. However, for internuclear separations where two electronic potentials come close to or even cross each other the spin-orbit interaction can couple

the states of the two electronic potentials. Due to the coupling, a crossing vanishes and the coupled potentials form avoided crossings. The avoided crossing is connecting two different electronic states. As a consequence of the avoided crossings, the electronic state changes *adiabatically* from one initial electronic state to another. For this reason, one is speaking of adiabatic potentials when the spin-orbit interaction is included. Potentials that take only Coulomb interactions into account are called diabatic potentials.

In the next subsection, we concentrate on some details of the electronic states and the electronic potentials, before continuing with a brief discussion of the motion of the nuclei.

2.3.3 Electronic States and Electronic Potentials

In the above subsection, we showed how it is possible, by applying the Born-Oppenheimer approximation, to treat the motion of the electrons separately from the motion of the nuclei. In this subsection, we look in a more detailed way on the electronic states and the electronic potentials.

The electrons are described by the equation 2.53, as presented in the above subsection. In general, the equation for the electronic states is not exactly solvable. Thus, further approximations are needed. An important technique in the approximation of electronic states and their potentials is the *variational method* (as described in Ref. [81]).

The variational method

An exact eigenfunction that solves the eigenvalue equation 2.53 for a fixed value of $R = R_0$ leads to exact electronic potentials. But what if we take a trial function $|\Phi\rangle$ that is different from the exact eigenfunction? Such a function yields the expectation value:

$$E_{\text{appeox}} = \frac{\langle \Phi | \hat{H}_0 | \Phi \rangle}{\langle \Phi | \Phi \rangle}. \quad (2.55)$$

Since it is an approximate function and not the exact solution, there is a difference between $U_m(R_0)$ and E_{appeox} . Now the difference of the exact and the approximate energy can be calculated. It is

$$E_{\text{appeox}} - U_m(R_0) = \frac{\langle \Phi | \hat{H}_0 | \Phi \rangle}{\langle \Phi | \Phi \rangle} - U_m(R_0) = \frac{\langle \Phi | (\hat{H}_0 - U_m(R_0)) | \Phi \rangle}{\langle \Phi | \Phi \rangle}. \quad (2.56)$$

If we assume that the wave function of our approximate state can be written as the sum of $\Phi = \Phi_m + \delta\Phi$, we can substitute it in equation 2.56

$$E_{\text{appeox}} - U_m(R_0) = \frac{\langle \delta\Phi | (\hat{H}_0 - U_m(R_0)) | \delta\Phi \rangle}{\langle \Phi | \Phi \rangle}. \quad (2.57)$$

Thus, the difference $E_{\text{appeox}} - U_m(R_0)$ depends quadratically on the difference $\delta\Phi$ and must assume a minimum for $\delta\Phi = 0$. We get

$$E_{\text{appeox}} - U_m(R_0) \geq 0 \implies E_{\text{appeox}} \geq U_m(R_0). \quad (2.58)$$

Hence, the energies calculated with approximate wave functions $\Phi = \Phi_m + \delta\Phi$ are always larger than the true energy $U_m(R_0)$. This gives a criterion for the quality of a chosen approximate wave function. We have to take the wave function that minimizes the energy expectation value.

Generally, our function Φ is expressed as a linear combination of test functions:

$$\Phi = \sum c_i \phi_i. \quad (2.59)$$

Exact solutions require an infinite number of test functions, thus one always truncates the set. Then, the goal is to choose the coefficients c_i in such a way that the wave function Φ minimizes the energy.

Test functions

Possible sets of test functions should either be easy to handle mathematically (all operations should converge fast, since the calculations are usually extensive) or motivated by physical reasons, or both. Test functions that include atomic orbitals are very commonly used, for example linear combination of atomic orbitals or linear combination of products of atomic orbitals. This is motivated by the fact that, when the internuclear distance is becoming infinite, the density distribution of the electrons inside a molecule has to comply with the density distribution of the electrons of two atoms. In addition, every set of functions has to fulfill certain symmetry properties. These properties are discussed later in section 2.3.4.

Electronic potentials at large internuclear distance: The multipole expansion

When the distance between the nuclei A and B is larger than the LeRoy-radius R_c , the electronic potentials can be described by electric multipole interactions between the atoms. The electronic state is given by the two-atom state. R_c is the distance at which the electron clouds start to overlap significantly as R is reduced (see figure 2.7). The region, $R > R_c$ is also called long-range region. One can calculate R_c with the formula [82]:

$$R_c = 2 \left(\sqrt{\langle n_A l_A | r_A^2 | n_A l_A \rangle} + \sqrt{\langle n_B l_B | r_B^2 | n_B l_B \rangle} \right). \quad (2.60)$$

r_i denotes the position of the outermost electron of atom A or B . $|n_i l_i\rangle$ stands for the state of the outermost electrons. n_i, l_i are the principal quantum number and the angular momentum. In the case of $\text{Cs}_2(6s + 6p)$ R_c takes on the value $R_c = 28.4a_0$.

M. Marinescu and A. Dalgarno present in Ref. [83] the perturbative approach for the calculations of the electronic potentials in the case of diatomic alkali molecules for $R > R_c$. In their treatment they explicitly take into account the contribution of the valence electrons only. The result is an expansion of the electronic potential of the form:

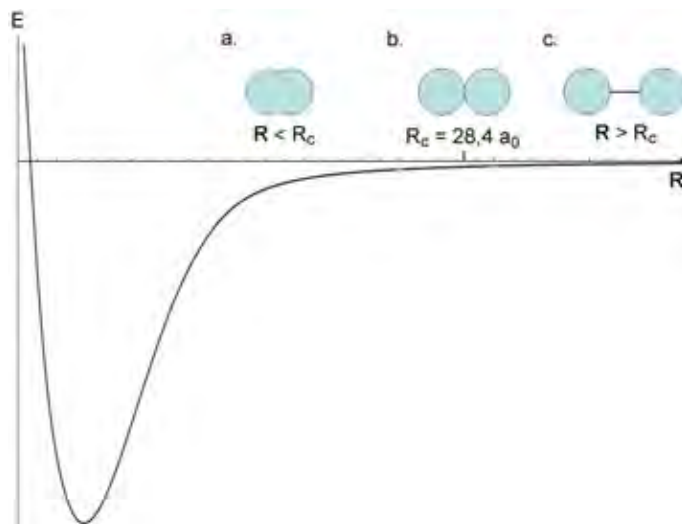


Figure 2.7: **Illustration of the overlap of the electronic wave functions of the atoms.**

In situation **a.** the distance between the nuclei is small ($R < R_c$). The atomic clouds overlap significantly and exchange interaction effects are very important. The electronic potentials can only be described accurately if one is using quantum chemistry calculations. **b.** shows the case of $R = R_c$, where the wave functions are not overlapping yet. For $R > R_c$ (see **c.**) the nuclei are separated far enough so that the molecular potential can be approximated by multipole interactions.

	C_3	C_6	C_8
$\beta = +1, m_l = 0 :$	20.95	$17.39 \cdot 10^3$	$5.040 \cdot 10^6$
$\beta = -1, m_l = 0 :$	-20.95	$17.39 \cdot 10^3$	$16.56 \cdot 10^6$
$\beta = +1, m_l = 1 :$	-10.47	$11.83 \cdot 10^3$	$2.256 \cdot 10^6$
$\beta = +1, m_l = 1 :$	10.47	$11.83 \cdot 10^3$	$9.131 \cdot 10^5$

Table 2.1: **Dispersion coefficients for $\text{Cs}_2(6s + 6p)$ states.**

$$U_m(R) = \sum_n \frac{C_n^m}{R^n} \quad \text{for } R > R_c. \quad (2.61)$$

The C_n^m are called dispersion coefficients. They depend on the dissociation limit of the molecule. For our present case, $\text{Cs}_2(6s + 6p)$, M. Marinescu and A. Dalgarno give state dependent values for the first three non-zero coefficients that are C_3 , C_6 and C_8 . The values of the dispersion coefficients for $\text{Cs}_2(6s + 6p)$ are given in table 2.1. Moreover, the four resulting potentials $U_m(R)$ are plotted in figure 4.1 of the Chapter *Results and Discussion*. The coefficients depend on the absolute value of the projection of the p -electrons orbital angular momentum on the z -axis $|m_l|$ and on the symmetry eigenvalue β given by the formula $\beta = (-1)^{p\sigma}$. $p = +1$ for g states and $p = -1$ for u states. $\sigma = +1$ for singlet states and $\sigma = -1$ for triplet states.

Asymptotic exchange interaction

In the region of the LeRoy-radius, the overlap between the two atomic charge distributions starts to increase exponentially. This leads to an increase of the exchange effects, which thus can be not neglected anymore. We include this effect by referring to an

article by M. Marinescu and A. Dalgarno again. In Ref. [84] they describe how one can derive an analytical expression of the exchange interaction for large atomic separations called *asymptotic* exchange interaction. The expression that they give is of the form:

$$V_{\text{exch}} = \sigma(a_1 R^{a_2} e^{-a_3 R} + \beta(b_1 R^{b_2} e^{-b_3 R})). \quad (2.62)$$

σ and β are defined in the same way as in the previous subsection on the multipole expansion. Like the C_n -coefficients of the multipole expansion, a_1 , a_2 , a_3 and b_1 , b_2 , b_3 are constants that depend on the dissociation limit of the molecule. Due to the asymptotic exchange interaction, the degeneracy of the potentials obtained from the multipole expansion is lifted resulting in eight distinct diabatic potentials. These potentials are plotted in figure 4.2 of the Chapter *Results and Discussion*

2.3.4 Labeling of Electronic States

We have seen before how one can calculate approximate wave functions and energies of electronic states. But even without such calculations we can make assumptions about the structure of possible solutions by considering the symmetry properties. In addition, we use these general physical restrictions as a criterion for the classification and the labeling of the states. In our labeling scheme we follow Ref. [81].

Symmetry of the electric field of the nuclei

First we want to look at the symmetry of the electric field created by the nuclei. Contrary to the case of atoms, it has not spherical symmetry, but a cylindrical symmetry. Therefore, the angular momentum \vec{l} of the electrons is not conserved. Moreover, the total angular momentum of all electrons $\vec{L} = \sum_{i=1}^N$ is also not conserved. \vec{L} precesses about the internuclear axis. Only the projection M_L of \vec{L} on the internuclear axis is conserved. It is also important to note that electronic states with the same absolute value of M_L denoted as $\Lambda = |M_L|$ are degenerated in energy. The quantum number Λ is often used to label molecular states. Following the labeling of atomic states, where states are labeled with lower case Roman letters s, p, d, f, g, \dots according to the value of the angular momentum quantum number $l = 0, 1, 2, 3, \dots$, electronic states of molecules are labeled with capital Greek letters. Thus, $\Lambda = 0, 1, 2, 3, \dots$ is labeled with $\Sigma, \Pi, \Delta, \Phi, \dots$

Symmetry operations

A symmetry operation \hat{S} is an operation that leaves the density distribution $|\Phi_m^{\text{el}}|^2$ of an electronic state Φ_m^{el} unchanged. Therefore, these operations can only add a phase $e^{i\theta}$ to the wave function:

$$\hat{S}|\Phi_m^{\text{el}}|^2 = |\Phi_m^{\text{el}}|^2 \quad \text{and} \quad \hat{S}\Phi_m^{\text{el}} = e^{i\theta}\Phi_m^{\text{el}}. \quad (2.63)$$

In the context of diatomic molecules, only symmetry operations occur that, if applied twice, do not have an effect on the wave function (like the exchange of two particles or a reflection on a plane). Therefore, the phase can only be ± 1 . We have

$$\hat{S}\Phi_m^{\text{el}} = \pm 1\Phi_m^{\text{el}} \quad \text{since} \quad \hat{S}^2\Phi_m^{\text{el}} = \Phi_m^{\text{el}}. \quad (2.64)$$

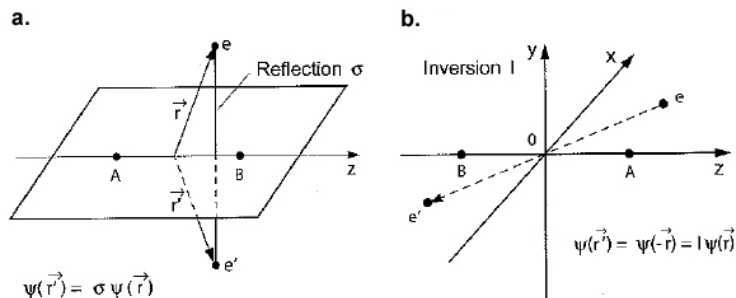


Figure 2.8: **Illustration of two symmetry operations.** (a) σ reflection on a plane containing the internuclear axis and (b) I inversion of the coordinates at the nuclear center of mass. The figure is adapted from Ref. [81].

It is said that a state is symmetric with respect to a symmetry operation \hat{S} if it has $+1$ as eigenvalue and anti-symmetric if the eigenvalue is -1 . For a diatomic molecule we have to look at the following symmetry operations:

1. **Exchange of two electrons** Electrons are fermions and their overall wave function changes its sign with respect to the exchange of two of them. First of all, this restricts the number of possible states, which is important when a wave function can be written as a product of a spin part and an orbital part. If one of the parts is symmetric (anti-symmetric) under exchange, the other one has to be anti-symmetric (symmetric). Second, the symmetry is also connected to different energies. Most diatomic molecules have a ground state that has an anti-symmetric spin-part.

2. **Exchange of the nuclei and g/u symmetry (I)** In the case of homonuclear molecules, the exchange of two nuclei is also a symmetry operation. If the nuclear spin has half-integer values or integer values, the nuclei are described as fermions or bosons, and the overall wave function has to be either symmetric or anti-symmetric with respect to the exchange of the nuclei. The indistinguishability of the nuclei also leads to a symmetry property of the electronic wave function. If we invert the coordinates of the electrons at the centre of mass of the nuclei, then the electronic wave function has to be symmetric or anti-symmetric under this operation. States with a symmetric electronic wave function are called *gerade* (g) and with an anti-symmetric wave function *ungerade* (u) (*gerade* is the German word for *even* and *ungerade* is the German word for *odd*). We denote the operator of this symmetry with I and call the symmetry g/u symmetry. The symmetry is illustrated in figure 2.8.

3. **Reflection of the electrons' coordinates on a plane that contains the internuclear axis (σ)** Since the nuclear framework of diatomic molecules has the internuclear axis as a symmetry axis, the electronic wave function has to be either symmetric or anti-symmetric with respect to the reflection of the electrons coordinates through a plane that contains the internuclear axis. The operator of this symmetry is denoted

with σ . For all states except Σ states the symmetric and the anti-symmetric wave functions are degenerate. Therefore, this symmetry is only used in the case of Σ states for labeling. If we denote this symmetry we write a '+' sign for symmetric states and a '-' sign for anti-symmetric states. The symmetry is illustrated in figure 2.8.

4. Simultaneous exchange of the electrons and the nuclei, ϵ symmetry The simultaneous exchange of the electrons and the nuclei, or ϵ symmetry, as we call it, is also a symmetry property. Since electrons are identical fermions and the nuclei are identical fermions, the wave function has to be unaltered for a simultaneous exchange of the particles. When nuclear spin and hyperfine interactions are included into the calculations, the ϵ symmetry is the only one of the presented symmetries that remains as a constant of the motion. The ϵ symmetry is connected to the g/u symmetry by the formula:

$$\epsilon = p(-1)^{I_A+I_B+I_t}. \quad (2.65)$$

Where $p = +1$ ($p = -1$) for g (u) states, I_A (I_B) is the nuclear spin of the nucleus at position A (B) and I_t is the total nuclear spin. When rotation is neglected, one only has to deal with wave functions for which $\epsilon = +1$ applies. In the case of a rotating molecule, one has to consider $\epsilon = +1$ ($\epsilon = -1$) for even (odd) values of N , the quantum number of the rotation (N is defined in section 2.3.5). For this reason we are studying positive and negative values of ϵ , despite the fact that we neglect rotation in the present calculations.

Labeling

Molecular states are labeled by combining a letter and the molecular term symbol. The letter indicates the energetic order of the electronic states and the molecular term symbol denotes the symmetry properties.

The energetic ground state is always denoted with X . The next energetically higher lying state, which is accessible through an optical transition is denoted with A , the next one with B and so on. States which are not accessible are denoted with lower case Roman letters starting from a , for the energetically lowest state, b for the next higher lying state and so on [81].

The molecular term symbol is made up by the combination of the conserved quantum numbers, also called *good* quantum numbers. For different sets of conserved quantities, different notations of the molecular term symbol are used. First, we want to describe labeling for negligible spin-orbit interaction.

In the case of negligible spin-orbit interaction Λ is a good quantum number. Moreover, the spins of the electrons are also conserved. The spins of all electrons add up to form the total spin $\vec{S} = \sum_i \vec{s}_i$, which has $2S + 1$ Zeeman states according to the possible projections of \vec{S} on an arbitrary axis. The quantity $2S + 1$ is called multiplicity. If it is 1, one speaks of singlet states. For $2S + 1 = 2$, we have doublet states, $2S + 1 = 3$ are called triplet states and so on. For the characterization of a molecular state the above presented g/u symmetry and the reflection symmetry is also used. The term symbol is arranged as

$$2S+1\Lambda_{g/u}^{(+/-)}. \quad (2.66)$$

The right superscript $+/-$ tells if the state is symmetric or anti-symmetric with respect to the reflection symmetry. It is denoted for Σ states only. Some examples of the molecular term symbol are given in figure 2.9 for the case of the Li_2 molecule.

The combination of the letter notation and the molecular term symbol looks like the following examples. $X^1\Sigma_g^+$, $a^3\Sigma_u^+$ or $B^3\Pi_u$, ...

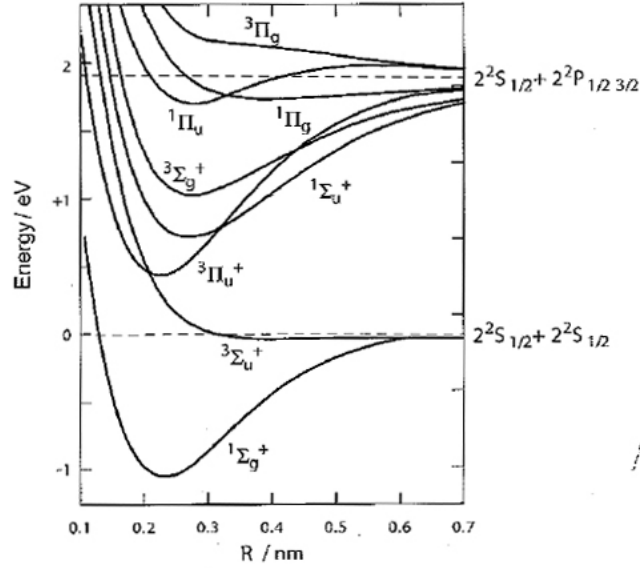


Figure 2.9: **Examples of electronic state labeling in the case of the Li_2 molecule.** The figure is taken from Ref. [81].

A further classification of an electronic state is required when effects of the spin-orbit interaction are not negligible. In that case it is helpful to distinguish between two extreme cases, namely weak and strong spin-orbit interaction.

When one considers weak spin-orbit interaction, one can describe the situation as follows. \vec{L} precesses around the internuclear axis and produces a magnetic field proportional to Λ . \vec{S} interacts with \vec{L} , but this interaction is too weak to break the coupling between \vec{L} and the internuclear axis. Thus, \vec{S} precesses around the magnetic field. The projection of \vec{S} is denoted as Σ (Do not confuse this Σ with $\Lambda = 0$ also denoted as Σ). The spin-orbit interaction Hamiltonian is given by

$$H_{so} = A\vec{L} \cdot \vec{S}. \quad (2.67)$$

The interaction couples \vec{L} and \vec{S} so that they form the resulting total electronic angular momentum vector \vec{J} . To distinguish the resulting potentials one can use the absolute value of the projection quantum number of \vec{J} on the internuclear axis denoted as $\Omega = |M_J|$. It is usually denoted as an index right besides the g/u symmetry in the molecular term symbol:

$$2S+1\Lambda_{g/u,\Omega}^{(+/-)}. \quad (2.68)$$

In the case of strong spin-orbit interaction it is possible that the coupling between \vec{L} and \vec{S} is stronger than the coupling of \vec{L} to the internuclear axis. Then \vec{L} and \vec{S} cease to be good quantum numbers. They form the vector $\vec{L} + \vec{S} = \vec{J}$, which precesses around the internuclear axis. Thus, both Λ and Σ lose their meaning and Ω is used to describe a state. One only denotes

$$\Omega_{g/u}^{(+/-)}. \quad (2.69)$$

The g/u symmetry and the reflection symmetry are still denoted. Capital Greek letters are not used anymore for the different numbers of Ω . States with different Ω are denoted by their quantum number. As examples one gets states like 0_u^+ , 0_g^- , 2_g , $1_u \dots$. In this diploma thesis, sometimes we also specify the dissociation limit of a potential in the notation. For molecular states that dissociate into the $\text{Cs}_2(6s^2S_{1/2} + 6p^2P_{1/2})$ dissociation limit, we add (${}^2P_{1/2}$) to the molecular term symbol. For molecular states that dissociate into the $\text{Cs}_2(6s^2S_{1/2} + 6p^2P_{3/2})$ dissociation limit, we add (${}^2P_{3/2}$) to the molecular term symbol. For example, we write $0_u^+({}^2P_{3/2})$ or $1_g({}^2P_{1/2})$.

Manifold of electronic states

The number of electronic states that have the same dissociation limit is always the same number as the number of possible two-atom states into which the molecule dissociates [80]. For $\text{Cs}(6s)$ we have two states since the electrons spin projection quantum number can be $+1/2$ or $-1/2$. For $\text{Cs}(6p)$ we have orbital angular momentum $l = 1$ and thus, three possible states of m_l . Multiplying those with the two possible spin alignments we get 6 states. For $\text{Cs}_2(6s + 6p)$, these considerations lead to $2 \cdot 6 = 12$ states. The g/u symmetry gives another factor of two and consequently we obtain 24 possible molecular states.

Electronic wave functions for the $\text{Cs}_2(6s + 6p)$ states at large internuclear distance

In this section we show the structure of the wave functions of the $\text{Cs}_2(6s + 6p)$ states at large internuclear distance. The orbital wave functions of the electrons are symmetrized products of the two atomic orbitals $6s$ and $6p$. The spin function is obtained by coupling the two spins. The according wave functions are given by the formula

$$\begin{aligned} |{}^{2S_t+1}\Lambda_{(g/u)}^{(+/-)}\rangle = & \left(|l_1 m_1\rangle_A^1 |l_2 m_2\rangle_B^2 + (-1)^{S_t} |l_1 m_1\rangle_A^2 |l_2 m_2\rangle_B^1 - p |l_1 m_1\rangle_B^1 |l_2 m_2\rangle_A^2 \right. \\ & \left. - p (-1)^{S_t} |l_1 m_1\rangle_B^2 |l_2 m_2\rangle_A^1 \right) |S_t M_S\rangle^{1,2}, \end{aligned} \quad (2.70)$$

where $|S_t M_S\rangle^{1,2}$ stands short for $|(s_1, s_2) S_t M_S\rangle$, the coupled spin function of the two valence electrons. S can take the values $S = 0, 1$ and its projection can be $M_S = 0$ for $S = 0$ and $M_S = 0, \pm 1$ for $S = 1$. The order of the coupling is indicated by the order of the upper right superscript ^{1,2}. The indices of the orbital wave functions A and B tell if the orbital is situated at nucleus A or nucleus B . The upper right superscript of the orbital wave functions tells if electron 1 or 2 is described by the state of the orbitals. $p = 1$ ($p = -1$) stands for g (u) states. The $\text{Cs}_2(6s + 6p)$ potentials in Hund's case a notation are ${}^3\Pi_g$, ${}^3\Pi_u$, ${}^1\Pi_g$, ${}^1\Pi_u$, ${}^3\Sigma_g^+$, ${}^3\Sigma_u^+$, ${}^1\Sigma_g^+$ and ${}^1\Sigma_u^+$. The eight potentials are

degenerated in different ways. For example, the ${}^3\Pi_u$ potential is 6 times degenerated. For completeness we also denote the wave function for all eight potentials:

$$\begin{aligned}
|{}^3\Pi_g\rangle &= \frac{1}{2}((|1\pm 1\rangle_A^1|00\rangle_B^2 - |1\pm 1\rangle_A^2|00\rangle_B^1 - |1\pm 1\rangle_B^1|00\rangle_A^2 + |1\pm 1\rangle_B^2|00\rangle_A^1)|1M_S\rangle^{1,2}) \\
|{}^3\Pi_u\rangle &= \frac{1}{2}((|1\pm 1\rangle_A^1|00\rangle_B^2 - |1\pm 1\rangle_A^2|00\rangle_B^1 + |1\pm 1\rangle_B^1|00\rangle_A^2 - |1\pm 1\rangle_B^2|00\rangle_A^1)|1M_S\rangle^{1,2}) \\
|{}^1\Pi_g\rangle &= \frac{1}{2}((|1\pm 1\rangle_A^1|00\rangle_B^2 + |1\pm 1\rangle_A^2|00\rangle_B^1 - |1\pm 1\rangle_B^1|00\rangle_A^2 - |1\pm 1\rangle_B^2|00\rangle_A^1)|00\rangle^{1,2}) \\
|{}^1\Pi_u\rangle &= \frac{1}{2}((|1\pm 1\rangle_A^1|00\rangle_B^2 + |1\pm 1\rangle_A^2|00\rangle_B^1 + |1\pm 1\rangle_B^1|00\rangle_A^2 + |1\pm 1\rangle_B^2|00\rangle_A^1)|00\rangle^{1,2}) \\
|{}^3\Sigma_g^+\rangle &= \frac{1}{2}((|10\rangle_A^1|00\rangle_B^2 - |10\rangle_A^2|00\rangle_B^1 - |10\rangle_B^1|00\rangle_A^2 + |10\rangle_B^2|00\rangle_A^1)|1M_S\rangle^{1,2}) \\
|{}^3\Sigma_u^+\rangle &= \frac{1}{2}((|10\rangle_A^1|00\rangle_B^2 - |10\rangle_A^2|00\rangle_B^1 + |10\rangle_B^1|00\rangle_A^2 - |10\rangle_B^2|00\rangle_A^1)|1M_S\rangle^{1,2}) \\
|{}^1\Sigma_g^+\rangle &= \frac{1}{2}((|10\rangle_A^1|00\rangle_B^2 + |10\rangle_A^2|00\rangle_B^1 - |10\rangle_B^1|00\rangle_A^2 - |10\rangle_B^2|00\rangle_A^1)|00\rangle^{1,2}) \\
|{}^1\Sigma_u^+\rangle &= \frac{1}{2}((|10\rangle_A^1|00\rangle_B^2 + |10\rangle_A^2|00\rangle_B^1 + |10\rangle_B^1|00\rangle_A^2 + |10\rangle_B^2|00\rangle_A^1)|00\rangle^{1,2}).
\end{aligned}$$

In the case of ${}^3\Pi$ states that have $\Omega = 0$, we make a further classification that is of use when dealing with spin-orbit interaction. ${}^3\Pi_0$ states for which the projection of the total orbital angular momentum m_L is +1 (-1) and the projection of the total electronic spin m_S is -1 (+1), are denoted with ${}^3\Pi_0(+, -)$ (${}^3\Pi_0(-, +)$):

$$\begin{aligned}
|{}^3\Pi_{g,0}(+, -)\rangle &= \frac{1}{2}(|11\rangle_A^1|00\rangle_B^2 - |11\rangle_A^2|00\rangle_B^1 - |11\rangle_B^1|00\rangle_A^2 + |11\rangle_B^2|00\rangle_A^1)|1-1\rangle^{1,2}) \\
|{}^3\Pi_{g,0}(-, +)\rangle &= \frac{1}{2}(|1-1\rangle_A^1|00\rangle_B^2 - |1-1\rangle_A^2|00\rangle_B^1 - |1-1\rangle_B^1|00\rangle_A^2 + |1-1\rangle_B^2|00\rangle_A^1)|11\rangle^{1,2}) \\
|{}^3\Pi_{u,0}(+, -)\rangle &= \frac{1}{2}(|11\rangle_A^1|00\rangle_B^2 - |11\rangle_A^2|00\rangle_B^1 + |11\rangle_B^1|00\rangle_A^2 - |11\rangle_B^2|00\rangle_A^1)|1-1\rangle^{1,2}) \\
|{}^3\Pi_{u,0}(-, +)\rangle &= \frac{1}{2}(|1-1\rangle_A^1|00\rangle_B^2 - |1-1\rangle_A^2|00\rangle_B^1 + |1-1\rangle_B^1|00\rangle_A^2 - |1-1\rangle_B^2|00\rangle_A^1)|11\rangle^{1,2})
\end{aligned}$$

2.3.5 Nuclear Motion

In this section we briefly introduce how one can treat the motion of the nuclei in order to obtain a full description of a molecule. The problem stated is the same as in equation 2.54:

$$\left[-\frac{\hbar^2}{2} \sum_{k=1}^2 \frac{1}{M_k} \vec{\nabla}_k^2 + U_m(R) - E \right] \Psi_m(\vec{R}) = 0. \quad (2.71)$$

One transforms equation 2.71 in the frame of the center of mass of the two nuclei:

$$\left[-\frac{\hbar^2}{2\mu} \vec{\nabla}_{\vec{R}}^2 + U_m(R) - E \right] \Psi_m(\vec{R}) = 0. \quad (2.72)$$

Where the nabla operator $\vec{\nabla}_{\vec{R}}^2$ acts on the coordinates of the relative vector $\vec{R} = \vec{R}_A - \vec{R}_B$ between the nuclei. In spherical coordinates, (R, θ, ϕ) , $\vec{\nabla}_{\vec{R}}^2$ is written as

$$\vec{\nabla}_{\vec{R}}^2 = \frac{1}{R^2} \frac{\partial}{\partial R} \left(R^2 \frac{\partial}{\partial R} + \frac{1}{R^2} \left\{ \frac{1}{\sin\theta} \frac{\partial}{\partial \theta} \left(\sin\theta \frac{\partial}{\partial \theta} \right) + \frac{1}{\sin^2\theta} \frac{\partial^2}{\partial \phi^2} \right\} \right) \quad (2.73)$$

By using the definition $\vec{N}^2 = - \left\{ \frac{1}{\sin\theta} \frac{\partial}{\partial \theta} \left(\sin\theta \frac{\partial}{\partial \theta} \right) + \frac{1}{\sin^2\theta} \frac{\partial^2}{\partial \phi^2} \right\}$ one obtains

$$\left(-\frac{\hbar^2}{2\mu} \frac{1}{R^2} \frac{\partial}{\partial R} \left(R^2 \frac{\partial}{\partial R} \right) + \frac{\vec{N}^2}{2\mu R^2} + U_m(R) - E \right) \Psi_m = 0. \quad (2.74)$$

Since $U(R)$ does not depend on the angular coordinates, one can write the wave function of the state $|m\rangle$ as a product of two functions, where one factor is dependent on R and the other on the angles (θ, ϕ) describing the orientation of the vector \vec{R} . $\Psi_m = \Psi_m^\nu(R) \Psi_m^r(\theta, \phi)$. We evaluate the eigenvalues of the Hamilton operator in two steps. First, we solve the eigenvalue equation of \vec{N}^2 , which only acts on the angular momentum part, for an eigenvalue λ :

$$\vec{N}^2 \Psi_m^r(\theta, \phi) = \lambda \Psi_m^r(\theta, \phi). \quad (2.75)$$

\vec{N}^2 has the same angular dependence as the square of the orbital angular momentum operator. Thus, we see from section 2.1.1 that the eigenvectors of \vec{N}^2 are the spherical harmonics $Y_{nq}(\theta, \phi)$. We obtain

$$\vec{N}^2 Y_{nq}(\theta, \phi) = \hbar^2 N(N+1) Y_{nq}(\theta, \phi). \quad (2.76)$$

This result can be used when solving the differential equation for the vibrational motion:

$$\left(-\frac{\hbar^2}{2\mu} \frac{1}{R^2} \frac{\partial}{\partial R} \left(R^2 \frac{\partial}{\partial R} \right) + \frac{\hbar^2 N(N+1)}{2\mu R^2} + U_m(R) - E \right) \Psi_m^\nu(R) = 0. \quad (2.77)$$

One often introduces an effective potential $U_{\text{eff}}(R)$ defined as

$$U_{\text{eff}}^{mN}(R) = \frac{\hbar^2 N(N+1)}{2\mu R^2} + U_m(R). \quad (2.78)$$

Harmonic approximation

Close to the minimum, which is assumed to have the position R_e , we can approximate the potential U^m by an harmonic potential. The effective potential U_{eff}^{mN} becomes

$$U_{\text{eff}}^{mN} \approx U^m(R_e) + \frac{\mu\omega_m}{2} (R - R_e)^2 + \frac{\hbar^2 N(N+1)}{2\mu R^2}. \quad (2.79)$$

ω_m is the specific potential frequency for the state $|m\rangle$. Energies of this Schrödinger equation can be denoted by $E^{mN\nu}$. For $N = 0$ one has the well known Schrödinger equation of the harmonic oscillator, shifted by a value $U^m(R_e)$, which determines the bottom of the electronic potential U^m . Thus, we get as solutions the energies $E^{m0\nu}$:

$$E^{m0\nu} = U^m(R_e) + \hbar\omega_m \left(\nu + \frac{1}{2} \right). \quad (2.80)$$

The eigenfunctions $\Psi^{m0\nu}(R)$ are the Hermite polynomials H_ν .

The effect of the rotation is frequently included by assuming that for an effective potential with $N \neq 0$ the vibrational wave functions are the same as for $N = 0$, a perturbative approach of first order. Then, the energy corrections $E^{N\nu}$ of a vibrational energy level ν due to the rotation can be calculated by averaging $\frac{\hbar^2 N(N+1)}{2\mu R^2}$ with the wave function $\Psi^{m0\nu}(R)$:

$$E^{N\nu} = \frac{\hbar^2 N(N+1)}{2\mu} \int \bar{\Psi}^{m0\nu}(R) \frac{1}{R^2} \Psi^{m0\nu}(R) dR = B_\nu N(N+1), \quad (2.81)$$

where we introduced the definition of the rotational constant B_ν . Thus, in the harmonic approximation the total energy of a molecule with the electrons in an electronic state $|m\rangle$ and the nuclei in a vibrational state Ψ^ν and a rotational state described by the quantum number N is given by

$$E^{mN\nu} = U^m(R_e) + \hbar\omega_m \left(\nu + \frac{1}{2} \right) + B_\nu N(N+1). \quad (2.82)$$

Beyond the harmonic approximation

In the harmonic approximation, the splitting between two neighboring vibrational levels is with $\hbar\omega$ constant. Realistic molecular potentials differ from a harmonic potential. The higher the value of ν , the smaller becomes the difference between two energy levels. Hence, more accurate approximations are needed, for example electronic potential as proposed by Morse or a Taylor-expansion of the electronic potentials.

2.4 Hund's Coupling Cases

With the methods discussed so far it is possible to describe the energy of a molecule inside the Born-Oppenheimer approximation. If one wants to improve the accuracy of the description, fine interactions, hyperfine interactions and interactions with the rotation also have to be included into the calculations. The additional interactions lead to couplings between the various angular momenta. The order in which the angular momenta are coupled is determined by the strength of the interactions. Hund's coupling cases classify the coupling schemes of the angular momenta in diatomic molecules for five limiting situations (cases *a* to *e*) by considering the strength of the interactions. This contributes to finding an adequate basis set, containing the approximately good quantum numbers. Here, we discuss two of the five coupling schemes that are of interest for Cs_2 . Good descriptions of all five coupling schemes can be found in Ref. [81, 79, 80].

2.4.1 Hund's Coupling Case a

In this case (see figure 2.10) one assumes that the interaction of the rotation of the nuclei \vec{N} with the electronic angular momenta (orbital and spin) is small. In addition, the coupling of \vec{L} to the internuclear axis due to the electric forces of the nuclei is stronger than the coupling between \vec{L} and \vec{S} . \vec{L} precesses around the internuclear axis. \vec{S} is coupled to \vec{L} by spin-orbit interaction and forced to precess around the internuclear axis. However, the spin-orbit coupling is not strong enough to break up the coupling between the internuclear axis and \vec{L} . Only their projections, Λ for \vec{L} and Σ for \vec{S} , are conserved. The sum of Λ and Σ is $\Omega = |\Lambda + \Sigma|$. Using the quantum number Ω , one can form a vector $\vec{\Omega} = \Omega \vec{e}_z$ along the internuclear axis. This vector is finally coupled to \vec{N} , the rotational angular momentum of the nuclei, to form $\vec{J} = \vec{N} + \vec{\Omega}$, the total electronic angular momentum of the molecule.

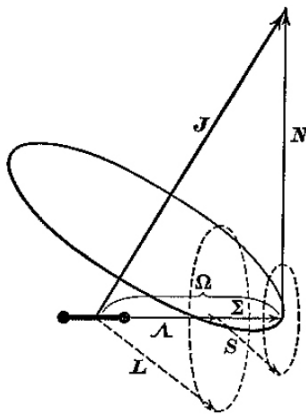


Figure 2.10: **Illustration of Hund's coupling case a.** The figure is taken from Ref. [80]

\vec{N} and $\vec{\Omega}$ rotate together around \vec{J} . The precession of \vec{L} and \vec{S} around $\vec{\Omega}$ is much faster than the precession of \vec{N} and $\vec{\Omega}$ around \vec{J} . Hund's coupling case a is called a *decoupled* basis set that is, \vec{L} and \vec{S} are both well defined and precess independently. All well defined quantum numbers are $(n, J, S, \Lambda, \Sigma, \Omega)$. n denotes other good quantum numbers like the label of a vibrational state.

We see that this case is similar to the first case of section 2.3.4 when we described how we label electronic states. Therefore, we call electronic states Hund's case a states if they possess a spin-orbit interaction that can be described by a Hund's case a coupling scheme. Potentials show the behavior of Hund's case a states when other electronic potentials that can perturb the one considered are energetically far apart compared to the energy of the spin-orbit interaction. This is usually the case for molecules made of light atoms, and for parts of the potentials that describe regions of small internuclear separation. It is not the case for a lot of molecules made up by heavy atoms, which normally have a larger spin-orbit interaction, for parts of potentials that describe the electronic energy at large separations and for regions where potentials of the same symmetry cross.

2.4.2 Hund's Coupling Case *c*

In this coupling case, the interaction between the total spin \vec{S} and the total orbital angular momentum \vec{L} is stronger than the coupling between \vec{L} and the molecular axis. Hence, \vec{L} and \vec{S} are coupled to form $\vec{J}_a = \vec{L} + \vec{S}$, the total electronic angular momentum without rotation of the nuclei (for illustration see figure 2.11).

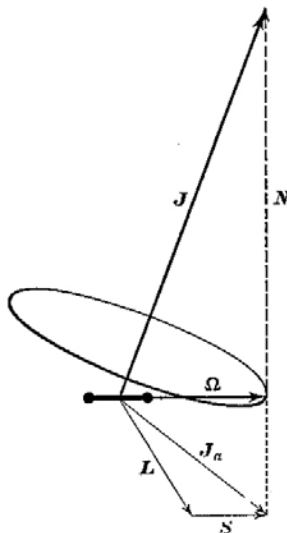


Figure 2.11: **Illustration of Hund's coupling case *c*.** The figure is taken from Ref. [80]

\vec{L} and \vec{S} do not precess independently like in case *a*. \vec{J}_a precesses fast around the internuclear axis. Its component Ω along the internuclear axis is a good quantum number. The nuclear angular momentum \vec{N} adds vectorially in order to form $\vec{J} = \vec{N} + \vec{\Omega}$. The good quantum numbers in this case are (n, J_a, J, Ω) . When nuclear rotation is not considered, Hund's case *c* describes the same situation as the second case of section 2.3.4, when we described how we label electronic states. Therefore, we call Hund's case *c* states electronic states that possess a large spin-orbit interaction and are thus described by a Hund's case *c* coupling scheme.

2.4.3 Extensions of Hund's Coupling Cases

The coupling cases that are defined by Hund do not include the nuclear spin \vec{I} . In our discussion we are using three more coupling schemes that also include the nuclear spins.

Fully coupled Hund's case *a* basis

This coupling scheme is a straightforward extension of Hund's case *a*. We assume that the hyperfine interactions are not strong enough to break up the coupling between the rotation \vec{N} and $\vec{\Omega}$ but they couple the total nuclear spin $\vec{I} = \vec{I}_1 + \vec{I}_2$ to the total electronic angular momentum \vec{J} to form the total molecular angular momentum \vec{F} ($\vec{F} = \vec{J} + \vec{I}$):

$$|n, ((\Lambda, S, \Sigma, N)J, (I_1, I_2)I)Fm_F\rangle. \quad (2.83)$$

Spin-decoupled basis

In the spin decoupled basis we use a Hund's case a state and multiply it with a function in which the two nuclear spins are coupled to a total nuclear spin; $\vec{I} = \vec{I}_1 + \vec{I}_2$. The according basis function in ket notation is

$$|n, (\Lambda, S, \Sigma, N)J, \Omega, (I_1, I_2)Im_I\rangle. \quad (2.84)$$

We use this basis function to qualitatively investigate the hyperfine structure in a perturbative approach and also in our calculations. In this case it is assumed that the coupling between \vec{J} and \vec{I} are very small so that also Ω and m_I are well defined.

Separated atom basis set

What we call the separated atom basis set is useful when all angular momenta of an atom are coupled to form the two atomic total angular momenta \vec{F}_i . The two atomic total angular momenta are then coupled to form the total molecular angular momentum \vec{F} :

$$|n, [((s_1, l_1)J_1, I_1)F_1, ((s_2, l_2)J_2, I_2)F_2]Fm_F\rangle. \quad (2.85)$$

Applying this coupling scheme is sensible when the interaction between the atoms is rather weak, so that the hyperfine interactions, in contrast to the electrostatic interaction, provide a rather large energy scale.

2.5 Spin-Orbit Interaction

So far, we assumed in a simplifying approach that the only interactions between the compounds of a molecule are the electrostatic interactions. In this section we want to include the spin-orbit interaction into the description. Spin-orbit interaction leads to the fine structure in the spectrum of molecules and atoms. It is a consequence of the interaction of the magnetic field produced by the motion of the electron with the magnetic moment associated with the electrons spin \vec{s} .

In a semi-classical way, we can introduce the spin-orbit interaction as follows: (A more detailed explanation is given in Ref. [77] or other textbooks.)

In the rest frame of the electron, the nucleus moves around it and produces a magnetic field at the position of the electron. This magnetic field \vec{B} is proportional to the electronic orbital angular momentum \vec{l} . The magnetic moment $\vec{\mu}$ of an electron due to its spin is given by $\vec{\mu} = g_s \mu_B \vec{s} / \hbar$, with g_s being the gyro magnetic moment of the electron and μ_B the Bohr magneton. The interaction energy of a magnetic dipole in a magnetic field is given by $E = -\vec{\mu} \cdot \vec{B}$. The spin-orbit interaction Hamiltonian H_{so} of a system with one electron and one nucleus is thus given by:

$$H_{so} = -\vec{\mu} \cdot \vec{B} = a(r) \vec{s} \cdot \vec{l}. \quad (2.86)$$

$a(r)$ is a factor that determines the strength of the interaction. The eigenfunction of the operator $\vec{s} \cdot \vec{l}$ are coupled wave functions of the form $|(s, l)jm_j\rangle$. The spin-orbit interaction couples the motion of the electron to its spin. This is also called *spin-orbit coupling*.

In the case of a molecule we have many electrons. Here, also the magnetic moments of the orbitals and spins of different electrons can interact with each other. We combine all these interactions in the Hamiltonian for the magnetic dipole interactions of the electrons $H_{\text{el,MD}}$:

$$H_{\text{el,MD}} = \sum_j \sum_{i < j} a_{i,j} \vec{l}_i \cdot \vec{s}_j + \sum_j \sum_{i < j} b_{i,j} \vec{l}_i \cdot \vec{l}_j + \sum_j \sum_{i < j} c_{i,j} \vec{s}_i \cdot \vec{s}_j. \quad (2.87)$$

All the terms in the sums lead to couplings between the angular momenta. The order of the couplings is determined by the coupling coefficients $a_{i,j}$, $b_{i,j}$ and $c_{i,j}$. In molecules for which Hund's case *a* applies, the $b_{i,j}$ and $c_{i,j}$ are larger than the $a_{i,j}$. In that case first the orbital angular momenta \vec{l}_i couple and form $\vec{L} = \sum_i \vec{l}_i$ and the spins \vec{s}_i couple to form $\vec{S} = \sum_i \vec{s}_i$. As a consequence, it is sufficient to approximate the spin-orbit interaction by an interaction between \vec{L} and \vec{S} :

$$H_{\text{so}} = A \vec{L} \cdot \vec{S}. \quad (2.88)$$

A is the coupling constant and approximates the effect of the $a_{i,j}$ of formula 2.87. The diagonal matrix elements of H_{so} are

$$\langle (\Lambda, (\Sigma,)S)\Omega, n | H_{\text{so}} | (\Lambda, (\Sigma,)S)\Omega, n \rangle = A \Lambda \Sigma. \quad (2.89)$$

The formula is so simple because only the components of \vec{L} and \vec{S} that are parallel to the internuclear axis do not vanish. Due to this interaction, a potential described by the quantum numbers $(\Lambda, \Sigma, S\Omega, n)$ splits up into components of different Ω . Moreover, the splitting is equal. We can observe this case in the spectrum of the $\text{Cs}_2(6s + 6p)$ states, as shown in figure 2.12. In panel **a** the plot of the spin-orbit splitting of the $b^3\Pi_u$ state (continuous lines) and of the Hund's case *a* potential that is not splitted (dashed line) is shown. Up to about $15a_0$, equation 2.89 applies. The splitting is equal, where the $^3\Pi_{u,2}(\Lambda = 1, \Sigma = 1)$ potential is shifted by a value $+A$ and the $^3\Pi_{u,0}(\Lambda = 1, \Sigma = -1)$ potential is shifted by the value $-A$ from the $b^3\Pi_u$ potential. The $^3\Pi_{u,1}(\Lambda = 1, \Sigma = 0)$ potential is not shifted because $\Sigma = 0$. For larger values of R , the potentials are perturbed by other potentials and thus cannot be described by $\vec{L} \cdot \vec{S}$ -coupling anymore.

Where the spin-orbit interaction is of the same magnitude as the splitting between two diabatic potentials, two potentials of the same symmetry perturb each other. In such cases it is better to describe the states using a Hund's case *c* basis set. In the description of Cs_2 such cases occur frequently. In the next paragraph, we show how we simulate the coupling in the case of Cs_2 .

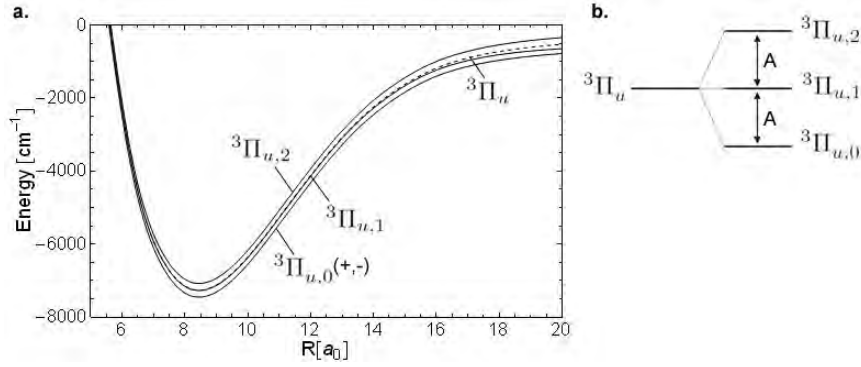


Figure 2.12: **Shown is the spin-orbit splitting of the $b^3\Pi_u$ potential.** In **a** the potentials are plotted. The continuous lines are curves with spin-orbit interaction and the dashed line is the potential of the unsplit b -state. For small internuclear separation the splitting is equal, whereas for larger values of R perturbations to this simple case are visible. **b** illustrates the equal splitting of the three states.

2.5.1 Spin-Orbit Interaction in Cs_2

We first consider the spin-orbit interaction in the cesium atom. As mentioned in section 2.2, cesium has one valence electron in the cases that we are considering ($\text{Cs}(6s), \text{Cs}(6p)$). This means that all electrons except the valence electron are in closed shells. The spin-orbit interactions $a_{i,i}\vec{l}_i \cdot \vec{s}_i$ for electrons in closed shells vanish to first order. Moreover, the spin-orbit interaction of the valence electron with the electrons in closed shells ($a_{i,j}\vec{l}_i \cdot \vec{s}_j$) behaves like an effective one-particle spin-orbit potential, i.e. like the spin-orbit interaction of an electron in the field of an *effective* nucleus, where this *effective* nucleus is made up by the real nucleus and the closed shell electrons[85]. Thus, the spin-orbit interaction for the considered configurations in a cesium atom is given by:

$$H_{\text{so}} = a_1(r)\vec{l}_1 \cdot \vec{s}_1, \quad (2.90)$$

where index 1 means the valence electron. One has $l = 0, 1$ for the s or p state. a_1 includes the effects of spin-orbit interactions of the form $\vec{l}_1 \cdot \vec{s}_1$ as well as a suitable average of the spin-orbit interactions of the form $\vec{l}_i \cdot \vec{s}_j$. We also assume that a_1 is spherically symmetric and one can show that it is proportional to $\frac{1}{r^3}$, with r being the distance between electron and nuclei. The resulting first order energy corrections are

$$\langle 6, (l, s = 1/2)jm_j | a_1\vec{l}_1 \cdot \vec{s}_1 | 6, (l, s = 1/2)jm_j \rangle = \langle a_1 \rangle \hbar^2 / 2 [j(j+1) - l(l+1) - 3/4]. \quad (2.91)$$

$\langle a_1 \rangle$ is the mean value of a_1 , averaged over the electronic radial coordinate. Of course the correction of s -states is zero because $l = 0$. Only $l = 1$ gives corrections to first order. $\langle a_1 \rangle$ can be determined by comparison with experimental values. The $6p$ state is splitted into the two states $\text{Cs}(6^2P_{1/2})$ and $\text{Cs}(6^2P_{3/2})$ by the value $\Delta = 554.039 \text{ cm}^{-1}$. The $\text{Cs}(6^2P_{1/2})$ state is shifted by $\Delta E_{1/2} = -\frac{2}{3}\Delta$ and the $\text{Cs}(6^2P_{3/2})$ is shifted by $\Delta E_{3/2} = +\frac{1}{3}\Delta$ from the unsplit state $\text{Cs}(6p)$.

The next step is investigating the case of the $\text{Cs}_2(6s + 6p)$ potentials. To do so, it is helpful to think of two cesium atoms and consider what happens when they approach

each other. For large separations, the two atoms influence each other only little and the spin-orbit interaction is dominated by the spin-orbit interactions of the valence electrons with closed shell electrons and the nucleus. If we assume that the molecule can be treated as two slightly interacting atoms, the spin-orbit interaction has the form:

$$H_{\text{so}} = a_{1,1}(r_1)\vec{l}_1 \cdot \vec{s}_1 + a_{2,2}(r_2)\vec{l}_2 \cdot \vec{s}_2 + a_{1,2}(r_{12})\vec{l}_1 \cdot \vec{s}_2 + a_{2,1}(r_{12})\vec{l}_2 \cdot \vec{s}_1. \quad (2.92)$$

The last two terms describe the interaction of the spin of an electron with the magnetic field created by the motion of the other electron. These two last terms are often neglected. Especially when one considers the atoms to be well separated, these terms are small.

When the last two terms of equation 2.92 are neglected, the spin-orbit interaction is

$$H_{\text{so}} = a_{1,1}(r)\vec{l}_1 \cdot \vec{s}_1 + a_{2,2}(r)\vec{l}_2 \cdot \vec{s}_2. \quad (2.93)$$

We investigate the effect of this form of spin-orbit interaction in a perturbational way. For this purpose, we use the wave functions of $\text{Cs}_2(6s + 6p)$ states given at the end of section 2.3.4 to calculate the matrix elements of H_{so} . The form of the wave functions already suggests that one term of H_{so} gives zero depending whether valence electron 1 or 2 is in the $6s$ state. The other is proportional to $\Delta/3$, which determines the spin-orbit splitting of the single cesium atom. H_{so} is not diagonal in the Hund's case a basis set. Thus, Hund's case a states with the same value of Ω and g/u symmetry can be coupled through H_{so} . A striking example for such a case is the formation of the $(A - b)0_u^+$ excited states from the $A^1\Sigma_u^+$ and the $b^3\Pi_u$ Hund's case a potentials, as illustrated in figure 2.13.

When spin-orbit interaction is not considered, one finds that the $A^1\Sigma_u^+$ potential crosses the $b^3\Pi_u$ potential at about $11a_0$ (red dashed lines in figure 2.13). We remember that the $b^3\Pi_u$ potential is sixfold degenerate. Due to spin-orbit interaction, the $A^1\Sigma_u^+$ state can couple to the $b^3\Pi_{u,0}^+(+, -)$ and the $b^3\Pi_{u,0}^+(-, +)$ states in order to form the $0_u^+(^2P_{1/2})$ and the $0_u^+(^2P_{3/2})$ Hund's case c states (two of the black continuous lines in figure 2.13). In contrast to the Hund's case a states, the Hund's case c states perform an avoided crossing. In between the $0_u^+(^2P_{1/2})$ and the $0_u^+(^2P_{3/2})$ potential we have also drawn the $0_u^-(^2P_{1/2})$ potential. It results from spin-orbit coupling between $b^3\Pi_{u,0}^+(+, -)$, $b^3\Pi_{u,0}^+(-, +)$ states and the energetically far separated $^3\Sigma_u^+$ potential. Due to the large energy difference of the $b^3\Pi$ and the $^3\Sigma_u^+$ potentials, the coupling is negligible and the $0_u^-(^2P_{1/2})$ potential coincides with the $b^3\Pi_{u,0}$ potential.

With spin-orbit interaction, the $A^1\Sigma_u^+$ and the $b^3\Pi_{u,0}^+(-, +)$ potentials interact strongly. As a consequence they perform an avoided crossing. The other $b^3\Pi_u$ states are not perturbed by the A state (see figure 2.12). They show a splitting that can be described by $\vec{L} \cdot \vec{S}$ -coupling. To illustrate this fact, we also include the potential of the $^3\Pi_{u,0}(+, -)$ state into the graph. All curves that include spin-orbit interaction are drawn in black.

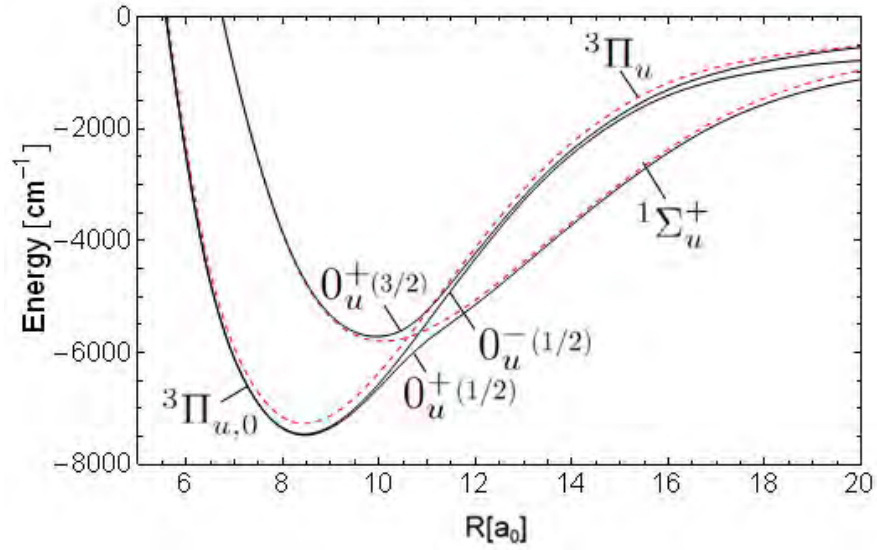


Figure 2.13: **Effect of the spin-orbit interaction on the $A^1\Sigma_u^+$ and the $b^3\Pi_u$ Hund's case a potentials.** The $A^1\Sigma_u^+$ and the $b^3\Pi_u$ potentials, which do not include spin-orbit interaction, are drawn in red, dashed lines. They cross each other at about $R \approx 11a_0$. The $0_u^+(^2P_{1/2})$ and the $0_u^+(^2P_{3/2})$ potentials result from spin-orbit coupling of the A and the b states and form the $(A - b)0_u^+$ system. The $0_u^+(^2P_{1/2})$ and the $0_u^+(^2P_{3/2})$ potentials perform a large avoided crossing due to spin-orbit coupling. The $0_u^-(^2P_{1/2})$ potential, located in between $0_u^+(^2P_{1/2})$ and $0_u^+(^2P_{3/2})$, is formed by spin-orbit interaction of the $b^3\Pi_u$ and the $^3\Sigma_u^+$ states. However, $b^3\Pi_u$ and the $^3\Sigma_u^+$ are energetically far separated. Hence, $0_u^-(^2P_{1/2})$ is not shift away from the $b^3\Pi_{u,0}$ potential. All potentials that include spin-orbit interaction are drawn with black, continuous lines.

2.6 Molecular Hyperfine Structure

This last section of the Chapter *Theory* finally deals with the hyperfine structure of diatomic molecules. The hyperfine structure is the result of small corrections to the adiabatic potentials, which further lift the degeneracy and thus induce an additional splitting of the potentials. The origin of the hyperfine Hamiltonian lies in the interaction between the electric and magnetic multipoles of a nucleus and the electric and magnetic fields created by the electrons and the other nuclei.

2.6.1 Hyperfine Structure of Homonuclear Diatomic Molecules

First, it has to be appreciated that, if not stated differently, the ideas of the section are adapted from an article of Broyer et al. (1978) [71].

In a fixed electronic and vibrational state we describe the hyperfine structure with the Hamiltonian H_{hf} . It can be decomposed into three parts:

$$H_{\text{hf}} = H_{\text{hf}}(A) + H_{\text{hf}}(B) + H_{\text{hf}}(AB). \quad (2.94)$$

The first part $H_{\text{hf}}(A)$ describes the interactions between the electrons and the nucleus at the position \vec{R}_A . The second part $H_{\text{hf}}(B)$ describes the interactions between the electrons and the nucleus situated at the position \vec{R}_B , the last part $H_{\text{hf}}(AB)$ stands for interactions between the two nuclei. Of course the first term is constituted by the same interactions as the second term, the only difference is that the nucleus is at another position.

Firstly, we concentrate on $H_{\text{hf}}(A)$ the interactions between all the electrons and nucleus A (all the arguments are the same for $H_{\text{hf}}(B)$). Here the electric and magnetic multipoles of the nuclei interact with the fields created by all the electrons. Due to parity conservation inside the nuclei, only the even electronic ones and the odd magnetic multipoles are non vanishing [71]. Thus, $H_{\text{hf}}(A)$ can be written as

$$H_{\text{hf}}(A) = H_{\text{MD}}(A) + H_{\text{EQ}}(A) + H_{\text{MO}}(A) + H_{\text{EH}}(A) + \dots \quad (2.95)$$

$H_{\text{MD}}(A)$ stands for magnetic dipole interaction, $H_{\text{EQ}}(A)$ for electric quadrupole interactions, $H_{\text{MO}}(A)$ for magnetic octupole interaction and $H_{\text{EH}}(A)$ is the Hamiltonian for the electric hexapole interactions. We only explicit the first two terms, since they are responsible for the main energy shifts.

The magnetic dipole interaction between all the electrons and a nucleus, $H_{\text{MD}}(A)$

We begin with the magnetic dipole interaction $H_{\text{MD}}(A)$. It consists of three terms:

$$H_{\text{MD}}(A) = H_{\text{II}}(A) + H_{\text{SI}}(A) + H_{\text{FC}}(A). \quad (2.96)$$

The first term describes the interaction between the orbital angular momenta of the electrons and a nuclear spin. The explicit form is

$$H_{\text{II}} = \sum_e -2g_{I_A}\mu_B\mu_N \left(\frac{\mu_0}{4\pi}\right) \frac{\vec{I}_A \cdot \vec{l}_e(A)}{r_{Ae}^3}. \quad (2.97)$$

The summation is over all electrons. g_{I_A} is the Landé factor of the free nucleus. I_A is the spin of the considered nucleus. μ_0 is the vacuum permeability. μ_B and μ_N are the Bohr magneton and the nuclear magneton respectively. The vector connecting the nucleus and the electron is $\vec{r}_{Ae} = \vec{r}_e - \vec{r}_A$, where \vec{r}_e is the position of electron e and \vec{r}_A is the position of nucleus A . Finally, $\vec{l}_e(A) = \vec{r}_{Ae} \times \vec{p}_e$ is the angular momentum of the electron e relative to the position of nucleus A and \vec{p}_e is its momentum.

The term $H_{\text{SI}}(A)$ is the interaction between the electrons' spins and the nucleus A :

$$H_{\text{SI}} = \sum_e -g_s g_{I_A} \mu_B \mu_N \left(\frac{\mu_0}{4\pi}\right) \frac{3(\vec{s}_e \cdot \vec{r}_{Ae}) - (\vec{I}_A \cdot \vec{s}_e)(\vec{r}_{Ae} \cdot \vec{r}_{Ae})}{r_{Ae}^5}, \quad (2.98)$$

with g_s being the Landé factor of the free electron. \vec{s}_e is the spin of the electron e .

The Fermi-contact interaction is described by the last of the three terms, $H_{\text{FC}}(A)$:

$$H_{\text{FC}}(A) = \sum_e -g_s g_{I_A} \mu_B \mu_N \left(\frac{\mu_0}{4\pi}\right) \frac{8\pi}{3} \vec{I}_A \cdot \vec{S}_e \delta(r_{Ae}). \quad (2.99)$$

It is important to see that all three terms of $H_{\text{MD}}(A)$ have the same tensorial form:

$$\vec{O}_{el}^1(\vec{j}_e) \cdot \vec{I}_A^1, \quad (2.100)$$

which is a scalar product of two rank 1 operators, where $\vec{j}_e(A) = \vec{l}_e(A) + \vec{s}_e$ is the total angular momentum of the electron e . The first one, $\vec{O}_{el}^1(\vec{j}_e)$, depends on the coordinates of the electrons and the second, \vec{I}_A^1 , on the nuclear spin. The two operators can be written as spherical tensor operators $V^1(\vec{j}_e)$ and $Q^1(\vec{I}_A)$. In this form the scalar product can be written as

$$V^1(\vec{j}_e) \cdot Q^1(\vec{I}_A) = \sum_e \sum_q (-1)^q Q_q^1(\vec{I}_A) V_{-q}^1(\vec{j}_e(A)). \quad (2.101)$$

The representation in spherical tensor operators is preferable, so that the Wigner-Eckart theorem can be used. It runs as

$$\langle \tau', j' m' | T_q^k | \tau, j m \rangle = (-1)^{j'-m'} \begin{pmatrix} j' & k & j \\ -m' & q & m \end{pmatrix} \langle \tau', j' || T^k || \tau, j \rangle. \quad (2.102)$$

$\langle \tau', j' || T^k || \tau, j \rangle$ is called reduced matrix element. It is a number that contains the information about radial dependence of the matrix elements. τ denotes all other quantum numbers except j and m . The big advantage of the use of spherical tensors and the Wigner-Eckart theorem is that we can divide the calculation of a matrix element into a purely radial and a purely angular part. The two parts can then be treated separately.

In a spherical tensor operator form, $H_{\text{MD}}(A)$ reads as

$$H_{\text{MD}}(A) = \sum_e \sum_q (-1)^q Q_q^1(\vec{I}_A) T_{-q}^1(\vec{j}_e(A)), \quad (2.103)$$

where T^1 combines all the three terms of $H_{\text{MD}}(A)$.

The electric quadrupole interaction between all the electrons and a nucleus, $H_{\text{EQ}}(A)$

The second term in the discussion is the electric quadrupole term $H_{\text{EQ}}(A)$:

$$H_{\text{EQ}}(A) = \sum_e \sum_q (-1)^q Q_q^2(A) V_{e,-q}(A), \quad (2.104)$$

where $Q_q^2(A)$ is the electric quadrupole of nucleus A , defined as

$$Q_q^2(A) = \sqrt{\frac{4\pi}{5}} \sum_p e_p r_p^2 Y_q^2(\theta_p, \phi_p). \quad (2.105)$$

r_p, θ_p, ϕ_p are the radial and angular coordinates of the protons p inside the nucleus A . The field created by the electrons at the position of nucleus A can be written as

$$V_{e,q}^2(A) = \sqrt{\frac{4\pi}{5}} \frac{e}{4\pi\epsilon_0 r_{Ae}^3} Y_q^2(\theta_{Ae}, \phi_{Ae}), \quad (2.106)$$

with θ_{Ae} and ϕ_{Ae} being the angular coordinates of the vector \vec{r}_{Ae} .

To make use of the Wigner-Eckart theorem, we rewrite $H_{\text{EQ}}(A)$ as

$$H_{\text{EQ}}(A) = \sum_e \sum_q (-1)^q Q_q^2(\vec{I}_A) V_{e,-q}(\vec{j}_e(A)), \quad (2.107)$$

with $Q_q^2(\vec{I}_A)$ and $V_{e,-q}(\vec{j}_e(A))$ being spherical tensor operators of rank 2.

The hyperfine interactions between the nuclei, $H_{\text{hf}}(A, B)$

$H_{\text{hf}}(A, B)$ is the direct hyperfine interaction between the two nuclei. We have a magnetic dipole term $H_{\text{MD}}(A, B)$. It consists of

$$H_{\text{MD}}(A, B) = H_{\text{IN}}(A, B) + H_{\text{I}_1\text{I}_2}(A, B), \quad (2.108)$$

with $H_{\text{IN}}(A, B)$ the nucleus spin - nucleus orbit, and nucleus spin - other nucleus orbit interaction (also called nucleus spin-rotation interaction). $H_{\text{I}_1\text{I}_2}(A, B)$ is the direct nucleus spin - nucleus spin interaction.

We also have an electric quadrupole term $H_{\text{EQ}}(A, B)$. It is the interaction between the quadrupole of one nucleus with the electric field created by the charge of the other

nucleus. There are also interactions between the two electric quadrupoles $H_{Q_1, Q_2}(A, B)$ and higher order electric and magnetic multipole interactions $H_{MO}(A, B)$, $H_{EH}(A, B), \dots$

Since we do not consider rotation and the terms of $H_{\text{hf}}(A, B)$ are generally some orders of magnitude smaller than the energy corrections arising from the terms presented in 2.6.1 and 2.6.1 we neglect their effects in the next part of the discussion.

2.6.2 Calculation of the Matrix Elements

We calculate the matrix elements of H_{hf} in a fully coupled Hund's case a basis, which reads as $|\nu, S\Lambda\Sigma\Omega J(I_1 I_2) I F M_F\rangle$. ν stands for a vibrational level. In section 2.6.1 we have determined H_{hf} to be $H_{\text{hf}} = H_{\text{MD}}(A) + H_{\text{MD}}(B) + H_{\text{EQ}}(A) + H_{\text{EQ}}(B)$ since we neglect higher order terms and terms of the form $H(A, B)$. Moreover, we have seen that the presented terms can be written by the use of spherical tensors. H_{MD} is of rank 1 and H_{EQ} of rank 2. We rewrite H_{hf} as a sum of the form:

$$H_{\text{hf}} = \sum_{\alpha=1}^2 \sum_k H^k(\alpha). \quad (2.109)$$

α is the sum over the two nuclei. k ranges from 1 to 2 and numbers the ranks of the tensors. By application of the Wigner-Eckart theorem, one can calculate the matrix elements of the $H^k(\alpha)$. They are

$$\begin{aligned} &\langle S' \Lambda' \Sigma' \Omega' \nu' J'(I_1 I_2) I' F' M'_F | H^k(\alpha) | S \Lambda \Sigma \Omega \nu J(I_1 I_2) I F M_F \rangle = \\ &\delta_{F, F'} \delta_{M_F, M'_F} (-1)^{k+I_1+I_2+F+I+I'+J+J'} f_k(i, \Omega', \Omega) [(2I+1)(2I'+1)(2J+1)(2J'+1)]^{1/2} \\ &\begin{pmatrix} J' & k & J \\ -\Omega & \Delta\Omega & \Omega \end{pmatrix} \begin{Bmatrix} I_2 & I_1 & I \\ k & I' & I_1 \end{Bmatrix} \begin{Bmatrix} F & I' & J' \\ k & J & I \end{Bmatrix}, \end{aligned} \quad (2.110)$$

with $\Delta\Omega = \Omega' - \Omega$ and $f_k(i, \Omega', \Omega)$ generally also depends on S , Λ , Σ and ν . It mainly contains the reduced matrix element for the various interactions. Thus, here is the dependence of the hyperfine structure on the internuclear distance included. Details for $f_k(i, \Omega', \Omega)$ are given in [71].

2.6.3 Approximate Matrix Elements

We can approximate the matrix elements of the hyperfine interactions, by using perturbation theory of first and second order. This will be helpful, when we interpret the results of our calculations. We use the spin-decoupled basis set:

$$|(S, L) J_t \Omega \epsilon\rangle |I_t m_I\rangle. \quad (2.111)$$

Moreover, we perform the perturbational approach only for the magnetic dipole part of H_{hf} , as we think that the main contribution of the hyperfine structure comes from the Fermi-contact interaction.

First order of perturbation

In first order one calculates diagonal matrix elements of the general form $\Delta E^1 = \langle m | H | m \rangle$. With the basis set that we use we get for ΔE_{MD}^1 the expression:

$$\Delta E_{\text{MD}}^1 = \langle I_t m_I | \langle (S, L) J_t \Omega \epsilon | H_{\text{MD}} | (S, L) J_t \Omega, \epsilon \rangle | I_t m_I \rangle. \quad (2.112)$$

In spherical tensor notation $H_{\text{MD}} = \sum_e \sum_q (-1)^q Q_q^1(\vec{I}_A) T_{-q}^1(\vec{j}_e(A))$ and equation 2.112 becomes

$$\Delta E_{\text{MD}} = \sum_q (-1)^q \langle (S, L) J_t \Omega \epsilon | \sum_e T_{-q}^1(\vec{j}_e(A)) | (S, L) J_t \Omega, \epsilon \rangle \langle I_t m_I | I_q^{(1)} | I_t m_I \rangle. \quad (2.113)$$

Now we apply the Wigner-Eckart theorem. The sum over q vanishes except for $q = 0$ because we calculate only diagonal elements in first order perturbation theory. Thus, we obtain for ΔE_{MD} :

$$\begin{aligned} \Delta E_{\text{MD}} = & (-1)^{J_t - \Omega} \begin{pmatrix} J_t & 1 & J_t \\ -\Omega & 0 & \Omega \end{pmatrix} \langle (S, L) J_t \Omega \epsilon | T^1 | (S, L) J_t \Omega \epsilon \rangle \\ & (-1)^{I_t - m_I} \begin{pmatrix} I_t & 1 & I_t \\ -m_I & 0 & m_I \end{pmatrix} \langle I_t \Omega \epsilon | I^1 | I_t \Omega \epsilon \rangle \end{aligned} \quad (2.114)$$

Where we have included the sum over e in T^1 . A $3j$ -symbol of the form $\begin{pmatrix} j & 1 & j \\ -m_j & 0 & m_j \end{pmatrix}$ can be calculated with the formula

$$(-1)^{j - m_j} \begin{pmatrix} j & 1 & j \\ -m_j & 0 & m_j \end{pmatrix} = \frac{m_j}{\sqrt{j(j+1)(2j+1)}}. \quad (2.115)$$

If $\Omega \neq 0$, ΔE_{MD}^1 is proportional to m_I . Hence, the first order energy correction $\Delta E_{\text{MD}}^1 = 0$ if $\Omega = 0$. Then, second order perturbation theory has to be considered.

Second order of perturbation

In second order perturbation theory, the matrix elements that have to be considered are of the form:

$$\Delta E_{\text{MD}}^2 = \sum_{\bar{S}, \bar{L}, \bar{J}_t, \bar{\Omega}, \bar{\epsilon}, \bar{I}_t, \bar{m}_I} \frac{|\langle I_t m_I | \langle (S, L) J_t \Omega \epsilon | H_{\text{MD}} | (\bar{S}, \bar{L}) \bar{J}_t \bar{\Omega}, \bar{\epsilon} \rangle | \bar{I}_t \bar{m}_I \rangle|^2}{E - \bar{E}}. \quad (2.116)$$

In principle any states, except states of different ϵ and m_F , can be coupled by the hyperfine interaction. However, the energy difference is in the denominator, therefore

states that are energetically far away from the considered state cannot act as a perturber. We only have to consider energetically close states. The sum in equation 2.117 is only adding terms that lie close to the considered state and the perturbational effect of the other states is neglected. The denominator is also determining the sign of the energy shift. If the perturbing state is energetically higher, the shift is negative. If the state is lower in energy, the shift is positive.

If $\Omega \neq 0$, we get contribution from first order perturbation terms and second order perturbation effects can, in general, be neglected. Therefore, we assume that $\Omega = 0$. Knowing that I is diagonal in the basis I_t , we obtain for ΔE_{MD}^2

$$\Delta E_{\text{MD}}^2 = \sum_{\text{perturbing states}} \frac{\delta(I_t, \bar{I}_t)}{E - \bar{E}} \left[(-1)^{J_t - \Omega} \begin{pmatrix} J_t & 1 & \bar{J}_t \\ 0 & \Delta\Omega & \bar{\Omega} \end{pmatrix} \langle J_t \| T^1 \| \bar{J}_t \rangle \right. \\ \left. (-1)^{I_t - m_I} \begin{pmatrix} I_t & 1 & I_t \\ -m_I & 0 & m_I \end{pmatrix} \langle I_t \| I \| I_t \rangle \right]^2. \quad (2.117)$$

In general, the result is complicated, but in the case of $\bar{\Omega} = 0$ we find that ΔE_{MD}^2 is proportional to m_I^2 .

Summary of the matrix element properties

In the case of $\Omega \neq 0$, first order corrections are generally more important than second order corrections. The energy splitting is proportional to m_I .

In the case of $\Omega = 0$ first order contributions vanish. Second order contributions might be important. Only states that lie energetically close can perturb each other. The energy difference determines the sign of energy shifts. The energy corrections are complicated if the perturbing state has $\bar{\Omega} \neq 0$. If the perturbing states have $\bar{\Omega} = 0$, the energy corrections are proportional to m_I^2 .

3 Model

In this section we present our model of the Cs_2 molecule. The main point is that we assume that the molecular fine and hyperfine structure are determined by the atomic fine and hyperfine interactions. This implies that the Hamiltonian that describes the energy of the hyperfine structure does not depend on the internuclear distance.

3.1 Hamiltonian

First, we set up the Hamiltonian. As explained in Chapter 2, within the adiabatic approximation the Schrödinger equation for the electronic states is

$$\hat{H}_0 |m\rangle = U_m(R) |m\rangle, \quad (3.1)$$

where $H_0 = T_e + V$ is the sum of the T_e , kinetic energy of the electrons and V , the sum of the potentials between the charged particles. If we want to add fine and hyperfine structure, we add it as a new term in H_0 . Thus, we obtain H_e , the Hamiltonian including also fine and hyperfine interactions:

$$H_e = T_e + V + H_f + H_{\text{hf}} = H_0 + H_f + H_{\text{hf}}, \quad (3.2)$$

with H_f and H_{hf} standing for the fine and hyperfine interactions. To model the fine structure we use spin-orbit interaction only. Thus, we write H_{so} instead H_f .

In the following subsections, we describe how to model the three parts of H_e .

3.1.1 Hyperfine and Spin-Orbit Interactions

To model the hyperfine structure, we assume that the effects that originate from the nature of the molecule, like the interactions between the valence electrons, can be neglected. H_{hf} is therefore the same as the Hamiltonian for the hyperfine interactions of the separated atoms:

$$H_{\text{hf}} = H_{\text{hf}}^A + H_{\text{hf}}^B, \quad (3.3)$$

where H_{hf}^α is the hyperfine structure of the free atom $\alpha = A, B$. We also make assumptions on the form of the wave function of the electronic cloud. For the calculations of the matrix elements of H_{hf} and H_{so} , we assume that the wave functions are the same as in the case of separated atoms and can be approximated by the use of the atomic $6s$ and $6p$ orbitals as denoted in section 2.3.4. Building on these two assumptions, H_{hf} is diagonal in the separated atom basis set. Thus, we first set up the separated atom basis

set. This is achieved by coupling the angular momenta \vec{s} , \vec{l} and \vec{I} of the individual atoms and after this, coupling the two individual atomic wave functions in order to form the molecular wave function. For the $6s$ atom we denote the orbital by the coupled wave function:

$$|((s_1 l_1) j_1 I_1) F_1 m_{F_1}\rangle. \quad (3.4)$$

The valence electrons spin couples to its orbital angular momentum to form j_1 , which couples to I_1 in order to form the total angular momentum F_1 . We also assume that the radial dependence is included in this wave function. It is given by the radial wave function of the $6s$ state. Of course $s_1 = 1/2$ and $l_1 = 0$ and thus, $j_1 = 1/2$ for the s -state.

Similarly, we can construct the basis function of the atom in the p -state ($l_2 = 1$):

$$|((s_2 l_2) j_2 I_2) F_2 m_{F_2}\rangle. \quad (3.5)$$

The molecular basis is then formed by coupling the two atomic basis sets:

$$|(((s_1 l_1) j_1 I_1) F_1, ((s_2 l_2) j_2 I_2) F_2) F m_F, \epsilon\rangle \equiv |[F_1, (j_2 I_2) F_2] F m_F, \epsilon\rangle. \quad (3.6)$$

ϵ is the quantum number of the symmetry due to the simultaneous exchange of electrons and nuclei.

With the approximations stated in the beginning, we can determine the effect of H_{hf} on our basis functions:

$$\begin{aligned} H_{\text{hf}} |[F_1, (j_2 I_2) F_2] F m_F, \epsilon\rangle &= (H_{\text{hf}}^A + H_{\text{hf}}^B) |[F_1, (j_2 I_2) F_2] F m_F, \epsilon\rangle \\ &= (\Delta E_{\text{hf}}^A(F_1) + \Delta E_{\text{hf}}^B(F_2, j_2)) |[F_1, (j_2 I_2) F_2] F m_F, \epsilon\rangle. \end{aligned} \quad (3.7)$$

$\Delta E_{\text{hf}}^\alpha$ are the energy corrections of the individual atoms. The splitting of the $6s$ and the $6p$ energy levels are given in section 2.2. The hyperfine energy correction of the different spin-orbit splitted states can be evaluated by the use of the Landé formula (which follows from the identity $\vec{j} \cdot \vec{I} = \frac{1}{2}(\vec{F}^2 - \vec{I}^2 - \vec{j}^2)$):

$$\Delta E_{\text{hf}} = \frac{A}{2} [F_i(F_i + 1) - j_i(j_i + 1) - I_i(I_i + 1)]. \quad (3.8)$$

It shows how the energy of the previously degenerated states is shifted when hyperfine interactions are considered. With the interval rule, which follows from formula 3.8,

$$\Delta E_{F_i+1} - \Delta E_{F_i} = A(F_i + 1), \quad (3.9)$$

one can determine the constant A from experimental values and calculate the energy corrections ΔE_{hf} as a function of F_1 for states of $6s$ atom and of j_2 and F_2 for $6p$ states.

The energy corrections arising from spin-orbit interaction are implemented in a similar way. We make the same assumptions as in the case of hyperfine structure. The wave

function of the electrons is given by combinations of atomic wave functions $[[F_1, (j_2 I_2) F_2] F m_F \epsilon]$ again. The Hamiltonian of the spin-orbit interaction is the one of section 2.5.1:

$$H_{\text{so}} = a_{1,1}(r)\vec{l}_1 \cdot \vec{s}_1 + a_{2,2}(r)\vec{l}_2 \cdot \vec{s}_2. \quad (3.10)$$

Using the identity

$$\vec{l} \cdot \vec{s} = \frac{1}{2}[j^2 - l^2 - s^2], \quad (3.11)$$

we can determine the effect of H_{so} . It is

$$H_{\text{so}} |[F_1, (j_2 I_2) F_2] F m_F \epsilon] = E_{\text{so}}(j_2) |[F_1, (j_2 I_2) F_2] F m_F \epsilon], \quad (3.12)$$

where $E_{\text{so}}(3/2) = 1/3\Delta$ for $j_2 = 3/2$ and $E_{\text{so}}(1/2) = -2/3\Delta$ for $j_2 = 3/2$. $\Delta = 554.039 \text{ cm}^{-1}$, it is the energy difference between the $\text{Cs}(6^2P_{1/2})$ and $\text{Cs}(6^2P_{3/2})$ levels. Putting together the results enables us to denote the corrections due to spin-orbit interaction and hyperfine structure of our model. It is

$$(H_{\text{so}} + H_{\text{hf}}) |[F_1, (j_2 I_2) F_2] F m_F \epsilon] = (E_{\text{so}}(j_2) + \Delta E_{\text{hf}}^A(F_1, j_2, F_2) + \Delta E_{\text{hf}}^B(F_1, j_2, F_2)) |[F_1, (j_2 I_2) F_2] F m_F \epsilon]. \quad (3.13)$$

3.1.2 H_0 , the Electronic Hamiltonian

We describe the electronic Hamiltonian H_0 differently for *large* and *small* internuclear separations. *Large* atomic separations are those for which the internuclear distance is larger than the Leroy-radius R_c , which is defined by formula 2.60. It tells at which internuclear distance the electronic clouds of two atoms start to overlap significantly. In the case of $\text{Cs}_2(6s + 6p)$ -states one finds $R_c = 28.4a_0$. If R is larger than R_c the electronic potential can be described by the energy of two separate interacting atoms. *Small* internuclear separations are those for which R is smaller than R_c . Here we cannot talk of separated atoms anymore because the electrons have a high probability of staying close to both nuclei. To improve the connection between the two regions, we implement a part in the Hamiltonian around the Leroy-radius that is called *asymptotic exchange interaction*. It models the exchange interaction in the region where the wave functions of the atoms just start to overlap. To model H_0 , we make the following distinction of regions:

1. **very large nuclear separations** ($R > 40a_0$) The electronic potentials are approximated to be small perturbations to the energy of the atomic states. The perturbations are expressed by an expansion in inverse powers of R
2. **around the LeRoy-radius** ($20a_0 > R > 40a_0$) We add an asymptotic exchange interaction term to the expansion of case 1.
3. **small nuclear separations** ($R < 20a_0$) The wave functions of the valence electrons overlap significantly and the methods of case 1 and 2 cease to describe the problem accurately. We take results of quantum chemistry calculations to describe the electronic potentials

The three points are now explicated in more detail.

1. Very large nuclear separations ($R > 40a_0$)

For large internuclear distances we can approximate the molecule by two atoms that interact via electrostatic forces. Then, it is convenient to separate the Hamiltonian H_0 into the parts:

$$H_0 = H_A + H_B + H_{AB}. \quad (3.14)$$

H_A describes the energy of the atom in the s -state and H_B describes the energy of the atom in the p -state. They are constant. By setting our zero point of energy equal to the dissociation limit, we drop these constants. H_{AB} is the interaction between the two atoms.

Since the separation between the nuclei is very large, the interactions inside the atoms are much larger than the interactions between the atoms themselves. Hence, the interatomic forces can be included as a perturbation of the atomic Hamiltonians as presented in section 2.3.3. We use the potential given by formula 2.61:

$$H_{AB} = U(R) = \sum_n \frac{C_n}{R^n} \quad (3.15)$$

The dispersion coefficients are taken from Ref. [83] and presented in section 2.3.3. To implement H_{AB} in our calculations, we use the wave functions given at the end of section 2.3.4 and take H_{AB} as the electronic potential of the states $|^{2S+1}\Lambda_{g/u}^{(+)}\rangle$:

$$H_{AB}(\Lambda, g/u, s) \left| ^{2S+1}\Lambda_{g/u}^{(+/-)} \right\rangle = \left(\frac{C_3(\Lambda, g/u, s)}{R^3} + \frac{C_6(\Lambda, g/u, s)}{R^6} + \frac{C_8(\Lambda, g/u, s)}{R^8} \right) \left| L, m_L \right\rangle_{g/u}^{(+/-)} \left| S m_s \right\rangle. \quad (3.16)$$

2. Around the LeRoy-radius ($20a_0 > R_c > 40a_0$)

When we come closer to the LeRoy-radius the overlap between the two atoms' charge distributions starts to increase exponentially, which also increases the exchange interaction. This is considered by adding the potential V_{exch} , the asymptotic exchange interaction (see section 2.3.3), to the potential $U(R)$ of the multipole expansion. Around the LeRoy-radius, H_{AB} becomes

$$H_{AB} = \sum_n \frac{C_n}{R^n} + V_{exch}. \quad (3.17)$$

The exchange interaction may also increase the region of the validity of the above formulas beyond the LeRoy radius. It therefore prepares the potentials to be more smoothly connected with the potentials taken in region 3.

3. Small nuclear separations ($R < R_c$)

In this region the analytical expressions listed above are not valid anymore. The two atoms' wave functions overlap significantly and the valence electrons cannot be considered as belonging to one individual atom. Moreover, the effects of the interactions between the valence electrons and the other electrons also increase. In the previous cases 1 and 2 we did only looked at the valence electrons. To include these effects, we use numeric data gained by quantum chemistry calculations. This data is taken from Ref. [86, 87, 88, 89].

The underlying model of the quantum chemistry calculations regards the Cs_2 molecule as a system of four particles. The four particles are the two valence electrons and two polarizable Cs^+ anions. In this way, an effect of other electrons than the valence electrons is also included. To improve the accuracy of the calculations, the results were fitted to experimental data whenever possible.

The electronic potentials of the eight $\text{Cs}_2(6s + 6p)$ states are not given by analytical expressions anymore. We use numerical values for discrete values of R that are interpolated with the program *Mathematica 7* to obtain smooth, continuous curves. After setting up the potentials in the different regions (1, 2 and 3) we connect them in order to form one continuous potential from small to large atomic separations. The potentials gained in case 1 and 2 match perfectly. But due to the different methods applied, the quantum chemistry calculations do not match exactly the analytical potentials of the long range region. Therefore, we interpolate the potentials and obtain the continuous potentials from small up to large values of R in the end.

3.1.3 Diagonalization of the Complete Hamiltonian H_e

In sections 3.1.2 and 3.1.1 we have seen how to set up the individual parts H_0, H_{so} and H_{hf} of H_e . To diagonalize H_e , it is necessary to find the relation between the basis in which H_0 is diagonal and the one in which H_{so} and H_{hf} are diagonal. As already stated, H_{so} and H_{hf} are diagonal in the asymptotic molecular basis set, whereas H_0 is diagonal in a Hund's case a basis set. The transformation between the two sets is obtained by re-coupling the basis vectors as shown in section 2.1.3. We find that:

$$\begin{aligned}
 |((s_1 l_1) j_1 i_A) f_1, ((s_2 l_2) j_2 i_B) f_2) f_t m_f)_\epsilon = & \sum_{\substack{j_t, i_t, s_t, l_t, m_{j_t}, m_{i_t} \\ m_{s_t}, m_{l_t}, m_{l_1}, m_{l_2}}} \hat{f}_1 \hat{f}_2 \hat{j}_1 \hat{j}_2 \hat{j}_t \hat{i}_t \hat{s}_t \hat{l}_t \begin{Bmatrix} s_1 & l_1 & j_1 \\ s_2 & l_2 & j_2 \\ s_t & l_t & j_t \end{Bmatrix} \begin{Bmatrix} j_1 & i_1 & f_1 \\ j_2 & i_2 & f_2 \\ j_t & i_t & f_t \end{Bmatrix} \\
 \langle j_t m_{j_t} i_t m_{i_t} | f_t m_f \rangle \langle s_t m_{s_t} l_t m_{l_t} | j_t m_{j_t} \rangle \langle l_1 m_{l_1} l_2 m_{l_2} | l_t m_{l_t} \rangle | S_t M_S \rangle^{1,2} | I_t M_I \rangle_{A,B} \\
 \frac{1}{2} (|l_2 m_{l_2}\rangle_A^1 |l_1 m_{l_1}\rangle_B^2 + (-1)^{S_t} |l_2 m_{l_2}\rangle_A^2 |l_1 m_{l_1}\rangle_B^1 - \epsilon (-1)^{2I+I_t} |l_2 m_{l_2}\rangle_B^1 |l_1 m_{l_1}\rangle_A^2 \\
 - \epsilon (-1)^{S_t+2I+I_t} |l_2 m_{l_2}\rangle_B^2 |l_1 m_{l_1}\rangle_A^1), \tag{3.18}
 \end{aligned}$$

or using a Hund's case a notation:

$$\begin{aligned}
|((s_1 l_1) j_1 i_A) f_1, ((s_2 l_2) j_2 i_2) f_2 \rangle_{f_t m_f} \epsilon = & \sum_{\substack{j_t, i_t, s_t, l_t, m_{j_t}, m_{i_t} \\ m_{s_t}, m_{l_t}, m_{l_1}, m_{l_2}}} \hat{f}_1 \hat{f}_2 \hat{j}_1 \hat{j}_2 \hat{i}_t \hat{s}_t \hat{l}_t \begin{Bmatrix} s_1 & l_1 & j_1 \\ s_2 & l_2 & j_2 \\ s_t & l_t & j_t \end{Bmatrix} \begin{Bmatrix} j_1 & i_1 & f_1 \\ j_2 & i_2 & f_2 \\ j_t & i_t & f_t \end{Bmatrix} \\
\langle j_t m_{j_t} i_t m_{i_t} | f_t m_f \rangle \langle s_t m_{s_t} l_t m_{l_t} | j_t m_{j_t} \rangle \langle l_1 m_{l_1} l_2 m_{l_2} | l_t m_{l_t} \rangle & \left|^{2S+1} \Lambda_{g/u}^{(+/-)} \right\rangle |I_t M_I \rangle_{A,B}
\end{aligned} \tag{3.19}$$

Using this relation, we can calculate the matrix elements of H_e in the asymptotic basis for different values of R :

$$H_e^{(i', i)} = \langle [((s_1 l_1) j_1 i_1) f'_1, ((s_2 l_2) j'_2 i_2) f'_2] f' m'_f, \epsilon' | \hat{H}_e | [((s_1 l_1) j_1 i_1) f_1, ((s_2 l_2) j_2 i_2) f_2] f m_f, \epsilon \rangle. \tag{3.20}$$

3.2 Calculation of the Hyperfine Splitted Adiabatic Potentials

The procedures described above yield a (854 x 854)-matrix for H_e . We can make use of the fact that m_f and ϵ remain good quantum numbers and thus, for the two values of ϵ (which are +1 and -1) and every value of $|m_f|$ we get a block matrix. The dimension dim of the matrices depends on the value of $|m_f|$. For $m_f = 9, 8, 7, 6, 5, 4, 3, 2, 1, 0$, we get $dim = 1, 5, 13, 24, 36, 48, 60, 72, 82, 86$ respectively. Hence, instead of calculating eigenvalues for the whole 854x854 matrix we calculate eigenvalues of the block matrices. The use of the good quantum numbers reduces the complexity of the calculations and helps to keep an overview. The calculations of eigenvalues of the various block-matrices as well as the set up of the Hamiltonian were done using the computational software program *Mathematica 7*.

By calculation of the eigenvalues, in the end we gain 854 hyperfine potentials. Every combination of m_f , ϵ corresponds to a number of hyperfine potentials that is the same as the dimension dim of the block matrices. These hyperfine potentials are further discussed in the next Chapter - the Chapter *Results and Discussion*.

4 Results and Discussion

The results of our calculations on the hyperfine structure of the $\text{Cs}_2(6s + 6p)$ states are presented and discussed in this Chapter. We have separated them into three parts. Firstly, we discuss and present the electronic potentials when hyperfine interactions are not considered. Secondly, we explain the general behavior of the hyperfine structure and discuss the results of our calculation for the long-range and for the short-range regions. Thirdly, we focus on the findings of interest for the ground-state transfer experiment. These findings concern the hyperfine structure of the $0_u^+(^2P_{1/2})$ and the $0_u^+(^2P_{3/2})$ adiabatic potentials.

4.1 Calculations without Hyperfine Interactions

In this first section of the Chapter *Results and Discussion*, we show the potentials that are obtained when the hyperfine interactions are not included. We show first the potentials that are obtained from the multipole expansion at large internuclear distance. Secondly, we include the asymptotic exchange interaction. Thirdly, we show plots of the electronic potentials that are taken from quantum chemistry calculations. In the last part we include spin-orbit interaction and show plots of the adiabatic potentials for the long-range region and for the short-range region.

Potentials obtained from multipole expansion of the atomic charge distributions

In figure 4.1, we show the four degenerate potentials that are gained from the multipole expansion at large internuclear distance. The method that is used to calculate the potentials is explained in the first part of section 2.3.3. The zero point is set to the $\text{Cs}_2(6s + 6p)$ dissociation limit. The potentials determine the electronic potentials for large atomic separations of $R > 40a_0$.

Potentials that include the asymptotic exchange interactions and the multipole expansion of the atomic charge distributions

Between internuclear separations of $20a_0$ and $40a_0$ we include an analytical expression of the asymptotic exchange interaction into the description of the electronic potentials. In this way we take into account the indistinguishability of the valence electrons and their fermionic character. In figure 4.2 we show how the electrostatic potentials split up under the influence of the asymptotic exchange interaction. The mathematical structure of the asymptotic exchange interaction is given in section 2.3.3. The derivation of the asymptotic exchange interaction is given in Ref. [84].

The dashed lines in figure 4.2 show the unsplit potentials obtained by multipole expansion only. The exchange interaction partly lifts the degeneracy of the potentials

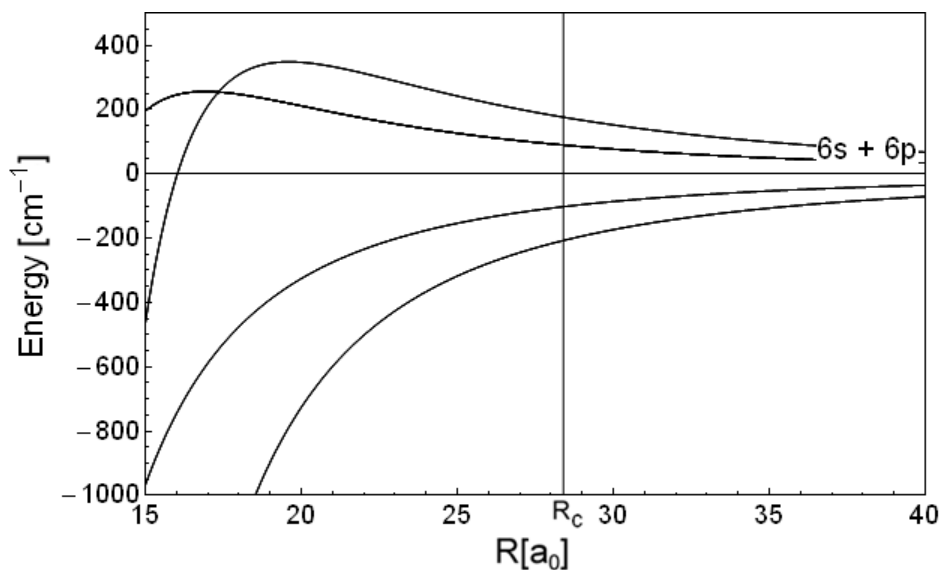


Figure 4.1: **Potentials obtained by multipole expansion only.** The vertical line indicates the LeRoy-radius R_c

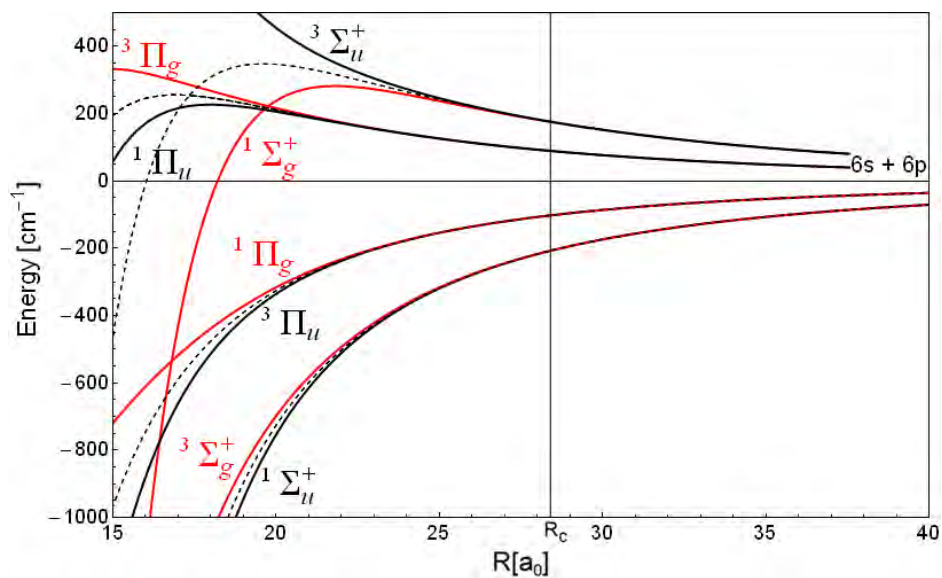


Figure 4.2: **Hund's case a potentials around the LeRoy-radius.** The figure shows the potentials obtained by the multipole expansion only (dashed lines) and the potentials obtained from a combination of asymptotic exchange interaction and multipole expansion (continuous lines). Due to the asymptotic exchange interactions, the potentials split up as R is becoming smaller. g symmetry states are colored in red and u symmetry states are colored in black. R_c is indicated by the vertical line.

gained by the multipole expansion. Every multipole potential splits up in two potentials that are described by the same value of $\beta = (-1)p\sigma$ but have a different combination of p and σ . ($p = +1$ for g states and $p = -1$ for u states. $\sigma = +1$ for singlet states and $\sigma = -1$ for triplet states.) The g symmetry potentials are colored in red and u symmetry potentials are colored in black. Again, zero energy is set to the $6s + 6p$ dissociation limit. Moreover, the molecular term symbols in a Hund's case a notation are included to label the potentials.

Potentials in the short-range region (taken from quantum chemistry calculations)

In the short range region, below $20a_0$, we use numerical data from quantum chemistry calculations. In principle, the used quantum chemistry calculations would provide us with data until internuclear separations of $40a_0$, but the potentials do not coincide exactly with the potentials used to model the interaction of the atoms around the Leroy-radius. Therefore, we cut the potentials from the quantum chemistry calculations and the analytical potentials (multipole expansion + asymptotic exchange interaction) around approximately $20a_0$ and interpolate the potentials that should coincide. In this way, we obtain smooth, continuous curves from small up to large internuclear separations. The result is displayed in figure 4.3.

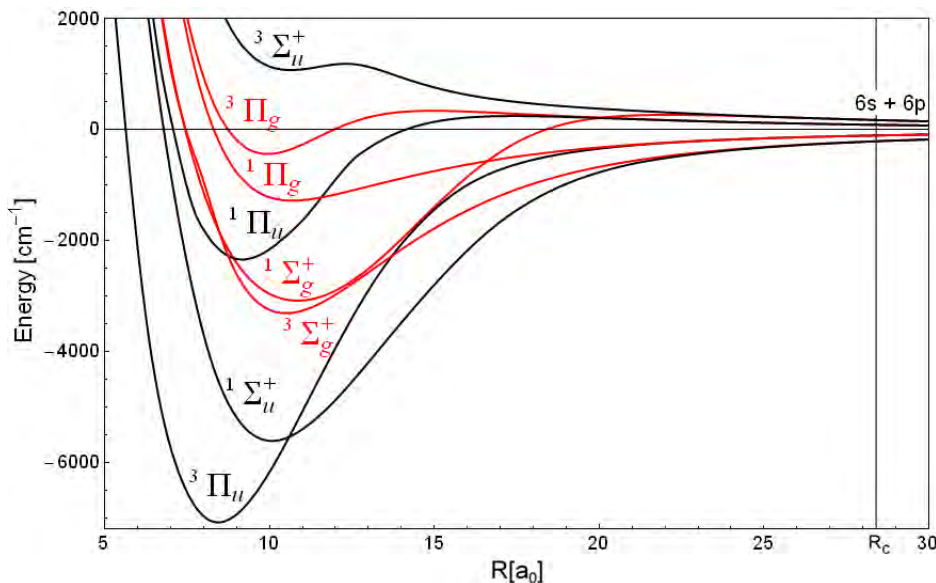


Figure 4.3: **Plot of the diabatic potentials in the short-range region.** The plotted Hund's case a potentials are gained by combining potentials taken from quantum chemistry calculations and potentials obtained by adding multipole expansion and asymptotic exchange interaction as explained in Chapter 3. The vertical line indicates R_c .

We have labeled the potentials of figure 4.3 with the molecular term symbol in Hund's case a notation. g states are colored in red and u states in black. The connected curves enable us to model the diabatic potentials from about $5a_0$ up to an arbitrary large internuclear distance. Since we did not yet include spin-orbit interaction, every electronic potential is degenerate with respect to the orientation of the total electron spin projection and in the case of Π states with respect to the projection of the total orbital angular momentum of the electrons. (Of course every potential is also degenerated with respect to the orientation of the nuclear spin, but for now we neglect the nuclear spin.)

Hence, ${}^3\Pi$ potentials are 6 times degenerated. ${}^1\Pi$ potentials are 2 times degenerated, ${}^3\Sigma$ potentials are 3 times degenerated and ${}^1\Sigma$ are not degenerated, resulting in 12 states for g and for u symmetry. Thus, the overall number of states is 24.

Adiabatic potentials (potentials that include spin-orbit interaction)

When we include spin-orbit interaction, the degeneracy of the eight diabatic potentials is partly lifted. Spin-orbit interactions split up the diabatic potentials with respect to the absolute value of the total electronic angular momentum projection Ω . ${}^3\Sigma$ potentials are split into a ${}^3\Sigma_0$ and a ${}^3\Sigma_1$ potential. ${}^3\Pi$ potentials are split into potentials that can be described by ${}^3\Pi_0$, ${}^3\Pi_1$ and ${}^3\Pi_2$. In addition, ${}^3\Pi_0$ potentials are split into the ${}^3\Pi_0(+, -)$ and the ${}^3\Pi_0(-, +)$ potential. Thus, we obtain 16 adiabatic potentials as a result of the splitting due to spin-orbit interaction. The adiabatic potentials are plotted for the short range region in figure 4.4.

Figure 4.4 shows all adiabatic potentials from $5a_0$ up to $30a_0$. The considerably strong spin-orbit interaction of Cs_2 not only results in a splitting of the potentials, but also in deformations of the diabatic potentials. The most obvious example is the disappearance of the crossing between the $A^1\Sigma_u^+$ potential and the $b^3\Pi_u$ potential. In the presence of such strong spin-orbit interaction, it is convenient to describe the adiabatic potentials with the use of Hund's case c notation. The plot for the adiabatic potentials in the long-range region is given in figure 4.5.

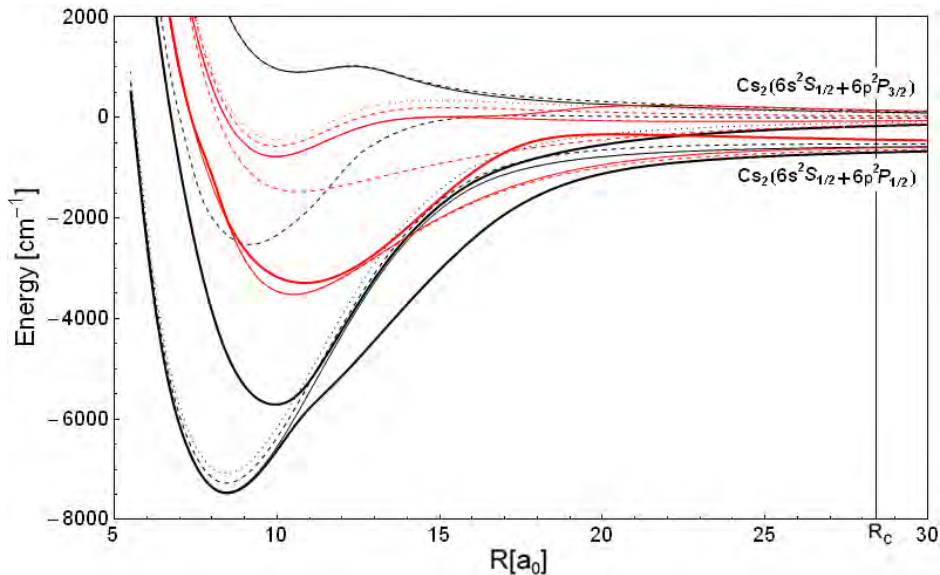


Figure 4.4: **Adiabatic potentials in the short-range region.** Internuclear separations vary from $5a_0$ up to $30a_0$. The energy zero-point is set to the $\text{Cs}_2(6S_{1/2} + 6P_{3/2})$ dissociation limit. The adiabatic potentials are described in Hund's case c notation. Dotted lines are states with $\Omega = 2$, dashed lines are states with $\Omega = 1$ and continuous lines indicate states with $\Omega = 0$. The reflection symmetry is indicated by thin lines for $\sigma = -1$ and thick lines for $\sigma = +1$. g/u symmetry is indicated by colors: red indicates g symmetry and black indicates u symmetry.

In the long-range region the influence of the spin-orbit interaction becomes dominant because the electrostatic interaction between the atoms is of the same magnitude as

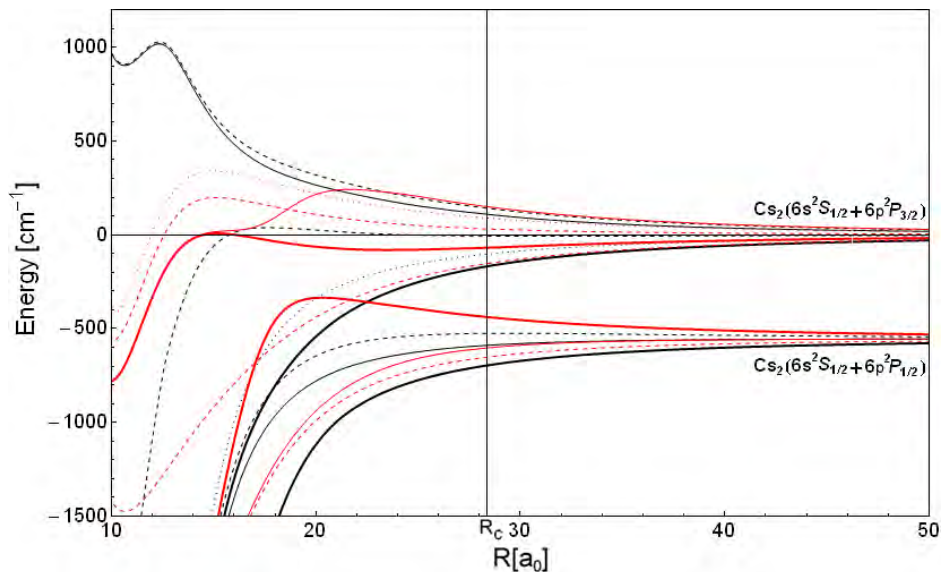


Figure 4.5: **Adiabatic potentials for internuclear separations that range from $10a_0$ to $50a_0$.** By comparison of this figure with figure 4.2 the strong influence of the spin-orbit interaction becomes visible. Spin-orbit splitting and avoided crossing can be seen very good. Like in figure 4.4, the energy zero-point is set to the $\text{Cs}_2(6S_{1/2} + 6P_{3/2})$ dissociation limit. The adiabatic potentials are described in Hund's case c notation. Dotted lines are states with $\Omega = 2$, dashed lines are states with $\Omega = 1$ and continuous lines indicate states with $\Omega = 0$. The reflection symmetry is indicated by thin lines for $\sigma = -1$ and thick lines for $\sigma = +1$. g/u symmetry is indicated by colors: red indicates g symmetry and black indicates u symmetry.

the spin-orbit interaction. Thus, figure 4.5 has no similarities with figure 4.2, which displays the diabatic potentials for approximately the same values of R .

Number of hyperfine potentials

The next step is to include hyperfine interactions into the calculations. As a consequence the degeneracy of the adiabatic potentials is further lifted. The nuclear spin of a cesium atom is $I = 7/2$. Thus, the total nuclear spin I_t , formed by coupling the two individual nuclear spins, can vary from 0 to 7. This results in 64 possible states $|I_t m_I\rangle$. I_t couples to the total electronic angular momentum J_t and forms the total molecular angular momentum F . However, hyperfine interactions are diagonal with respect to the absolute value of the projection of the total angular momentum $|m_f|$. States with the same $|m_f|$ have the same hyperfine potential. Taking this into account we can calculate the number of hyperfine potentials. As shown in the end of section 2.3.4, we have 24 molecular states if the nuclear spin is neglected. Thus, the total number of all states $24 \times 64 = 1536$. The hyperfine potentials are degenerate in $|m_f|$, therefore the number of potentials is the number of states with $|m_f| \geq 0$. Thus, $(1536 - 2 \times 86) / 2 + 2 \times 86 = 854$ is the number of potentials obtained by the hyperfine calculations. 2×86 is the number of states with $|m_f| = 0$ for $\epsilon = +1$ and $\epsilon = -1$.

For internuclear separations where $|m_L| = \Omega$ is a good quantum number, we can also calculate the number of hyperfine potentials that form the hyperfine structure of an adiabatic potential. For $\Omega = 0$, we get 64 possible states $|(m_L = \Omega = 0, I_t) F_t, m_F\rangle$.

Since states with $m_F \geq 0$ are degenerate, the hyperfine structure of $\Omega = 0$ potentials is formed by 36 hyperfine potentials. For $\Omega = 1$ and $\Omega = 2$, we have $m_L = \pm 1$ and $m_L = \pm 2$ respectively. Thus, for both values of Ω we get 128 states of $|(m_L, I_t)F_t, m_F\rangle$. Again we count the states that fulfill $m_F \geq 0$. This results in 71 hyperfine potentials for $\Omega = 1$ and 70 hyperfine potentials for $\Omega = 2$.

In the remaining part of this Chapter we investigate the 854 hyperfine potentials. In all steps it is rather helpful to keep in mind that ϵ and $|m_f|$ are always good quantum numbers. Therefore, we order the curves by these numbers. In section 4.2 we concentrate on the results describing hyperfine structure in the long range region. We show how the electronic potentials are correlated to the energy of two separated atoms and how the general structure changes with decreasing R . Important results are summarized in a table at the end of section 4.2. In section 4.3 we deal in detail with the results of the short range region.

4.2 Hyperfine Structure in the Long-Range Region

In this section we want to present and discuss the results of the hyperfine structure calculations for the long-range region. In the first part we show how the hyperfine potentials are connected to the dissociation limit of two separated cesium atoms. Then, we investigate the region of the potentials where the hyperfine interactions are of the same order of magnitude as the electrostatic interactions.

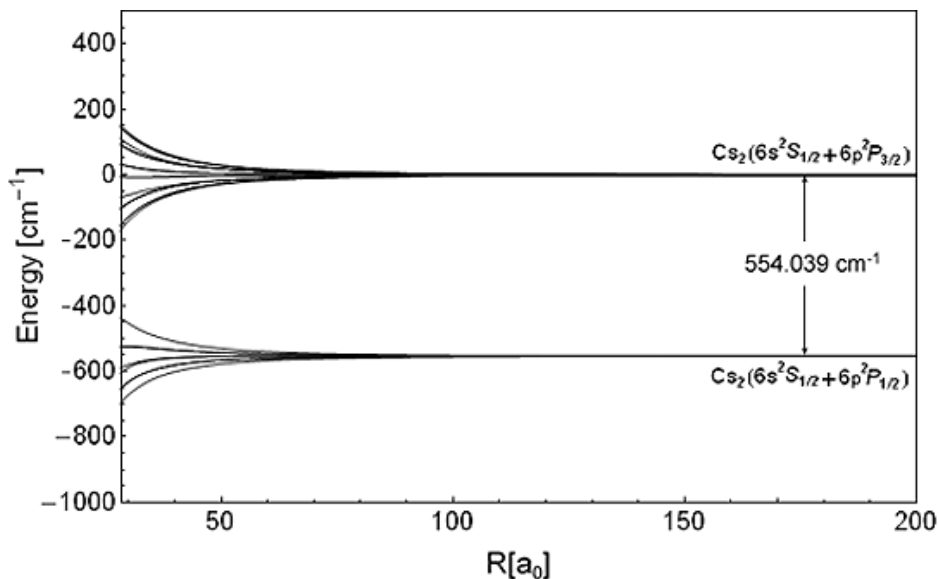


Figure 4.6: **All hyperfine potentials in the long-range region.** On this plot the $\text{Cs}_2(6^2S_{1/2} + 6^2P_{1/2})$ and the $\text{Cs}_2(6^2S_{1/2} + 6^2P_{3/2})$ dissociation limits are visible very well. To display the hyperfine structure we zoom in the following plots on the lower bunch and the upper bunch of lines.

We begin the discussion with a plot, figure 4.6, where all hyperfine potentials starting from $R = R_c$ up to $R = 200a_0$ are shown. The plot illustrates how the electrostatic interaction decrease and become smaller than the spin-orbit interaction as R increases. For large internuclear distances the potentials tend to one of the two spin-orbit split dissociation limits $\text{Cs}_2(6^2S_{1/2} + 6^2P_{1/2})$ and $\text{Cs}_2(6^2S_{1/2} + 6^2P_{3/2})$. The effects of

hyperfine interactions are much too small to be visible in this plot. The splitting due to hyperfine interactions lead to splittings that are below 10 GHz, which is very small compared to the spin-orbit splitting of $\Delta = 554 \text{ cm}^{-1} \approx 16000 \text{ GHz}$. Therefore, one has to zoom on the potentials in order to resolve the hyperfine structure.

The first zoom is made on the potentials connected to the $\text{Cs}_2(6^2S_{1/2} + 6^2P_{1/2})$ dissociation limit. The plot of the zoom is shown in figure 4.7.

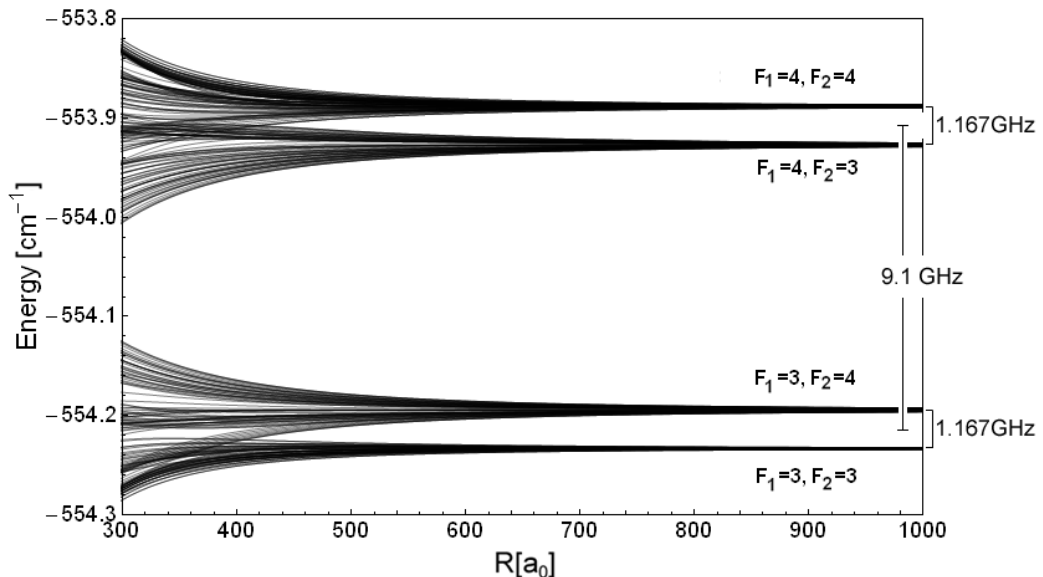


Figure 4.7: **Zoom on the potentials that dissociate to the $\text{Cs}_2(6s^2S_{1/2} + 6p^2P_{1/2})$ limit.** F_1 and F_2 indicate the quantum numbers of the two atom state to which the hyperfine potentials tend. F_1 (F_2) labels the quantum number of the s -state (p -state) atom.

The internuclear separations of the plot in figure 4.7 are between $R = 300a_0$ and $R = 1000a_0$. At these large internuclear distances the electrostatic interactions between the atoms are smaller than the molecular hyperfine structure splitting. Therefore, we can see the connection to the asymptotic limits of the two atom states, where every atom is in one of the possible atomic hyperfine states.

The lowest bunch of lines corresponds to the asymptotic limit of one atom in the $\text{Cs}(6s^2S_{1/2}, F_1 = 3)$ state and the other atom in a $\text{Cs}(6^2P_{1/2}, F_2 = 3)$ state. In the second lowest bunch of lines, the p -atom is in a $F_2 = 4$ hyperfine state. Therefore, the dissociation limit is heightened by 1.167 GHz, the splitting between the $\text{Cs}(6p^2P_{1/2}, F_2 = 3)$ and the $\text{Cs}(6p^2P_{1/2}, F_2 = 4)$ state.

When the hyperfine state of the s -atom changes from $F_1 = 3$ to $F_1 = 4$ we can observe the same scheme again. The lines lie now 9.192 GHz higher, which is the splitting between the $\text{Cs}(6s^2S_{1/2}, F_1 = 3)$ and the $\text{Cs}(6s^2S_{1/2}, F_1 = 4)$ states. Thus, the third lowest line is the dissociation limit where the s -atom is in the $\text{Cs}(6s^2S_{1/2}, F_1 = 4)$ state and the p -atom in the $\text{Cs}(6p^2P_{1/2})$ state. The highest bunch of lines is connected to the dissociation limit where the hyperfine state of the s -atom is $F_1 = 4$ and also the hyperfine state of the p -atom is $F_2 = 4$. In figure 4.7 we explicitly label these asymptotic limits with $(F_1 = 3, F_2 = 3)$, $(F_1 = 3, F_2 = 4)$, $(F_1 = 4, F_2 = 3)$ and $(F_1 = 4, F_2 = 4)$.

Analogous to figure 4.7, figure 4.8 shows a zoom on the energy range around the $\text{Cs}_2(6s^2S_{1/2} + 6p^2P_{3/2})$ asymptotic limit. The plot range is between $300a_0$ and $1000a_0$, the same as in the plot of figure 4.7. The spectrum of figure 4.8 is richer than the spectrum of figure 4.7 because $J_2 = 3/2$ for the hyperfine potentials of figure 4.8. F_2 can take the values 2, 3, 4 or 5. The splitting between the hyperfine levels of the p -atom is much smaller than the splitting between the hyperfine levels of the s -atom. The splitting between $\text{Cs}(6p^2P_{3/2}, F_2 = 2)$ and $\text{Cs}(6p^2P_{3/2}, F_2 = 3)$ is 0.15 GHz, between $\text{Cs}(6p^2P_{3/2}, F_2 = 3)$ and $\text{Cs}(6p^2P_{3/2}, F_2 = 4)$ is 0.201 GHz and between $\text{Cs}(6p^2P_{3/2}, F_2 = 4)$ and $\text{Cs}(6p^2P_{3/2}, F_2 = 5)$ 0.251 GHz. The hyperfine splitting of the s -atom is 9.1 GHz. As a consequence, the hyperfine splittings gather in two main bunches of lines, which correspond to the value of F_1 . These main bunches of lines are subdivided into four bunches of lines, which correspond to the possible values of F_2 . Figure 4.8 with its inset **a** illustrates the hyperfine splitting.

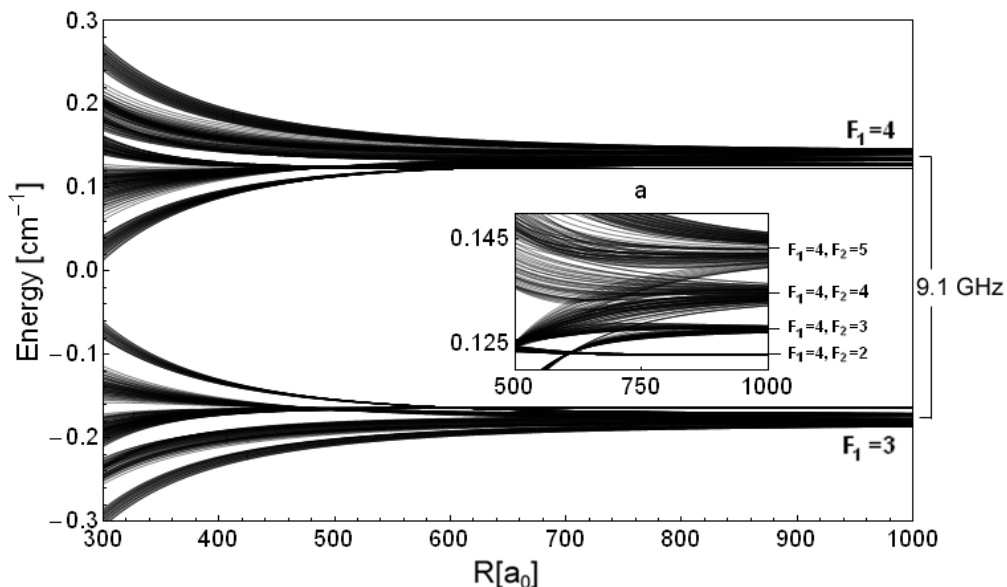


Figure 4.8: **Zoom on the potentials that dissociate to the $\text{Cs}_2(6s^2S_{1/2} + 6p^2P_{3/2})$ limit.** F_1 and F_2 indicate the quantum numbers of the two atom state to which the hyperfine potentials tend. F_1 (F_2) labels the quantum number of the s -state (p -state) atom. Inset **a** shows a zoom on the lines connected to the $F_1 = 4, F_2 = 2, 3, 4, 5$.

In figure 4.7 and figure 4.8 we demonstrate that our calculations indeed provide the connection of the hyperfine potentials and the two-atom dissociation limits. In the remaining part of this section, using of figure 4.7, figure 4.9 and figure 4.10, we illustrate the behavior of the hyperfine potentials as R is becoming smaller.

On the left side of figure 4.7, one sees how the hyperfine potentials split up when R is reduced. When R takes values where the electrostatic interactions between the two atoms is comparable to the hyperfine splitting, hyperfine potentials that are connected to different dissociation limits approach each other. The hyperfine potentials perturb each other and also undergo real and avoided crossings. Since the Hamiltonians of molecular interactions are not diagonal in the atomic basis set, F_1 and F_2 fail to be good quantum numbers when the off-diagonal elements are not negligible anymore. Only m_f and ϵ remain good quantum numbers. The classification according to F_2 fails

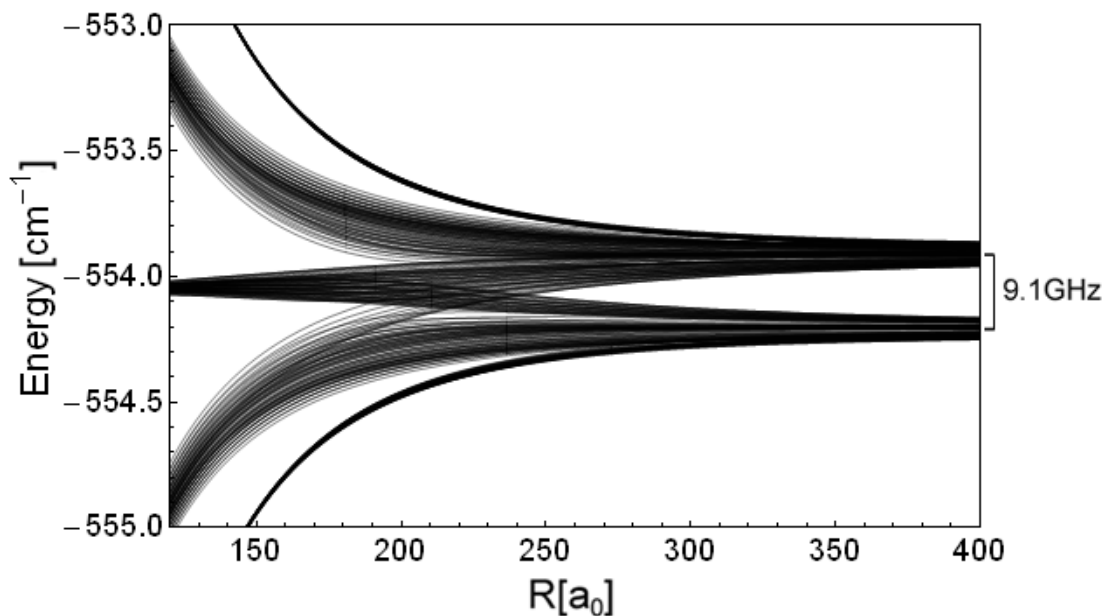


Figure 4.9: **Zoom on the potentials that dissociate to the $\text{Cs}_2(6s^2S_{1/2} + 6p^2P_{1/2})$ limit.** Internuclear separations reach from $R = 120a_0$ up to $R = 400a_0$.

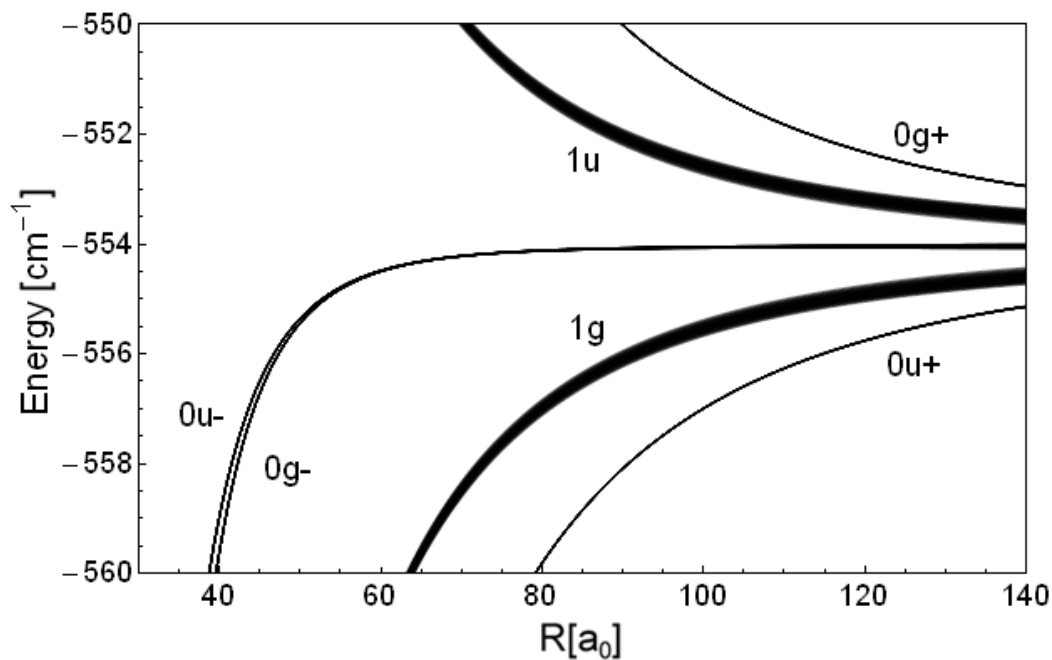


Figure 4.10: **Zoom on the potentials that dissociate to the $\text{Cs}_2(6s^2S_{1/2} + 6p^2P_{1/2})$ limit.** Internuclear separations reach from $R = 30a_0$ up to $R = 140a_0$. The labels of the adiabatic potentials are also included.

F_1	F_2	$R_f [a_0]$
<hr/>		
$j_2 = 1/2$		
3	3	410
	4	
4	3	420
	4	
<hr/>		
$j_2 = 3/2$		
3	5	855
	4	
	4	750
	3	
	3	620
	2	
4	2	620
	3	
	3	820
	4	
	4	950
	5	
<hr/>		

Table 4.1: **Internuclear separation at which F_1 and F_2 cease to be good quantum numbers.** Internuclear separation at which the hyperfine potentials emerging from particular hyperfine dissociation limits cross the first time potentials emerging from another dissociation limit. The first two columns show the quantum numbers of the dissociation limit and the third shows R_f the internuclear separation at which the potentials cross.

first because the hyperfine splitting of p -states is smaller than the splitting of the s -states. This happens at about $400a_0$, visible in figure 4.7. For R smaller than $300a_0$ also potentials associated to $F_1 = 3$ and $F_1 = 4$ approach each other, as seen in figure 4.9.

In table 4.1 we tabulated at about which internuclear separation a specific set of F_1 and F_2 values ceases to contain good quantum numbers, since the potentials emerging from a particular dissociation limit cross the potentials of another dissociation limit.

If one decreases the internuclear distance below approximately $140a_0$, the Coulomb interactions between the atoms become larger than the hyperfine splitting, see figure 4.10. Then, according to the good quantum numbers, the hyperfine potentials gather and form the hyperfine structure of the adiabatic potentials. This happens for the 0_u^+ potential at $290a_0$, for the 1_g potential at $185a_0$, for the 0_g^- potential at $66a_0$, for the 0_u^- potential at $66a_0$, for the 1_u potential at $210a_0$ and for the 0_g^+ potential at $285a_0$.

fine structure state	R_s [a_0]	maximum hyperfine splitting [GHz] at $R = R_c$
0_g^+	140	0.717
1_u	140	6.752
0_u^-	68	0.019
2_g	68	8.568
1_g	190	4.757
1_u	190	5.584
0_g^-	69	0.008
2_u	69	8.573
1_u	165	5.659
0_u^+	225	0.036
0_g^+	285	0.002
1_u	210	8.606
0_u^-	66	0.017
0_g^-	66	0.017
1_g	185	8.860
0_u^+	290	0.006

Table 4.2: **Formation of the hyperfine structure of the adiabatic potentials for decreasing R .** The first column shows the term symbol of the adiabatic potential. The second column shows at which internuclear separation R_s the hyperfine structure potentials of a particular adiabatic potential and the hyperfine structure potentials of another adiabatic potential cross, so that one can not relate a hyperfine potential to the hyperfine structure of a single adiabatic potential anymore. For $R < R_s$, the hyperfine potentials can be related to an adiabatic potential. The third column gives the maximum hyperfine splitting of the various adiabatic potentials at the Leroy-radius R_c .

The same procedure can also be applied to the hyperfine potentials that emerge from the $\text{Cs}_2(6s^2S_{1/2} + 6p^2P_{3/2})$ dissociation limit. In table 4.2, we tabulated the internuclear separations R_s at which the hyperfine structure of all the adiabatic potentials are formed for both cases, the $\text{Cs}_2(6s^2S_{1/2} + 6p^2P_{1/2})$ and the $\text{Cs}_2(6s^2S_{1/2} + 6p^2P_{3/2})$ dissociation limits. Moreover, we added the maximum hyperfine splitting at the Leroy-radius R_c to give a connection to the short-range region.

4.3 Hyperfine Structure in the Short-Range Region

In section 4.2 we have discussed the hyperfine splitting of the molecular states for internuclear separations larger than the Leroy radius $R_c = 28.4a_0$. We have seen how the electronic potentials are connected to the atomic energies, and how the quantum numbers describing the atomic states fail to be conserved as a consequence of the increasing electrostatic interactions between the atoms.

In this section we deal with the short-range region. The short-range region is of higher interest for the ground-state transfer experiments in Innsbruck because the vibrational levels of the $(A-b)0_u^+$ system that are exploited in the STIRAP have right-hand Condon points R_1 and R_2 , where $R_1 = 11.9a_0$ for the $\nu = 61$ level and $R_2 = 15.58a_0$ for the $\nu = 225$ level. Both values are well below $R_c = 28.4a_0$. Figure 4.11 shows a plot of the

adiabatic potentials in the shortrange region. The $0_u^+(^2P_{1/2})$ potential is colored in red and the $0_u^+(^2P_{3/2})$ potential is colored in blue. R_1 , R_2 and the two vibrational levels are also indicated.

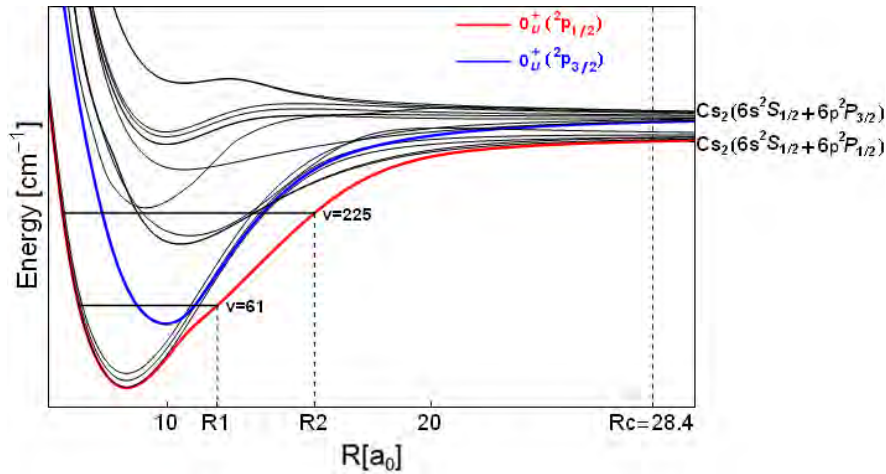


Figure 4.11: **Adiabatic potentials in the short range region.** The red line indicates the $0_u^+(^2P_{1/2})$ potential and the blue line indicates the $0_u^+(^2P_{3/2})$ potential. The vibrational states $\nu = 225$ and $\nu = 61$ of the coupled potentials are exploited in STIRAP of the ground-state transfer experiment in Innsbruck. The right-hand Condon points of the two vibrational states are also labeled. $R_1 = 11.9a_0$ is the Condon point for the $\nu = 61$ level and $R_2 = 15.58a_0$ for the $\nu = 225$ level. The zero point of energy is set to the $\text{Cs}_2(6s^2S_{1/2} + 6p^2P_{3/2})$ dissociation limit.

In the first part of this section, we discuss the characteristics of our results by looking at a specific value of R ($R = 12a_0$). We use the arguments given in section 2.6.3 to explain the characteristics of the hyperfine structure. Then, in section 4.3.2, we focus on the potential that are of interest for the ground-state transfer experiment in Innsbruck. We discuss the characteristics of the $(A-b)0_u^+$ system, give the maximum hyperfine splitting of the $0_u^+(^2P_{1/2})$ and the $0_u^+(^2P_{3/2})$ potentials and estimate the hyperfine splitting of two used vibrational levels. Finally, we illustrate the maximum hyperfine structure splitting of all the other adiabatic potentials.

4.3.1 Investigation of the Hyperfine Structure at $R = 12a_0$

In this section, we investigate the hyperfine structure at $R = 12a_0$ to show exemplarily how the general characteristics of our results can be interpreted. Figure 4.12 shows plots of the hyperfine structure at $R = 12a_0$. In the plot, the energy of a hyperfine potential that belongs to the hyperfine structure of a specific adiabatic potential is given relative to the specific adiabatic potential at $R = 12a_0$. In figure 4.13 we show a zoom on those hyperfine structures that cannot be resolved in figure 4.12.

In the plot, one sees the hyperfine splitting of the 16 different adiabatic potentials. They are ordered from left to right, decreasing in energy of the adiabatic potentials. The hyperfine splittings are labeled in two ways: The first row tells to which adiabatic potential the hyperfine splitting belongs. For example, the splitting on the far right is the hyperfine structure of the $0_u^+(^2P_{1/2})$ potential. The second row tells which Hund's case a state has the highest contribution in the wave function of the coupled Hund's case c state. For instance, a 1_g state is formed by couplings between $^1\Pi_g$, $^3\Pi_g$ and $^3\Sigma_g^+$.

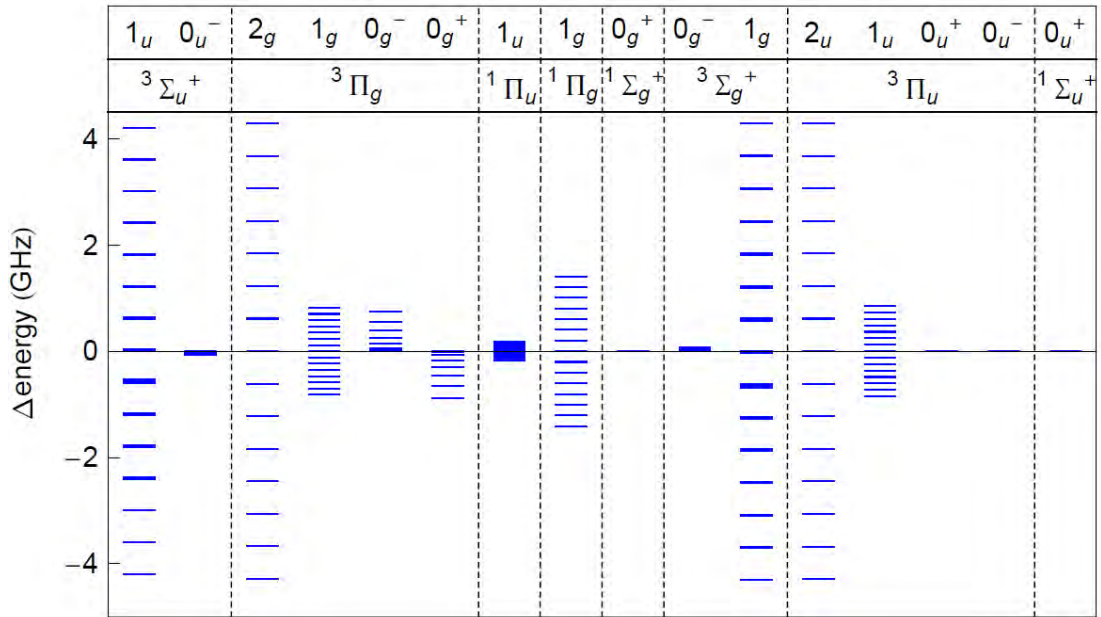


Figure 4.12: **Hyperfine structure of all adiabatic potentials at $R = 12a_0$.** The first column labels the different hyperfine structure with the corresponding term symbol in Hund's case c notation. The second row labels the various hyperfine structures with the uncoupled potentials that are mostly responsible for the plotted hyperfine structure. The blue lines represent energy of a hyperfine potential that belongs to a specific adiabatic potential relative to the specific adiabatic potential at $R = 12a_0$.

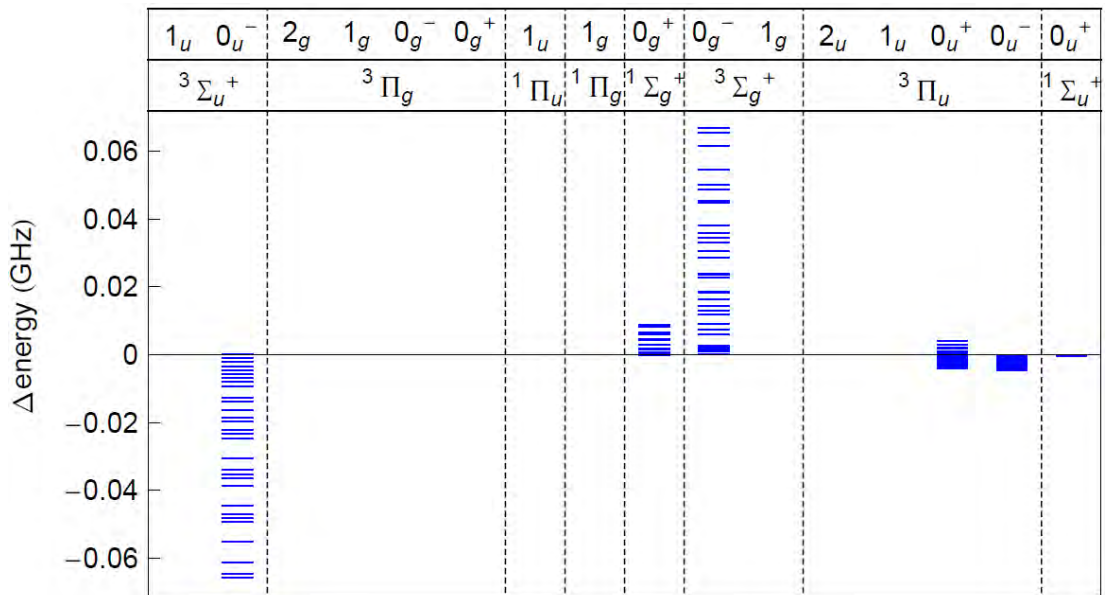


Figure 4.13: **Zoom on figure 4.12.** Displayed are the hyperfine structures of adiabatic potentials with a maximum hyperfine splitting at $R = 12a_0$ smaller than 100 MHz.

If the second row is labeled with ${}^3\Pi_g$, it means that the wave function of the 1_g state has the highest contributions from the ${}^3\Pi_g$ state.

In section 2.6.3 at the end of the Chapter *Theory*, we discussed the hyperfine interactions in terms of perturbation theory. We use the arguments made in this section to discuss figure 4.12 and figure 4.13. Therefore, we recall those arguments shortly:

The magnetic dipole interactions between electrons and nuclei, especially the Fermi contact interaction, are responsible for the largest splittings in the hyperfine structure. For $\Omega = 1$ or 2 , contributions of the magnetic dipole interactions of first order perturbation do not vanish. Moreover, the first order energy corrections are proportional to m_I , thus we expect a splitting that is proportional to m_I if $\Omega \neq 0$.

For $\Omega = 0$ the first order of the magnetic dipole interaction vanishes. Second order energy corrections have to be calculated. Their splitting is in general small compared to the splitting of states with $\Omega = 1$ or 2 . In second order perturbation only states that lie energetically close can act as significant perturbers. The energy difference between considered and perturbing state determines the sign. If the perturbing state $|\bar{n}\rangle$ has $\bar{\Omega} = 0$, the energy corrections is proportional to m_I^2 .

Behavior of $\Omega \neq 0$ states at $R = 12a_0$

If we look at figure 4.12, we see that the states with $\Omega = 1$ or 2 has a large hyperfine splitting. It lies between 1 GHz and 9 GHz. Generally, the hyperfine splitting of states with $\Omega = 0$ is smaller. It lies between 1 GHz and only fractions of a MHz. This is in agreement with the arguments given before. States with $\Omega = 0$ have no first order contribution of the magnetic dipole interactions and have thus a smaller hyperfine splitting.

There are also large differences in the magnitude of the splittings. Some states with $\Omega = 1$ have a hyperfine structure as large as those of $\Omega = 2$, whereas others with $\Omega = 1$ have a much smaller hyperfine structure. To explain this behavior we use the second row of the plots. As already stated, they tell which uncoupled states are most important for the composition of the wave function of the Hund's case *c* states.

The states with the largest hyperfine structure (maximum splitting of almost 9 GHz) are those in the first, the third, the eleventh and the twelfth column of figure 4.12. The second row connects these states to the ${}^3\Sigma_u^+$, the ${}^3\Pi_g$, the ${}^3\Sigma_g^+$ and the ${}^3\Pi_u$ states. So the largest hyperfine structure is produced by $\Omega \neq 0$ states that are predominantly of triplet character with $\Sigma = \pm 1$.

States associated by the second row with $\Sigma = 0$ have a smaller hyperfine structure splitting. The largest hyperfine structure of states with $\Sigma = 0$ has 1_g . This state is formed mainly by ${}^1\Pi_g$. Its maximum hyperfine splitting is about 3 GHz.

The hyperfine structure for all the plotted states with $\Omega \neq 0$ is made up by fifteen packs. We know that the hyperfine splitting of $\Omega \neq 0$ should be proportional to m_I . The maximum value of I_t is 7. Thus, there are $2 \times 7 + 1 = 15$ possibilities for m_I at the most. The fifteen packs correspond to the fifteen possible values of m_I and the equal splitting reflects the proportionality of the magnitude of first order energy corrections to m_I .

	Hund's case c state	Hund's case a state	$E(12a_0)$ [cm $^{-1}$]	max. splitting [GHz]
1.	1_u	${}^3\Sigma_{u,1}^+$	1016	8.407
2.	0_u^-	${}^3\Sigma_{u,0}^+$	1007	0.068
3.	2_g	${}^3\Pi_{g,2}$	15	8.570
4.	1_g	${}^3\Pi_{g,1}$	-133	1.659
5.	0_g^-	${}^3\Pi_{g,0}$	-329.2	0.692
6.	0_g^+	${}^3\Pi_{g,0}$	-329.9	0.691
7.	1_u	${}^1\Pi_{u,1}$	-1087	0.332
8.	1_g	${}^1\Pi_{g,1}$	-1354	2.837
9.	0_g^+	${}^1\Sigma_{g,0}^+$	-3109	0.008
10.	0_g^-	${}^3\Sigma_{g,1}^+$	-3182	0.070
11.	1_g	${}^3\Sigma_{g,0}^+$	-3190	8.600
12.	2_u	${}^3\Pi_{u,2}$	-3935	8.571
13.	1_u	${}^3\Pi_{u,1}$	-4138	1.684
14.	0_u^+	${}^3\Pi_{u,0}$	-4222	0.008
15.	0_u^-	${}^3\Pi_{u,0}$	-4317	0.004
16.	0_u^+	${}^3\Sigma_{g,0}^+$	-5139	0.0002

Table 4.3: **Data to interpret the hyperfine structure of the adiabatic potentials at $R = 12a_0$.** The third column tells which Hund's case a state has the highest contribution in the wave function of the coupled Hund's case c state of column two. $E(12a_0)$ tells the energy of the adiabatic potential at $R = 12a_0$ relative to the $\text{Cs}_2(6s^2S_{1/2} + 6p^2P_{3/2})$ dissociation limit. The maximum splitting (max. splitting) of the hyperfine structure of an adiabatic potential is given in column number 5.

Behavior of $\Omega = 0$ states at $R = 12a_0$

In second order perturbation theory, the energy difference between a particular state and its perturbers determines both the magnitude of the energy correction and the sign of the energy shift due to perturbations. Therefore, in table 4.3 we give the energy at $R = 12a_0$ of the adiabatic potentials relative to the $\text{Cs}_2(6s^2S_{1/2} + 6p^2P_{3/2})$ dissociation limit and values for the maximum splitting of the hyperfine structure of an adiabatic potential. Looking at the table, we can identify the possible perturbers of a state.

The second row of table 4.3 and the second column from the left of figure 4.12 and figure 4.13 describe the hyperfine splitting of the first adiabatic potential that we consider, the 0_u^- potential. Its wave function is predominantly of ${}^3\Sigma_{u,0}^+$ character. The energy relative to the $\text{Cs}_2(6s^2S_{1/2} + 6p^2P_{3/2})$ dissociation limit of the 0_u^- states is 1007 cm^{-1} . The energetically next Hund's case c potential would be the 1_u potential with an energy relative to the $\text{Cs}_2(6s^2S_{1/2} + 6p^2P_{3/2})$ dissociation limit of 1016 cm^{-1} . The second closest Hund's case c potential would be the third of table 4.3, the 2_g potential, with an energy relative to the $\text{Cs}_2(6s^2S_{1/2} + 6p^2P_{3/2})$ dissociation limit of 15 cm^{-1} , energetically much more separated from 0_u^- than 1_u . Hence, we consider only the 1_u states as a significant perturber of 0_u^- . The 1_u states have $\Omega = 1$, thus we cannot make statements about the proportionality of the energy splitting with respect to the m_J . However, since the energy difference $\Delta E = E - \bar{E}$, the difference between the energy of the considered state and the perturber is negative, the hyperfine potentials of the 0_u^- potential is shifted negatively relative to the unsplitted 0_u^- potential.

The next hyperfine structure of a state with $\Omega = 0$ is the hyperfine structure of 0_g^- . It is

displayed in column 5 of figure 4.12 and data are given in the fifth row of table 4.3. The perturbers are the 0_g^+ states, which lie very close. The separation is only 0.7 cm^{-1} . Due to the small separation, second order effects are quite large. The maximum hyperfine splitting is 0.692 GHz , which is even larger than the maximum hyperfine splitting of the 1_u adiabatic potential. The 0_g^+ states have $\Omega = 0$. Thus, the splitting is proportional to m_I^2 . Additionally, the hyperfine potentials are shifted relative to 0_g^- potential by positive values (ΔE is positive).

0_g^+ states (number 6 in table 4.3 and figure 4.12) display a similar behavior as the 0_g^- , but the hyperfine potentials are shifted, relative to the unsplitted 0_g^+ adiabatic potential, in a negative sense.

The ninth states of table 4.3 and figure 4.12, 0_g^+ lie close to the states number 10 (0_g^-) and the states of number 11 (1_g^-). Both lie energetically lower and thus the relative splitting is positive. 0_g^- states have $\Omega = 0$ and 1_g^- states have $\Omega = 1$. The splitting of 0_g^+ (shown in figure 4.13) displays a splitting that is proportional to m_I^2 . Therefore, we can conclude that the effects of 1_g^- states play a much smaller role than the effects of the 0_g^+ states.

The tenth row of table 4.3 shows the data of 0_g^- states. The perturbers are the 1_g^- states. The energy correction is positive.

The adiabatic 0_u^+ potential of row number 14 has an energy relative to the $\text{Cs}_2(6s^2S_{1/2} + 6p^2P_{3/2})$ dissociation limit of -4222 cm^{-1} . Interestingly, there are two perturbers above the 1_u states at -4138 cm^{-1} and below the 0_u^+ states at -4317 cm^{-1} . Thus, we have positive and negative energy shifts in the hyperfine structure of 0_u^+ . The shifts with a positive sign show a splitting proportional to m_I .

The second lowest state in energy is 0_u^- . The perturbers are the above lying 0_u^+ states. Hence, the splitting is proportional to m_I^2 and the energy shift is negative.

The last row, number 16, corresponds to 0_u^+ states whose wave function has mainly $^1\Sigma_u^+$ character. The perturbers are the 0_u^- states. Thus, we observe energy corrections with a negative sense and a splitting proportional to m_I^2 .

4.3.2 Focus on $(A - b)0_u^+$ System

In this section we throw a closer look at the hyperfine structure of states that form the $(A - b)0_u^+$ system. Vibrational levels of these states are exploited in the ground-state transfer experiment. Therefore they are particularly interesting. The potentials of these states are plotted in red and blue in figure 4.11. Firstly, we look closer on the $0_u^+(^2P_{1/2})$ potential because it has a simpler hyperfine structure. This is followed by a discussion of the $0_u^+(^2P_{3/2})$ potentials.

Hyperfine structure of the $0_u^+(^2P_{1/2})$ potential

The $0_u^+(^2P_{1/2})$ adiabatic potential is plotted in red in figure 4.11 relative to the $\text{Cs}_2(6s^2S_{1/2} + 6p^2P_{3/2})$ dissociation limit. In figure 4.14, we plotted the hyperfine potentials that belong to the hyperfine structure of the $0_u^+(^2P_{1/2})$ adiabatic potential relative to the $0_u^+(^2P_{1/2})$ adiabatic potential. In this way, we can illustrate the relative hyperfine splitting of the $0_u^+(^2P_{1/2})$ potential and we show how the hyperfine potentials are pushed

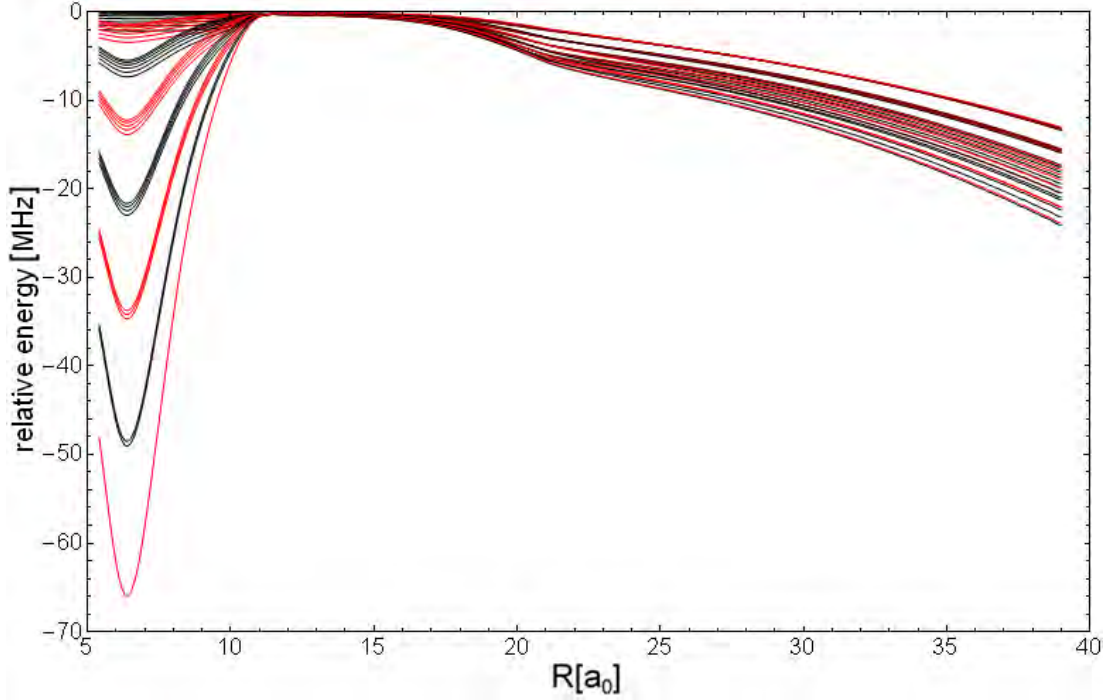


Figure 4.14: **Hyperfine potentials of the $0_u^+(^2P_{1/2})$ adiabatic potential relative to the $0_u^+(^2P_{1/2})$ adiabatic potential.** Hyperfine potentials that are characterized by an even (odd) value of $|m_f|$ are plotted in black (red).

away by hyperfine interactions from the adiabatic potential. The values of $|m_f|$ of the hyperfine potentials that belong to the $0_u^+(^2P_{1/2})$ potential vary from zero to seven. In figure 4.14 we plotted even values of $|m_f|$ in black and odd values in red. What is remarkable, in figure 4.14 is the drastic change of the magnitude of the hyperfine structure around the avoided crossing that is centered at $R_{crossing} = 10.6a_0$ at an energy of approximately -5500 cm^{-1} relative to the $\text{Cs}_2(6s^2S_{1/2} + 6p^2P_{3/2})$ dissociation limit. The value of the maximum hyperfine splitting changes from about 60 MHz to much less than 1 MHz within a few times of the Bohr radius. We explain this behavior with two effects. Firstly, one has to consider that the $0_u^+(^2P_{1/2})$ state is formed by spin-orbit coupling between the $A^1\Sigma_u^+$ state and the $b^3\Pi_u$ state. Due to the avoided crossing, the ratio of the A and the b state in the composition of the coupled state changes. For energies much smaller than -5500 cm^{-1} relative to the $\text{Cs}_2(6s^2S_{1/2} + 6p^2P_{3/2})$ dissociation limit, the $0_u^+(^2P_{1/2})$ state is almost entirely formed by the b state. Triplet states have a larger hyperfine splitting than singlet states. Since the contribution of the b state decreases during the avoided crossing, also the hyperfine splitting is reduced. The composition of the $0_u^+(^2P_{1/2})$ in A and b state can be illustrated by the energy dependency of the rotational constant B_ν .

One calculates B_ν by averaging the value of an electronic potential with a vibrational wave function. If one uses different vibrational wave functions, B_ν is different. In figure 4.15, B_ν is calculated using vibrational wave functions gained from the diabatic potentials A and b (black crosses) and vibrational wave functions gained by a coupled channel calculation, where the A and b state are coupled (red crosses). The lower lying line of black crosses describes B_ν of the A state. The higher lying line of black crosses describes B_ν of the b state. In figure 4.16 B_ν is calculated using vibrational wave functions gained from the adiabatic potentials $0_u^+(^2P_{1/2})$ (blue line) and $0_u^+(^2P_{3/2})$

(black line) and vibrational wave functions gained by a coupled channel calculation, where the $0_u^+(^2P_{1/2})$ state and the $0_u^+(^2P_{1/2})$ state are coupled. In figure 4.15 and figure 4.16, the coupled channel calculations lead to the same results of B_ν . This is because the vibrational state with which B_ν is calculated is the same in both figures. Coupling the A state and the b state or the $0_u^+(^2P_{1/2})$ state and $0_u^+(^2P_{3/2})$ state is only a different representation of the basis that is used in the coupled potential calculations. Where the coupled potential calculations and the single potential calculations lead to the same result of B_ν , the coupled vibrational wave function is formed purely by one state. For energies much smaller than -5500cm^{-1} relative to the $\text{Cs}_2(6s^2S_{1/2}+6p^2P_{3/2})$ dissociation limit, the coupled potential calculation, the calculations with the b state potential as well as the calculations with the $0_u^+(^2P_{1/2})$ state potential are almost the same. Thus, one can conclude that the coupling is negligible and the electronic $0_u^+(^2P_{1/2})$ state is formed entirely by the b state.

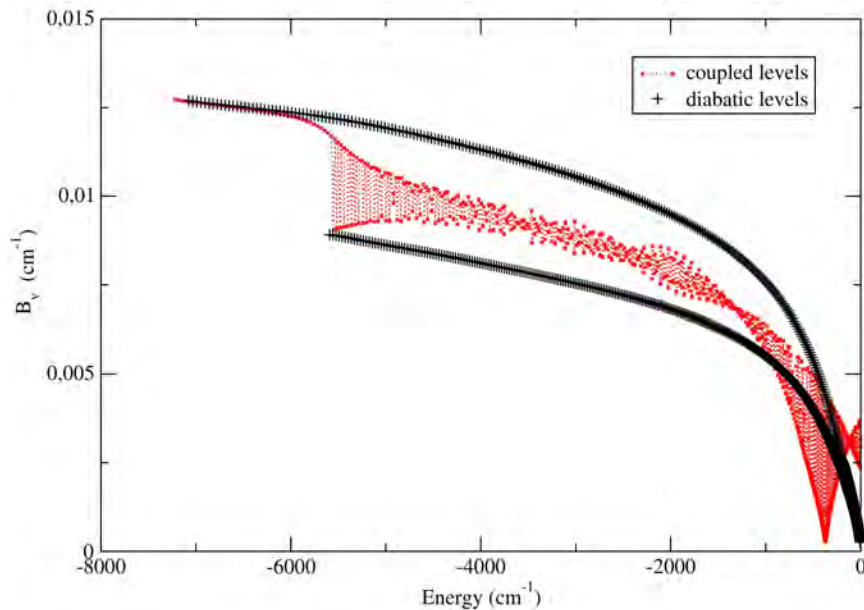


Figure 4.15: **Rotational Constant B_ν calculated with vibrational wave functions of the A and the b potentials and vibrational wave functions obtained by coupling the A and the b potential.** The lower series of black crosses shows the values of B_ν calculated with vibrational wave functions of the A potential. The upper series of black crosses shows results of B_ν when only the b potential is used in the calculation. The red crosses indicate the values of B_ν for vibrational wave functions obtained from coupling the A and the b potentials.

Secondly, the effect of the avoided crossing between the $0_u^+(^2P_{1/2})$ and the $0_u^+(^2P_{3/2})$ potentials is also important. Due to the avoided crossing the $0_u^+(^2P_{1/2})$ potential and the 0_u^- potential are separated more and more as R increases. At small internuclear separations, the 0_u^- hyperfine states are the main perturbers of the $0_u^+(^2P_{1/2})$ states and mostly responsible for the structure of the hyperfine splitting. Due to larger separations, second order perturbation effects decrease and consequently also the hyperfine splitting.

At larger internuclear distances ($R > 20a_0$) the magnitude of the hyperfine splitting increases again. All $\text{Cs}_2(6s+6p)$ potentials come closer to each other since electrostatic forces decrease for larger values of R . Therefore, the hyperfine states generally perturb each other more.

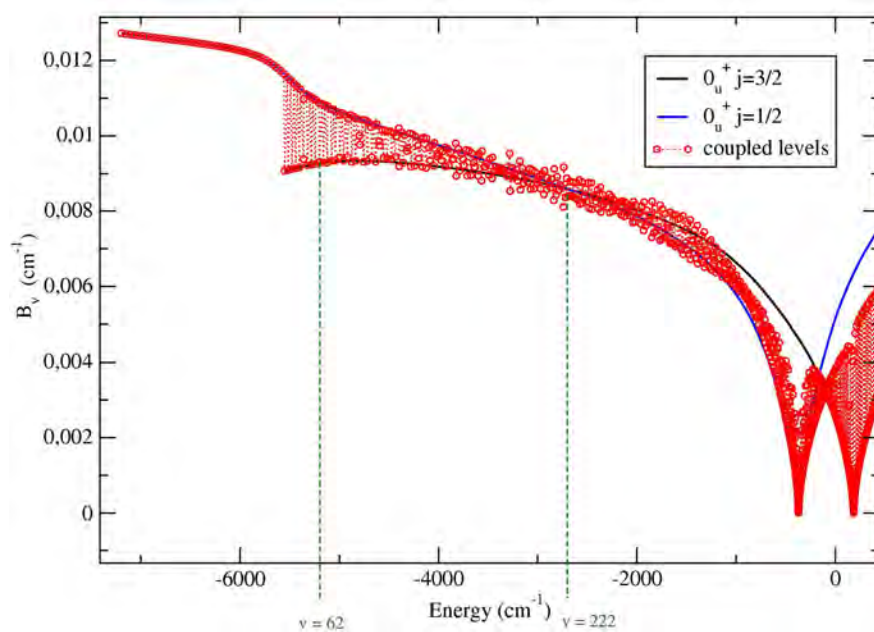


Figure 4.16: **Rotational Constant** B_ν calculated with vibrational wave functions of the $0_u^+(^2P_{1/2})$ potential (blue line), the $0_u^+(^2P_{3/2})$ potential (black line) and wave functions gained by coupling of $0_u^+(^2P_{1/2})$ and $0_u^+(^2P_{3/2})$ vibrational wave functions (red circles). From this figure and figure 4.15 we can conclude that the $0_u^+(^2P_{1/2})$ state is formed predominantly by the b state for energies smaller than -5500 cm^{-1} . This is because in this energy region the coupled channel calculations and the single channel calculations with the b and the $0_u^+(^2P_{1/2})$ potentials give approximately the same results for B_ν .

Hyperfine structure of the $0_u^+(^2P_{3/2})$ potential

In contrast to the latter case of $0_u^+(^2P_{1/2})$, the hyperfine structure of $0_u^+(^2P_{3/2})$ is more complicated because the $0_u^+(^2P_{3/2})$ adiabatic potential performs six crossings with other adiabatic potentials as seen in figure 4.17. The blue curve in figure 4.17 is the $0_u^+(^2P_{3/2})$ potential. It crosses the 2_u potential at $R = 10.6a_0$ (inset a), the $1_u(^2P_{1/2})$ at $R = 11.14a_0$ (inset b), the $1_g(^2P_{1/2})$ potential at $R = 13.98a_0$ (inset c), the $0_g^-(^2P_{1/2})$ potential at $R = 14.02a_0$ (inset c), the $1_u(^2P_{1/2})$ potential at $R = 17.84a_0$ (inset d) and finally the $0_g^-(^2P_{1/2})$ potential at $R = 22.49a_0$ (inset e).

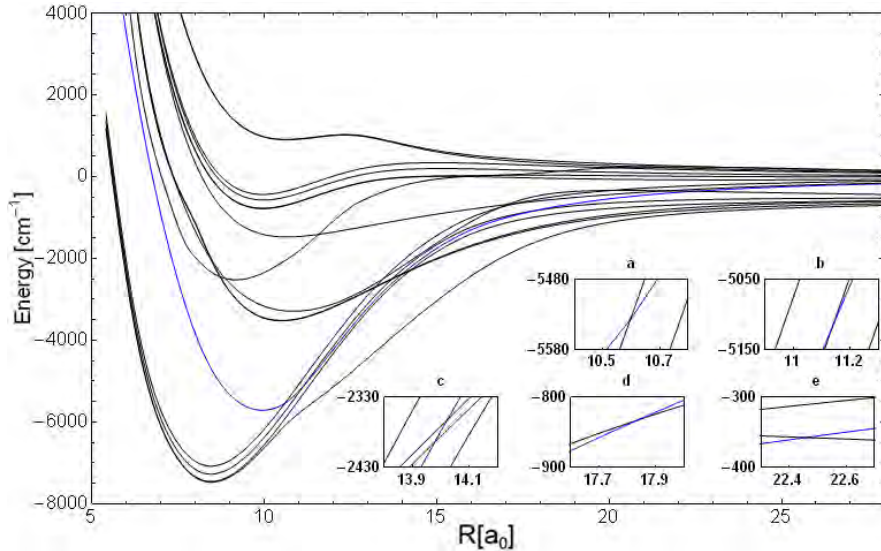


Figure 4.17: **Adiabatic potentials from $5a_0$ up to $30a_0$.** The blue line is the electronic potential of $0_u^+(^2P_{3/2})$. The insets a-e show the various crossings of the $0_u^+(^2P_{3/2})$ line with the 2_u potential at $R = 10.6a_0$ (inset a), the $1_u(^2P_{1/2})$ at $R = 11.14a_0$ (inset b), the $1_g(^2P_{1/2})$ potential at $R = 13.98a_0$ (inset c), the $0_g^-(^2P_{1/2})$ potential at $R = 14.02a_0$ (inset c), the $1_u(^2P_{1/2})$ potential at $R = 17.84a_0$ (inset d) and finally the $0_g^-(^2P_{1/2})$ potential at $R = 22.49a_0$ (inset e).

When hyperfine interactions are included, Ω and the eigenvalues of the g/u symmetry-operator cease being good quantum numbers. As a result, the hyperfine potentials anticross where the adiabatic potentials make a real crossing (as seen in figure 4.17). If we follow the hyperfine structure of $0_u^+(^2P_{3/2})$ adiabatically, starting from short nuclear separations, we change due to the avoided crossing to the hyperfine structure of another adiabatic potential. Close to an avoided crossing, the hyperfine potentials cannot be assigned to the hyperfine structure of only one of the adiabatic potentials that perform the anticrossing. During the avoided crossings the hyperfine potentials change adiabatically from the hyperfine structure of one specific adiabatic potential to the other. Figure 4.18 illustrates this fact. It shows a zoom on the avoided crossing between the $0_u^+(^2P_{3/2})$ hyperfine potentials and the $1_u(^2P_{1/2})$ hyperfine potentials around $R = 17.84a_0$. When we follow the hyperfine potentials of $0_u^+(^2P_{3/2})$ adiabatically starting from the left (All hyperfine potentials that form the hyperfine structure of $0_u^+(^2P_{3/2})$ on the left side of the avoided crossing are drawn in black.) we change within $0.01a_0$ to the hyperfine structure of $1_u(^2P_{1/2})$. The maximum hyperfine splitting of the $0_u^+(^2P_{3/2})$ potential before the crossing is rather small, approximately 15 MHz, whereas the maximum hyperfine splitting of the $1_u(^2P_{1/2})$ potential after the avoided crossing is about 5 GHz, more than 100 times larger. The result is an increase of the hyperfine splitting.

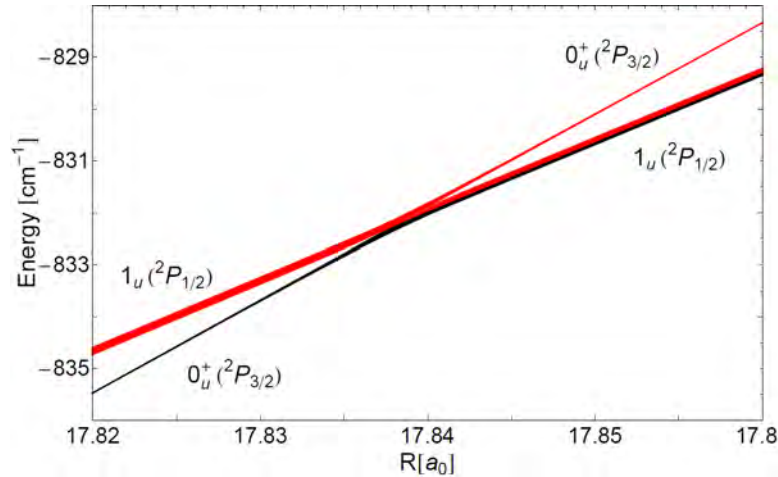


Figure 4.18: **Avoided crossing between the $0_u^+(^2P_{3/2})$ hyperfine potentials and the $1_u(^2P_{1/2})$ potentials at internuclear separations of about $17.84a_0$.** Hyperfine potentials that belong on the left side of the avoided crossing to the hyperfine structure of the $1_u(^2P_{1/2})$ adiabatic potential are plotted in red and hyperfine potentials that belong to the hyperfine structure of the $0_u^+(^2P_{3/2})$ adiabatic potential are plotted in black. In the central region of the avoided crossing hyperfine potentials can couple and thus, hyperfine potentials cannot be counted to the hyperfine structure of a specific adiabatic potential. On the right side of the avoided crossing one sees that the hyperfine structure of the $0_u^+(^2P_{3/2})$ adiabatic potential is formed by hyperfine potentials that belonged before the avoided crossing to the hyperfine structure of the $1_u(^2P_{1/2})$ adiabatic potential (red lines). The hyperfine structure of $1_u(^2P_{1/2})$ is formed by red and black lines on the right of the avoided crossing.

In figure 4.19 we show a plot of the hyperfine potentials that form the hyperfine structure of the $0_u^+(^2P_{3/2})$ adiabatic potential. The hyperfine potentials are plotted relative to the line that results from taking the average of all the hyperfine potentials that form the hyperfine structure of $0_u^+(^2P_{3/2})$.

Two developments are observable. First, there are three local peaks visible. The peaks are results of the avoided crossings between the hyperfine potentials of different adiabatic potentials. Due to the small separations between the curves, second order perturbation effects lead to a strong increase of the hyperfine structure. Moreover, as explained before in the discussion of the avoided crossing between the $0_u^+(^2P_{3/2})$ hyperfine potentials and the $1_u(^2P_{1/2})$ hyperfine potentials, the hyperfine potentials change their properties from one adiabatic potential to another. The hyperfine structure increases rapidly when the state after the crossing has a larger hyperfine structure than the state before the crossing. The peaks at $R = 10.6a_0$ and $R = 22.49a_0$ (see figure 4.17) cannot be seen in the plot, because they are too sharp. Also the two peaks at $R = 14a_0$ cannot be resolved individually. They lie too close to each other. The second development is a general increase of the hyperfine splitting from small to large nuclear separations. For $R < 10.6a_0$ the maximum splitting is about 0.5 MHz. Between the two large peaks it is approximately 10 MHz in magnitude, and for $R > 19a_0$ the maximum splitting increases strongly. The increase is a result of decreasing electrostatic interactions for larger values of R . The potentials move closer together and perturb each other more.

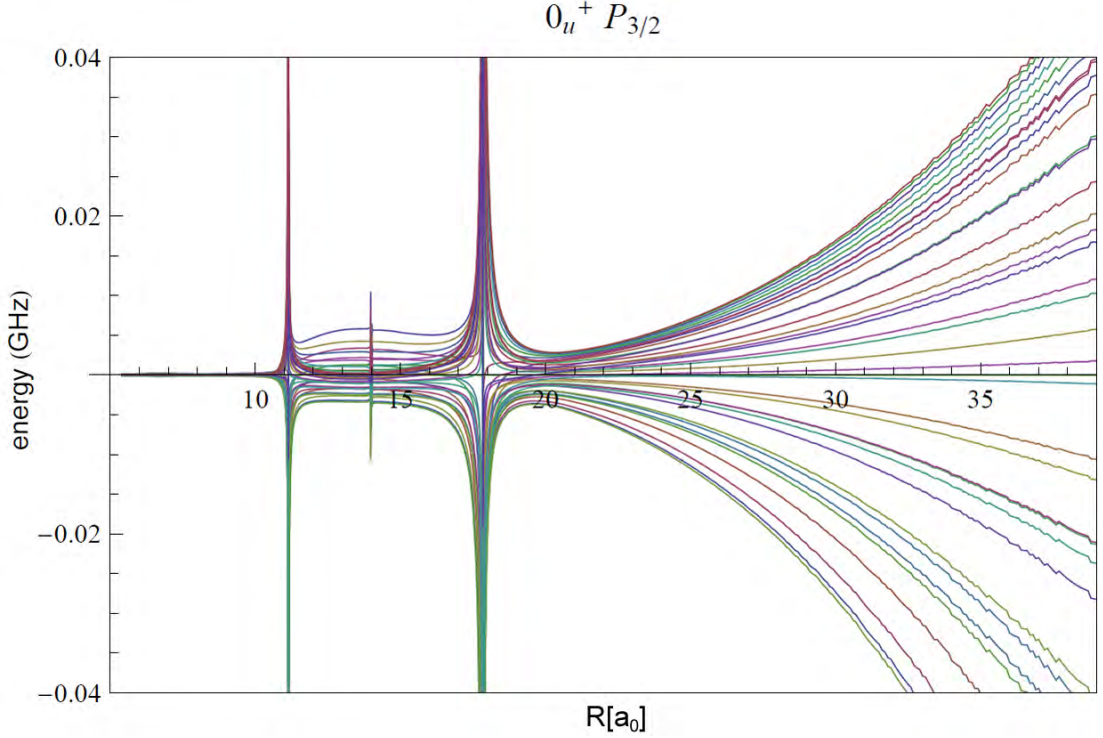


Figure 4.19: **Hyperfine potentials of the $0_u^+(^2P_{3/2})$ adiabatic potential.** The hyperfine potentials are plotted relative to the average line of all 36 hyperfine potentials.

4.3.3 Maximum Splitting

In this section we present the maximum splitting of the hyperfine structures of the $0_u^+(^2P_{1/2})$ potential and the $0_u^+(^2P_{3/2})$ potential as a function of the internuclear distance. The maximum splitting of the hyperfine structure at a specific value of R is given by the difference between the highest and the lowest line hyperfine potential. The plot for the maximum splitting of the two adiabatic potentials is shown in figure 4.20. In regions of avoided crossings, where one can not relate the hyperfine potentials to the hyperfine structure of a specific adiabatic potential, the plots are suppressed.

Using this figure, we can make a rough estimation of the hyperfine splitting of vibrational levels used in the STIRAP ground-state transfer. The energy of a vibrational state ν is the expectation value of an electronic potential averaged with the vibrational wave function of the state ν . Where the vibrational wave function is large, the weight of the potential in the calculation of the average value is higher. For vibrational levels far above the bottom of the electronic potential, the vibrational wave function is dominated by the vibrational energy at the Condon points. Thus, the hyperfine splitting of the electronic states at the Condon points dominates the hyperfine structure of vibrational energy levels. The maximum splitting of the hyperfine potentials at the Condon points is therefore providing a rough estimation of the hyperfine splitting of the vibrational levels.

The two used vibrational states with $\nu = 61$ and $\nu = 225$ as marked in figure 4.11 have right hand Condon points of $R_{1/2}^{61} = 11.9a_0$ and $R_{1/2}^{225} = 15.58a_0$ in the $0_u^+(^2P_{1/2})$ and $R_{3/2}^{61} = 11.04a_0$ and $R_{3/2}^{225} = 13.61a_0$ in the $0_u^+(^2P_{3/2})$ potential. For the $0_u^+(^2P_{1/2})$ potential, we get a maximum hyperfine splitting smaller than 1 MHz at both values of

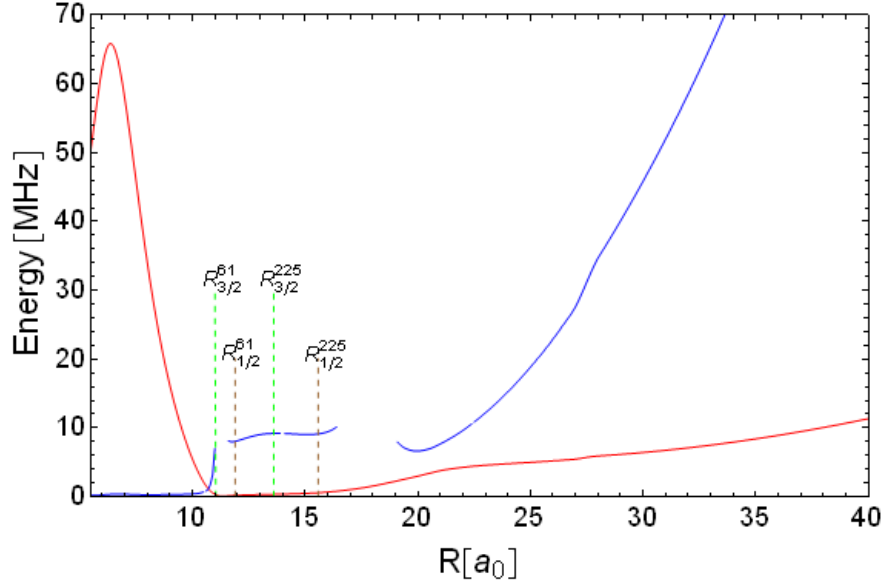


Figure 4.20: **Maximum splitting of the $0_u^+(^2P_{1/2})$ hyperfine potentials (red) and the $0_u^+(^2P_{3/2})$ hyperfine potentials (blue).** The plot is suppressed in regions of the avoided crossings, where one can not relate the hyperfine potentials to the hyperfine structure of a specific adiabatic potential.

R . For the $0_u^+(^2P_{3/2})$ potentials, we get a maximum hyperfine splitting of 7 MHz for $R^{61_{3/2}} = 11.0a_0$ and 9 MHz for $R^{225_{3/2}} = 13.61a_0$.

Maximum splitting of all adiabatic potentials

At this point, we also show the maximum hyperfine splitting as a function of R for all adiabatic potentials. The hyperfine potentials are plotted relative to the average line of all hyperfine potentials that form the considered hyperfine structure. In regions of the avoided crossings, where one can not relate the hyperfine potentials to the hyperfine structure of a specific adiabatic potential, we suppressed the plotting.

We find that the maximum hyperfine splitting differs much for the various states. States with $\Omega = 2$ and some states with $\Omega = 1$ have a large maximum hyperfine splitting that is close to 9 GHz for all values of R . Other states with $\Omega = 1$ show a stronger dependence on the internuclear distance but in general the maximum splitting is larger than 1 GHz. States that are described by $\Omega = 0$ show a very strong dependence on the internuclear distance. In general, these states have a small maximum hyperfine splitting (between 1 and 200 MHz). However, locally the splitting can be very large.

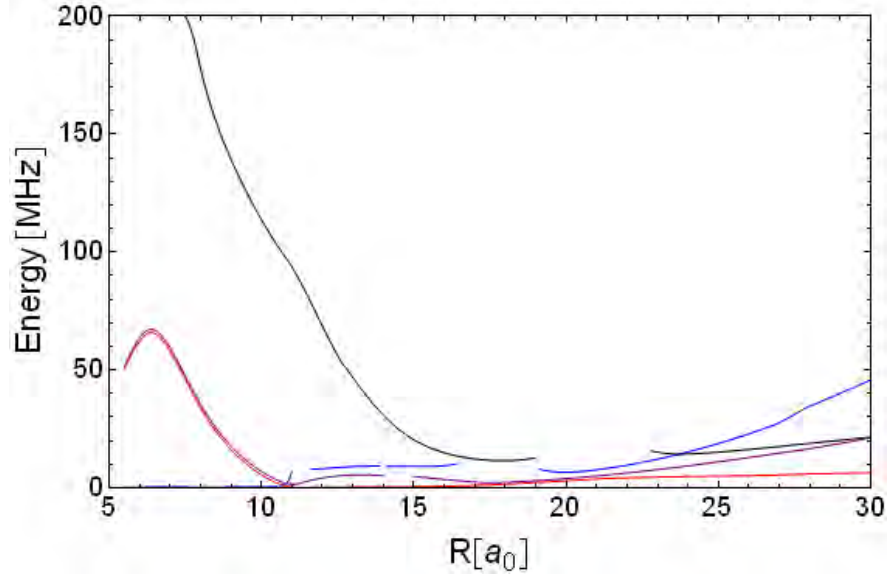


Figure 4.21: **Maximum splitting of the 0_u hyperfine potentials.** Displayed are the maximum splittings of the hyperfine structures of the $0_u^+(^2P_{1/2})$ (red), the $0_u^+(^2P_{3/2})$ (blue), the $0_u^-(^2P_{1/2})$ (purple) and the $0_u^-(^2P_{3/2})$ (black) adiabatic potentials.

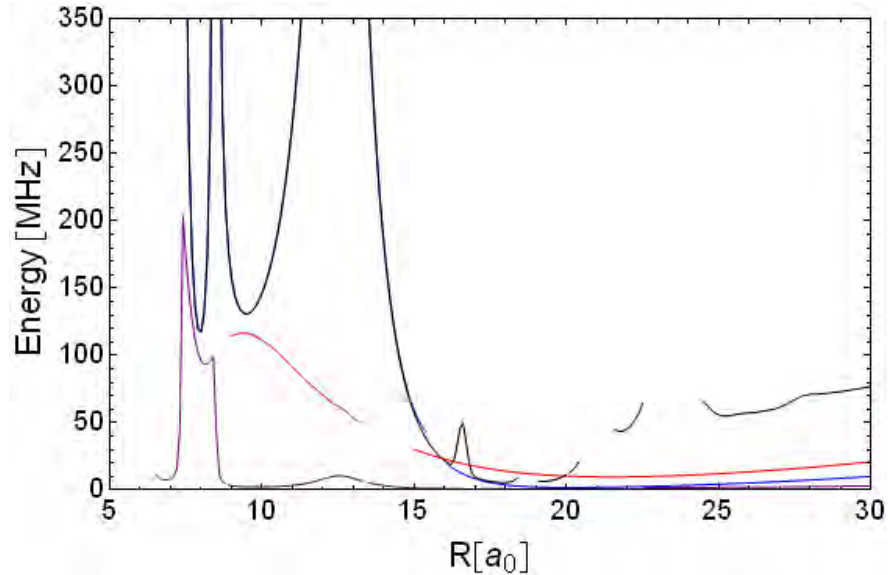


Figure 4.22: **Maximum splitting of the 0_g hyperfine potentials.** Displayed are the maximum splittings of the hyperfine structures of the $0_g^-(^2P_{1/2})$ (red), the $0_g^-(^2P_{3/2})$ (blue), the $0_g^+(^2P_{1/2})$ (purple) and the $0_g^+(^2P_{3/2})$ (black) adiabatic potentials.

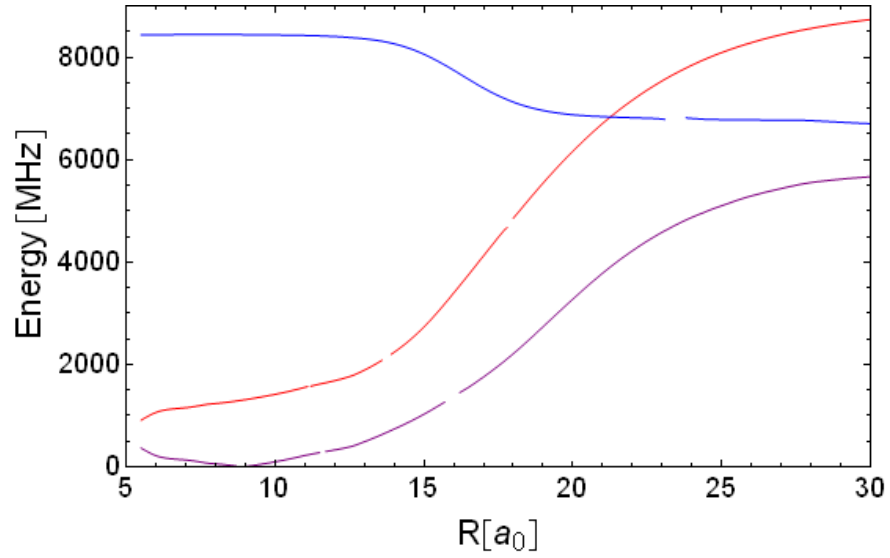


Figure 4.23: **Maximum splitting of the 1_u hyperfine potentials.** Displayed are the maximum splittings of the hyperfine structures of the $1_u(^2P_{1/2})(b)$ (red), the $1_u(^2P_{3/2})(b)$ (blue) and the $1_u(^2P_{3/2})(a)$ (purple) adiabatic potentials.

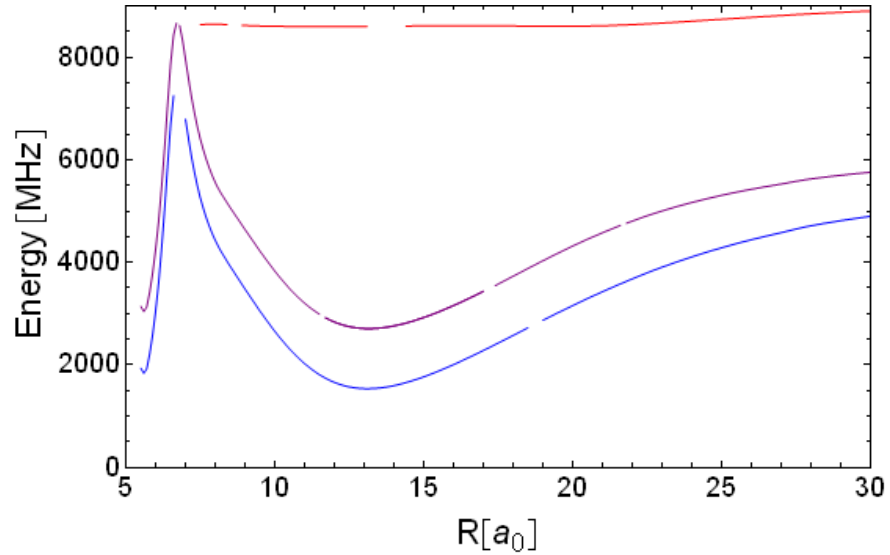


Figure 4.24: **Maximum splitting of the 1_g hyperfine potentials.** Displayed are the maximum splittings of the hyperfine structures of the $1_g(^2P_{1/2})(b)$ (red), the $1_g(^2P_{3/2})(a)$ (blue) and the $1_g(^2P_{1/2})(a)$ (purple) adiabatic potentials.

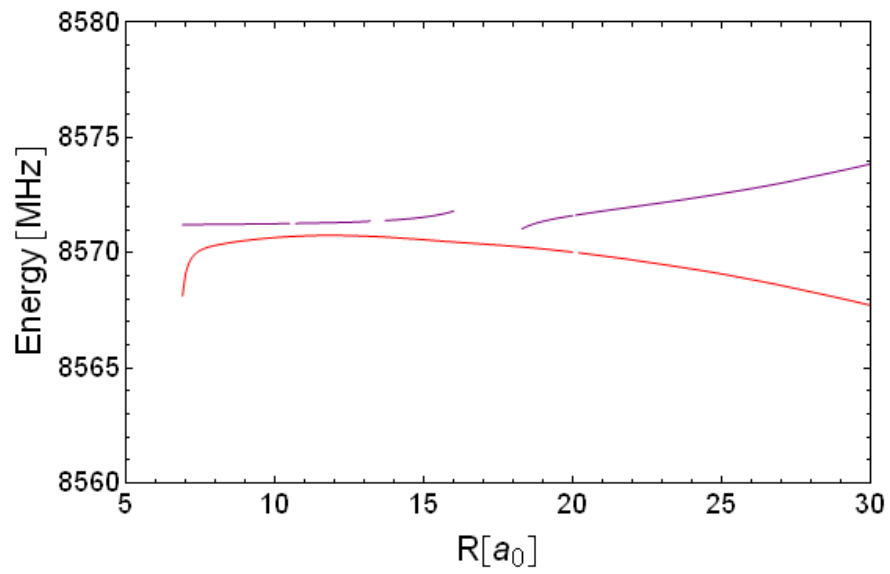


Figure 4.25: **Maximum splitting of the $\Omega = 2$ hyperfine potentials.** Displayed are the maximum splittings of the hyperfine structures of the 2_g (red) and the 2_u (purple) adiabatic potentials.

5 Perspectives

In the preceding chapters, we explain basic principles that are important for the understanding of our calculations on the molecular hyperfine structure. Moreover, the model that we use to calculate the hyperfine structure of the Cs_2 dimer in electronically excited states is presented in Chapter 3. Then, we also discuss and illustrate the results of our calculations. At the end of Chapter 4 we have seen that we expect a very small hyperfine splitting for rovibrational states of the $(A-b)0_u^+$ system. This is also in qualitative agreement with spectroscopic measurements, which reveal a hyperfine splitting of rovibrational states of the $(A-b)0_u^+$ system that should be smaller or on the same order of magnitude as our results (see Ref. [68] and Ref. [69]).

A small hyperfine splitting can lead to loss of state control. If one wants to populate a specific molecular hyperfine state, it is possible that transitions to several unwanted hyperfine states occur. This may also be problematic for the optimization of our STIRAP process. Of course, selection rules help to decrease the number of loss channels. Especially in the case of homonuclear diatomic molecules, where symmetry properties reduce the number of possible values for the nuclear spin quantum number, state control can be maintained due to selection rules to a high degree. In the case of heteronuclear molecules, no restriction for the nuclear spin exists. Thus, the number of states that can be unintentionally populated is increased. In order to better estimate possible difficulties that arise due to a small hyperfine structure more spectroscopic experiments have to be performed and a detailed comparison of spectroscopic data with our results is needed. However, also a more general theoretical treatment of the hyperfine structure of diatomic molecules has to be achieved.

In this final Chapter we describe some improvements to the presented calculations that can be made in order to compare the model with experimental data.

5.1 Variable Spin-Orbit Interaction

A first improvement of the calculations is obtained by considering a more complex model of the spin-orbit interaction. In our calculations we considered the spin-orbit interaction to be determined by the spin-orbit interaction of the atoms. Therefore, it is constant for every value of R . However, in a molecule the magnitude of the spin-orbit interaction, as the electronic potentials, is a function of the internuclear distance.

Romain Vexiau¹ has already implemented the variable spin-orbit interaction to simulate the coupling of the $A^1\Sigma_u^+$ and the $b^3\Pi_u$ potentials. The data that he uses to describe the variable spin-orbit interaction are taken from [90]. The spin-orbit interaction between all other potentials is still assumed to be constant. In figure 5.1 we show a plot of the hyperfine structure of the $0_u^+(^2P_{1/2})$ adiabatic potential with variable spin-orbit

¹Laboratoire Aimé Cotton

interaction. In the figure, the hyperfine potentials are plotted relative to the average line of all 36 hyperfine potentials of the $0_u^+(^2P_{1/2})$ hyperfine structure. If one compares figure 5.1 and figure 6.6, which shows the hyperfine structure of $0_u^+(^2P_{1/2})$ with constant spin-orbit interaction, one sees that the hyperfine splitting is generally larger for variable spin-orbit interaction. This is because the variable spin-orbit interactions are smaller in most regions than the constant spin-orbit interaction. Smaller spin-orbit interactions results in closer lying adiabatic potentials and thus the hyperfine potentials perturb each other stronger.

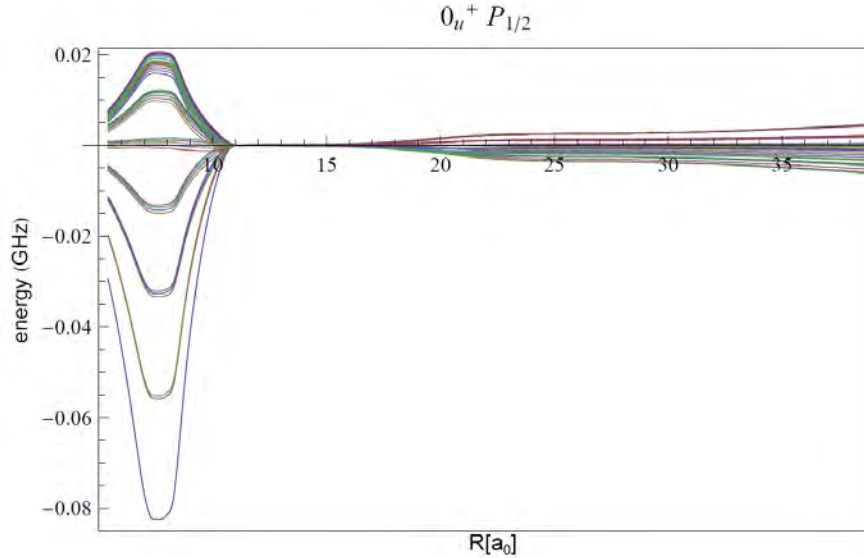


Figure 5.1: **Hyperfine potentials of the $0_u^+(^2P_{1/2})$ adiabatic potential with variable spin-orbit interaction.** The hyperfine potentials are plotted relative to the average of all hyperfine potentials that form the hyperfine structure of $0_u^+(^2P_{1/2})$.

5.2 Calculation of the Hyperfine Structure of Vibrational Levels

In section 2.3.5, we showed how vibrational levels are calculated. Romain Vexiau already used the hyperfine potentials to calculate the hyperfine structure of vibrational levels that are exploited in the ground-state transfer. In his approach, the hyperfine splitting of a vibrational level is calculated by perturbation theory. The perturbing term is the difference ΔV^i of a hyperfine potential and the adiabatic potential to whose hyperfine structure the hyperfine potential is counted. In first order perturbation theory, the unperturbed vibrational wave functions $|\Psi^\nu\rangle$ are used to average ΔV_i and thus hyperfine energy corrections ΔE^ν are calculated.

The vibrational wave functions of the $(A - b)0_u^+$ system are coupled vibrational wave functions. Ψ^ν is given by a linear combination of $\Psi_{1/2}^\nu$ and $\Psi_{3/2}^\nu$, which are vibrational wave functions of the $0_u^+(^2P_{1/2})$ adiabatic potential and the $0_u^+(^2P_{3/2})$ adiabatic potential respectively. The energy corrections ΔE^ν are calculated using a formula of the form:

$$\Delta E^\nu = \langle \Psi^\nu | \Delta V(R) | \Psi^\nu \rangle = \langle \Psi_{1/2}^\nu | \Delta V_{1/2}(R) | \Psi_{1/2}^\nu \rangle + \langle \Psi_{3/2}^\nu | \Delta V_{3/2}(R) | \Psi_{3/2}^\nu \rangle. \quad (5.1)$$

The vibrational wave functions of the levels $\nu = 62$ and $\nu = 225$ are plotted in figure 5.2. As an example for the results of the calculations, we show in figure 5.3 the hyperfine structure of the vibrational levels $\nu = 62$ and $\nu = 225$. Only 16 vibrational levels are seen because only levels with $\epsilon = +1$ are plotted. In all plots variable spin-orbit interaction is used.

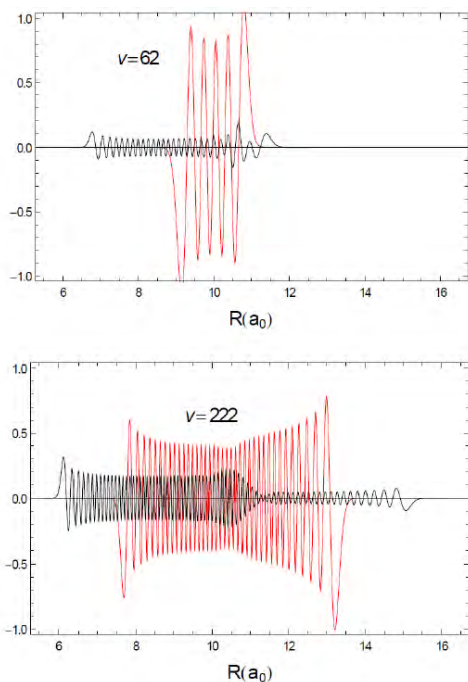


Figure 5.2: **The coupled vibrational wave function for vibrational levels $\nu = 62$ and $\nu = 225$.** The red (black) line indicates $\Psi_{3/2}^\nu$ ($\Psi_{1/2}^\nu$).

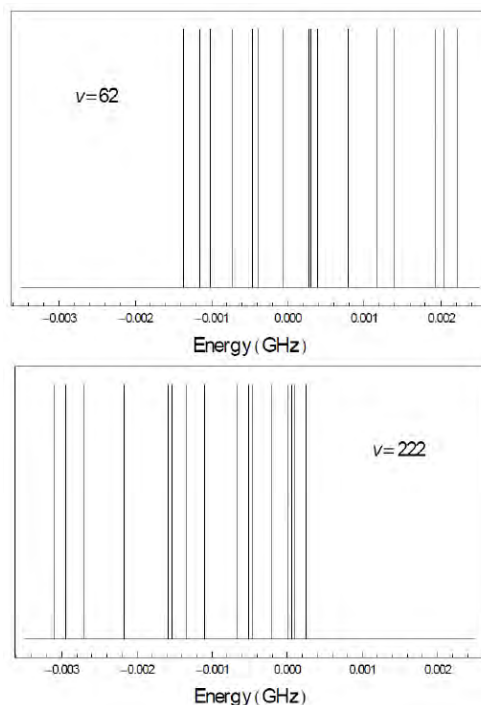


Figure 5.3: **Hyperfine structure of the $\nu = 62$ and $\nu = 225$ vibrational levels.**

5.3 Inclusion of Rotation and Magnetic Fields into the Calculations

In order to compare the results of the calculations with experimental data one also has to study the effect of hyperfine interaction simultaneously with the molecular rotation and the magnetic interaction. At the present, there is not much data at our hand with which to compare our calculations. One possible source is the high resolution spectroscopy data produced by our group [68]. Here, rovibrational levels of the $(A-b)0_u^+$ system and rovibrational levels of the $(1)^3\Sigma_g^+$ potential have been investigated. The used magnetic fields lie between 1.9 mT and 2.2 mT. The rovibrational states studied in the spectroscopic data are odd because in the rovibronic ground state $N = 0$ (even). (Optical transitions with linear polarized light allow only transitions that fulfill $\Delta N =$

± 1 .) To compare the data with results, at least the case of odd N has to be described by our calculations.

5.4 Comparison of the Results of the Model with Spectroscopic Data

Though we have not yet included rotational splitting and Zeeman splitting in our model we can conjecture about consequences of our findings for resolution requirements of spectroscopic experiments of the $(A - b)0_u^+$ state. The optical loss spectroscopy measurements presented in Ref. [68] could not resolve any hyperfine structure of the rovibronic state $(A - b)0_u^+$ ($\nu=225, N=1$) (The results for the experimental data is shown in figure 5.4.). Analysis of the measurements reveals a line width of the $(A - b)0_u^+$ ($\nu=225, N=1$) state of about 12 MHz. Our calculations predict that the maximum splitting of all 36 potentials that form the hyperfine structure of $(A - b)0_u^+$ is smaller than 9 MHz for the $(A - b)0_u^+$ ($\nu=225, N=0$) state (see section 4.3.3). Romain Vexiau's calculations for the $(A - b)0_u^+$ ($\nu=222, N=0$) state (section 5.2) show that the maximum splitting for states described by the quantum number $\epsilon = +1$ is about 3 MHz. Taking into account that the number of states will be largely increased when going from $N = 0$ to $N = 1$, it is possible that the resolution of the experiment, which has kHz precision, was not sufficient to resolve the hyperfine structure of the $(A - b)0_u^+$ ($\nu=225, N=1$) state. Further spectroscopy with higher resolution can answer this question. However, it is likely that the life time τ of the $(A - b)0_u^+$ ($\nu=225, N=1$) state leads to a natural line width $\Gamma = \frac{1}{\tau}$ that is larger than the hyperfine structure. In this case, one cannot resolve the hyperfine structure because it disappears in the natural line width. The natural line width of rovibronic levels is about 0.1-1000 MHz. If the natural line width is too large to resolve hyperfine structure, one can try to perform measurements at higher magnetic fields where the Zeeman splitting leads to a hyperfine splitting that exceeds the natural line width.

Ref. [68] also indicates that the hyperfine structure of the $(1)^3\Sigma_g^+$ can readily be resolved. Comparison with the hyperfine splitting of this state can give valuable information on the quality of our approximations.

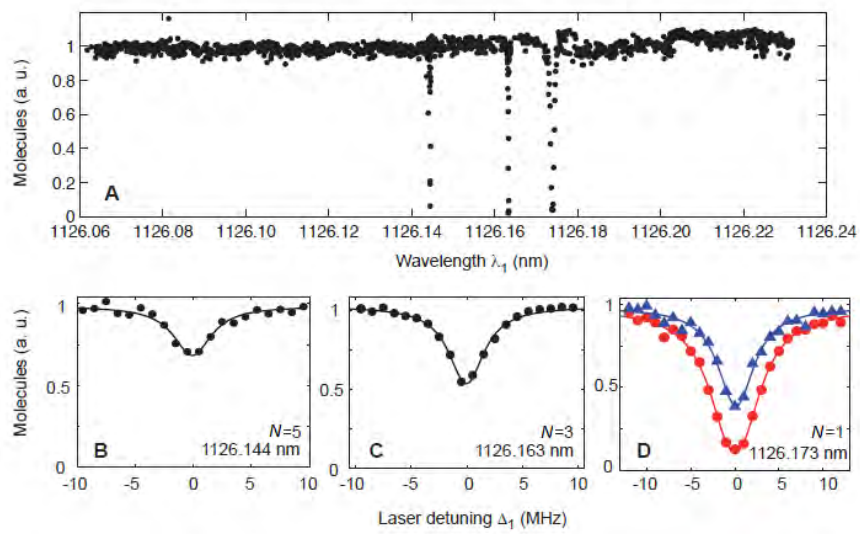


Figure 5.4: **Optical loss spectroscopy assigned to the $(A-b)0_u^+$ ($\nu=225$) state.** Panel **A** shows a coarse-grained scan over resonance lines of the $(A-b)0_u^+$ ($\nu=225$) state. The scan is performed near 1126 nm. The three resonances indicate transitions from the initial Feshbach molecule state to the rovibronic $(A-b)0_u^+$ ($\nu=225$, $N = 1, 3, 5$) states. Panel **B-D** show measurements with higher resolution of the resonances visible in **A**. The solid lines represent fits to determine Rabi frequencies and the life times. The two colors in Panel **D** indicate measurements for different laser intensities. Figure is taken from Ref. [68]

6 Appendix

6.1 Additional Relative Hyperfine Plots

The primary motivation for this thesis was the investigation of the hyperfine structure of molecular states that are exploited in our experiments of the ground-state transfer of molecules. These states belong to the $(A - b)0_u^+$ system. For this reason we discuss the hyperfine splitting of these states in detail. A detailed discussion of the hyperfine structure of other states would go beyond the scope of this thesis. However, we have also simulated the hyperfine splitting of all other potentials that dissociate to the $\text{Cs}_2(6s+6p)$ limit. We show the results of our calculations for all calculated states in this appendix in the form of figures in which the hyperfine potentials of a specific adiabatic potential are plotted relative to the average line of all hyperfine potential that form the considered hyperfine structure. Moreover we also give the number of hyperfine components of each considered potential.

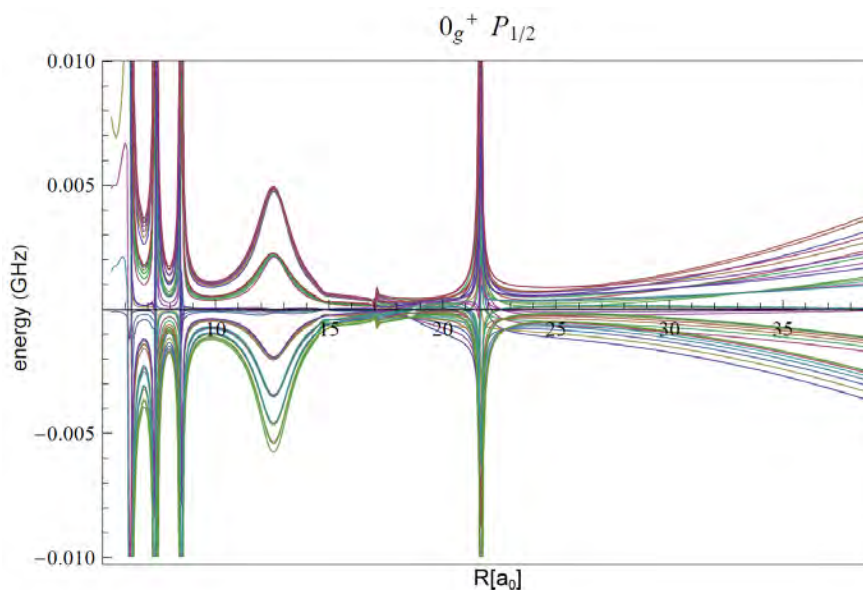


Figure 6.1: **Hyperfine potentials of the $0_g^+(^2P_{1/2})$ adiabatic potential.** The hyperfine structure is made up by 36 hyperfine potentials.

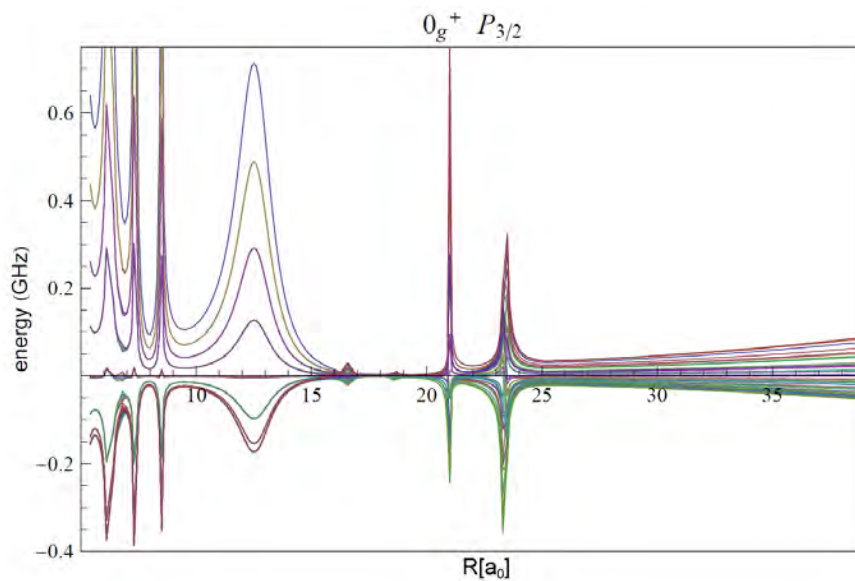


Figure 6.2: **Hyperfine potentials of the $0_g^+(^2P_{3/2})$ adiabatic potential.** The hyperfine structure is made up by 36 hyperfine potentials.

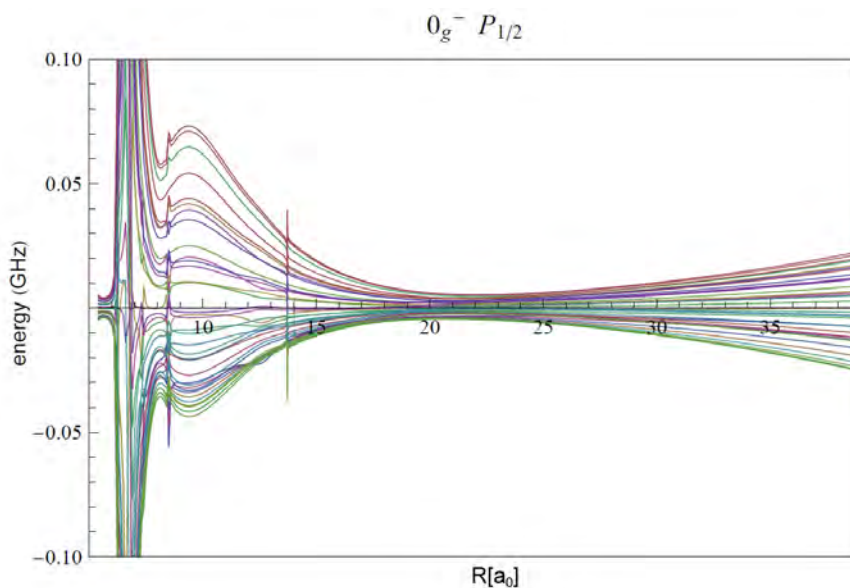


Figure 6.3: **Hyperfine potentials of the $0_g^-(^2P_{1/2})$ adiabatic potential.** The hyperfine structure is made up by 36 hyperfine potentials.

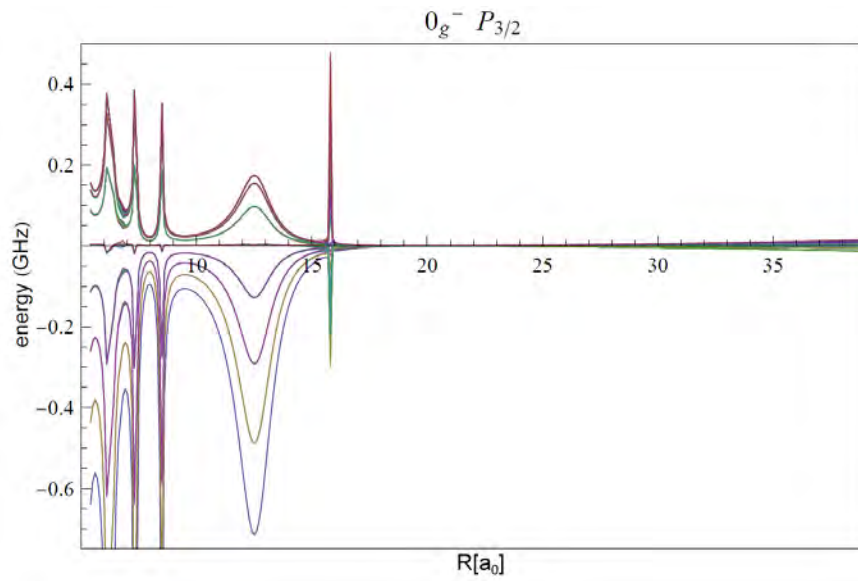


Figure 6.4: **Hyperfine potentials of the $0_g^- (^2P_{3/2})$ adiabatic potential.** The hyperfine structure is made up by 36 hyperfine potentials.

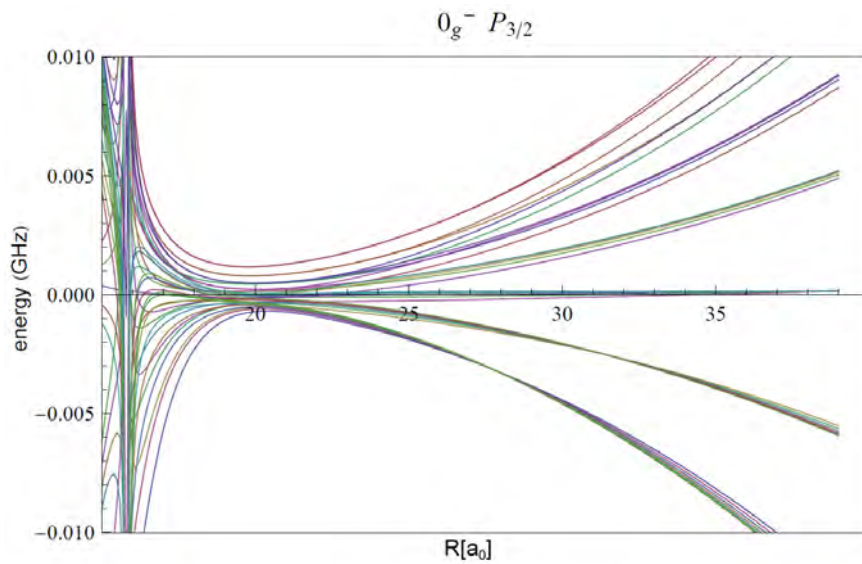


Figure 6.5: **Zoom on figure 6.4.**

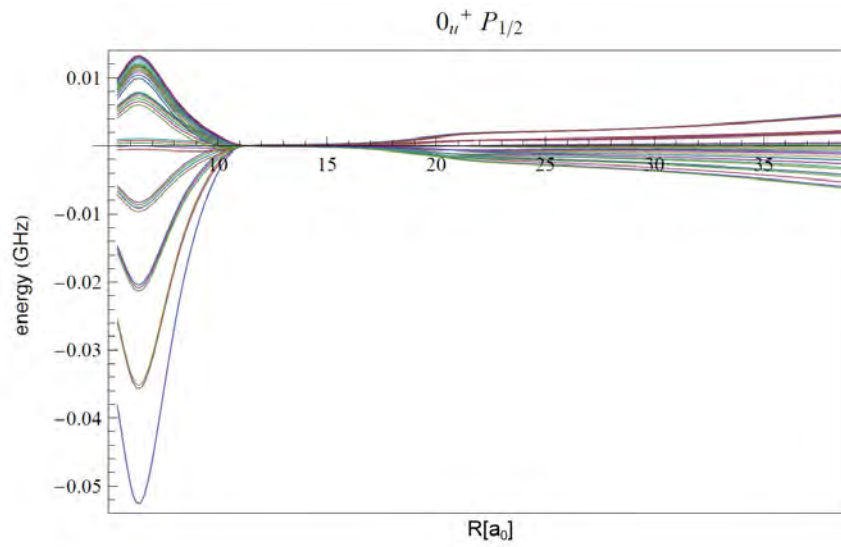


Figure 6.6: **Hyperfine potentials of the $0_u^+(^2P_{1/2})$ adiabatic potential.** The hyperfine structure is made up by 36 hyperfine potentials.

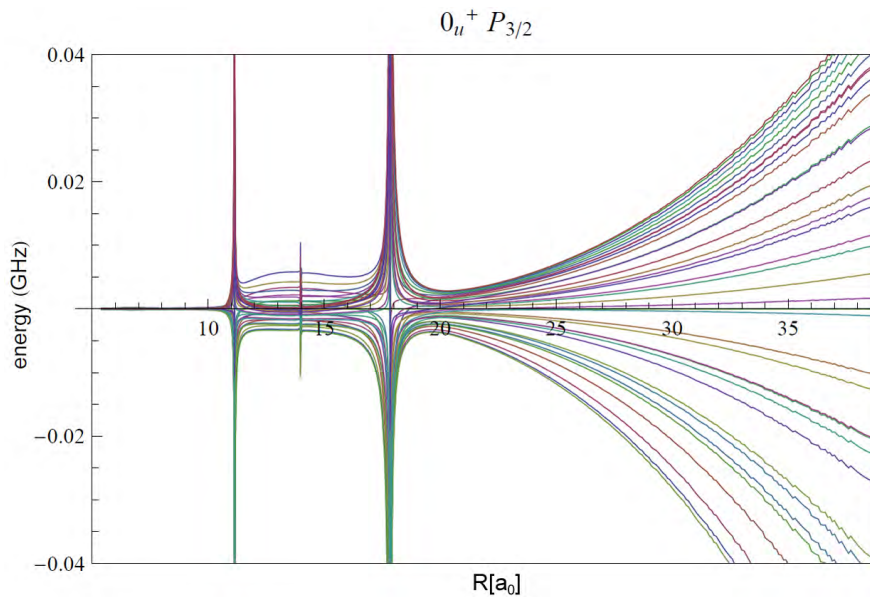


Figure 6.7: **Hyperfine potentials of the $0_u^+(^2P_{3/2})$ adiabatic potential.** The hyperfine structure is made up by 36 hyperfine potentials.

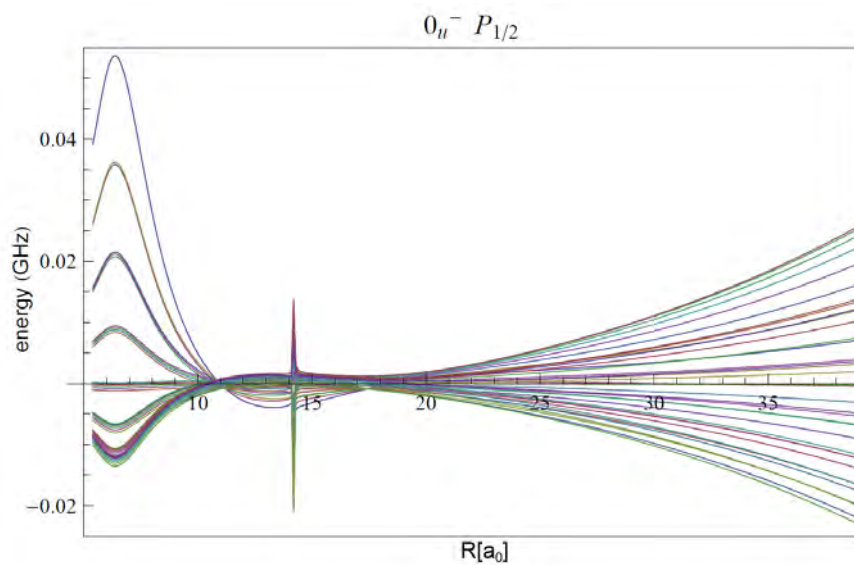


Figure 6.8: **Hyperfine potentials of the $0_u^- (^2P_{1/2})$ adiabatic potential.** The hyperfine structure is made up by 36 hyperfine potentials.

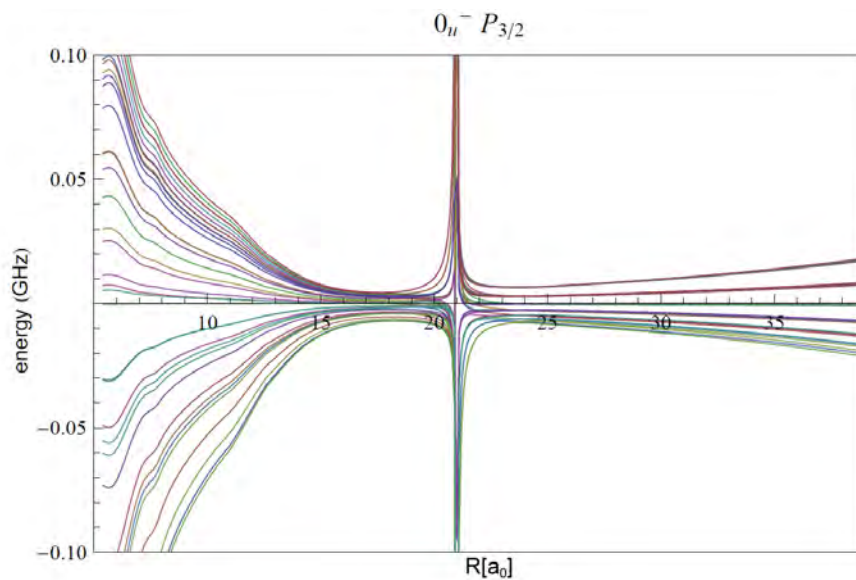


Figure 6.9: **Hyperfine potentials of the $0_u^- (^2P_{3/2})$ adiabatic potential.** The hyperfine structure is made up by 36 hyperfine potentials.

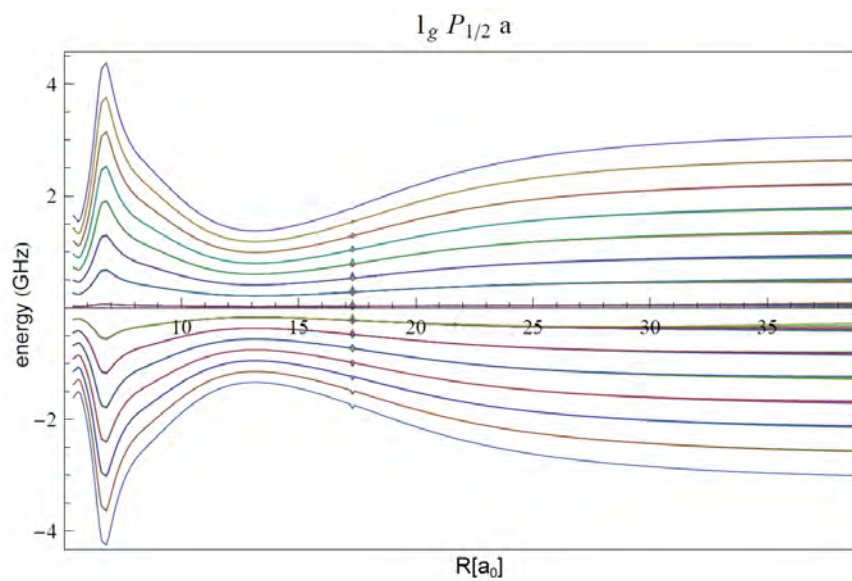


Figure 6.10: **Hyperfine potentials of the $1_g(^2P_{1/2})(a)$ adiabatic potential.** The hyperfine structure is made up by 71 hyperfine potentials.

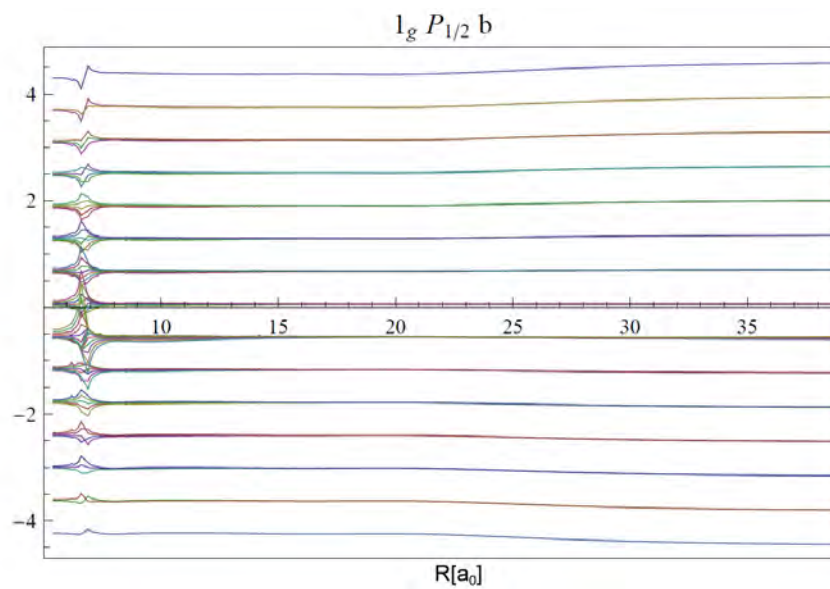


Figure 6.11: **Hyperfine potentials of the $1_g(^2P_{1/2})(b)$ adiabatic potential.** The hyperfine structure is made up by 71 hyperfine potentials.

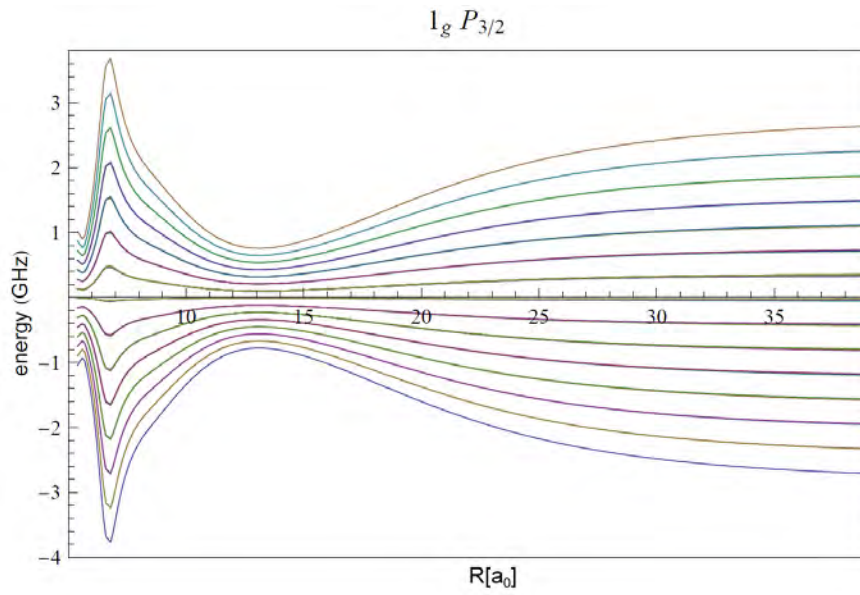


Figure 6.12: **Hyperfine potentials of the $1_g(^2P_{3/2})$ adiabatic potential.** The hyperfine structure is made up by 71 hyperfine potentials.

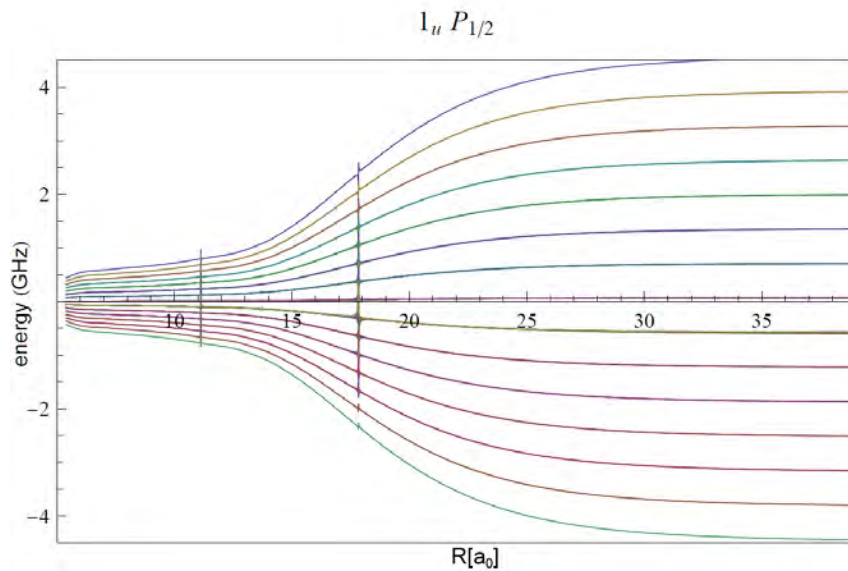


Figure 6.13: **Hyperfine potentials of the $1_u(^2P_{1/2})$ adiabatic potential.** The hyperfine structure is made up by 71 hyperfine potentials.

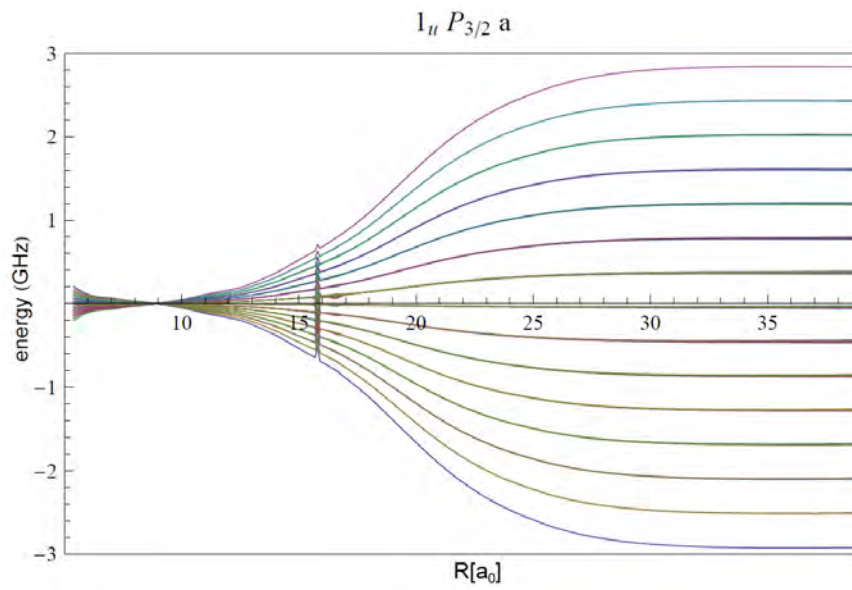


Figure 6.14: **Hyperfine potentials of the $1_u(^2P_{3/2})(a)$ adiabatic potential.** The hyperfine structure is made up by 71 hyperfine potentials.

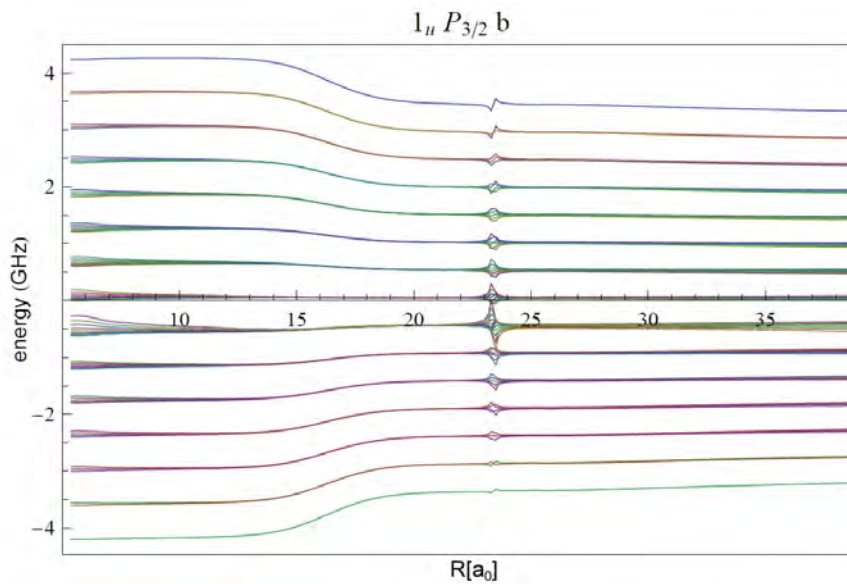


Figure 6.15: **Hyperfine potentials of the $1_u(^2P_{3/2})(b)$ adiabatic potential.** The hyperfine structure is made up by 71 hyperfine potentials.

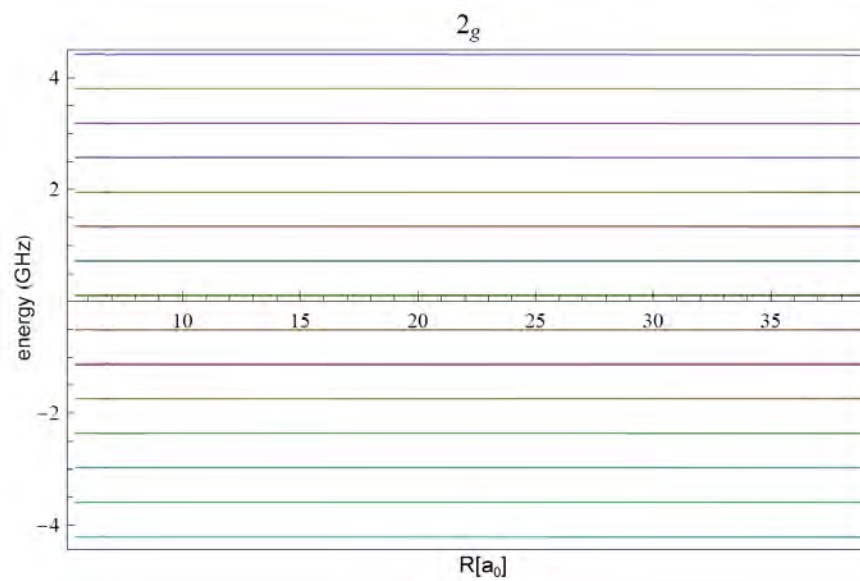


Figure 6.16: **Hyperfine potentials of the 2_g adiabatic potential.** The hyperfine structure is made up by 70 hyperfine potentials.

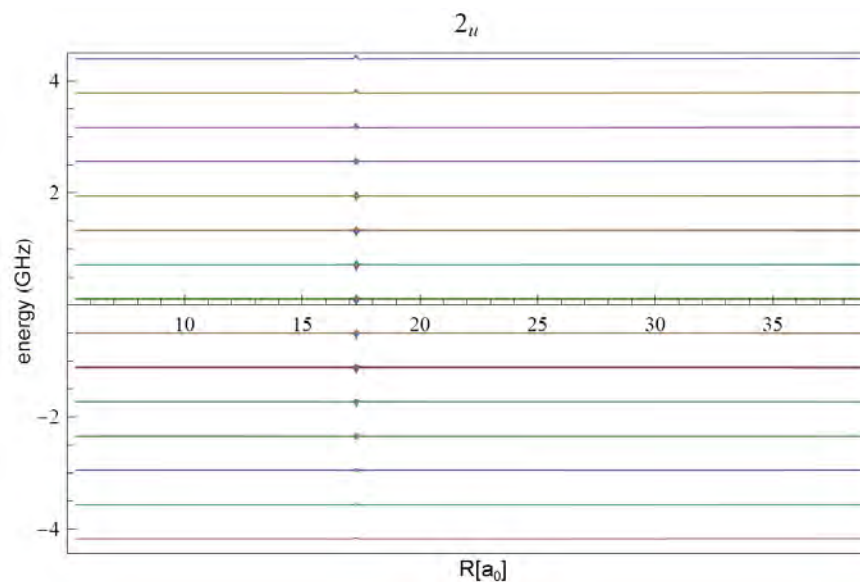


Figure 6.17: **Hyperfine potentials of the 2_u adiabatic potential.** The hyperfine structure is made up by 70 hyperfine potentials.

Bibliography

- [1] J. J. Hudson, B. E. Sauer, M. R. Tarbutt, and E. A. Hinds. Measurement of the electron electric dipole moment using YbF molecules. *Phys. Rev. Lett.*, 89:023003, 2002.
- [2] Eric R. Hudson, H. J. Lewandowski, Brian C. Sawyer, and Jun Ye. Cold molecule spectroscopy for constraining the evolution of the fine structure constant. *Phys. Rev. Lett.*, 96:143004, 2006.
- [3] C. Chin and V.V. Flambaum. Enhanced sensitivity to fundamental constants in ultracold atomic and molecular systems near Feshbach resonances. *Phys. Rev. Lett.*, 96:230801, 2006.
- [4] T. Zelevinsky, S. Kotochigova, and J. Ye. Precision test of mass-ratio variations with lattice-confined ultracold molecules. *Phys. Rev. Lett.*, 100:43201, 2008.
- [5] S. Schiller and V. Korobov. Tests of time independence of the electron and nuclear masses with ultracold molecules. *Phys. Rev. A*, 71:032505, 2005.
- [6] D. DeMille, S. Sainis, J. Sage, T. Bergeman, S. Kotochigova, and E. Tiesinga. Enhanced sensitivity to variation of m_e/m_p in molecular spectra. *Phys. Rev. Lett.*, 100:43202, 2008.
- [7] R. V. Krems. Cold controlled chemistry. *Phys. Chem. Chem. Phys.*, 10:4079, 2008.
- [8] K. Góral, L. Santos, and M. Lewenstein. Quantum phases of dipolar bosons in optical lattices. *Phys. Rev. Lett.*, 88:170406, 2002.
- [9] D. DeMille. Quantum computation with trapped polar molecules. *Phys. Rev. Lett.*, 88:67901, 2002.
- [10] A. André, D. DeMille, J.M. Doyle, M.D. Lukin, S.E. Maxwell, P. Rabl, R.J. Schoelkopf, and P. Zoller. A coherent all-electrical interface between polar molecules and mesoscopic superconducting resonators. *Nature Phys.*, 2:636, 2006.
- [11] P. Rabl, D. DeMille, J. M. Doyle, M. D. Lukin, R. J. Schoelkopf, and P. Zoller. Hybrid quantum processors: Molecular ensembles as quantum memory for solid state circuits. *Phys. Rev. Lett.*, 97:33003, 2006.
- [12] J. Doyle, B. Friedrich, R. V. Krems, and F. Masnou-Seeuws. Quo vadis, cold molecules? *Eur. Phys. J. D*, 31(2):149, 2004.
- [13] L. D. Carr, D. DeMille, R. V. Krems, and J. Ye. Cold and ultracold molecules: Science, technology and applications. *New J. Phys.*, 11:055049, 2009.
- [14] O. Dulieu and C. Gabbanini. The formation and interactions of cold and ultracold molecules: New challenges for interdisciplinary physics. *Rep. Prog. Phys.*, 72:086401, 2009.

- [15] B. Friedrich and J. M. Doyle. Why are cold molecules so hot? *ChemPhysChem*, 10:604, 2009.
- [16] William D. Phillips. Nobel lecture: Laser cooling and trapping of neutral atoms. *Rev. Mod. Phys.*, 70:721, 1998.
- [17] N. Masuhara, J. M. Doyle, J. C. Sandberg, D. Kleppner, T. J. Greytak, H. F. Hess, and Greg P. Kochanski. Evaporative cooling of spin-polarized atomic hydrogen. *Phys. Rev. Lett.*, 61:935, 1988.
- [18] M. H. Anderson, J. R. Ensher, M. R. Matthews, C. E. Wieman, and E. A. Cornell. Observation of Bose-Einstein condensation in a dilute atomic vapor. *Science*, 269:198, 1995.
- [19] K. B. Davis, M. O. Mewes, M. R. Andrews, N. J. Van Druten, D. S. Durfee, D. M. Kurn, and W. Ketterle. Bose-Einstein condensation in a gas of sodium atoms. *Phys. Rev. Lett.*, 75:3969, 1995.
- [20] K. W. Madison, F. Chevy, W. Wohlleben, and J. Dalibard. Vortex formation in a stirred Bose-Einstein condensate. *Phys. Rev. Lett.*, 84:806, 2000.
- [21] J. R. Abo-Shaeer, C. Raman, J. M. Vogels, and W. Ketterle. Observation of vortex lattices in Bose-Einstein condensates. *Science*, 292:476, 2001.
- [22] M. R. Andrews, C. G. Townsend, H. J. Miesner, D. S. Durfee, D. M. Kurn, and W. Ketterle. Observation of interference between two Bose condensates. *Science*, 275:637, 1997.
- [23] B. DeMarco and D.S. Jin. Onset of Fermi degeneracy in a trapped atomic gas. *Science*, 285:1703, 1999.
- [24] A.G. Truscott, K.E. Strecker, W.I. McAlexander, G.B. Partridge, and R.G. Hulet. Observation of Fermi pressure in a gas of trapped atoms. *Science*, 291:2570, 2001.
- [25] F. Schreck, L. Khaykovich, K. L. Corwin, G. Ferrari, T. Bourdel, J. Cubizolles, and C. Salomon. Quasipure Bose-Einstein condensate immersed in a Fermi sea. *Phys. Rev. Lett.*, 87:080403, 2001.
- [26] J. Bardeen, L. N. Cooper, and J. R. Schrieffer. Theory of superconductivity. *Phys. Rev.*, 108:1175, 1957.
- [27] H. T. C. Stoof, M. Houbiers, C. A. Sackett, and R. G. Hulet. Superfluidity of spin-polarized ${}^6\text{Li}$. *Phys. Rev. Lett.*, 76:10, 1996.
- [28] C. Chin, R. Grimm, P. Julienne, and E. Tiesinga. Feshbach resonances in ultracold gases. *Rev. Mod. Phys.*, 82:1225, 2010.
- [29] E. A. Donley, N. R. Clausen, S. T. Thompson, and C. E. Wieman. Atom-molecule coherence in a Bose-Einstein condensate. *Nature*, 417:529, 2002.
- [30] T. Bourdel, L. Khaykovich, J. Cubizolles, J. Zhang, F. Chevy, M. Teichmann, L. Tarruell, S. J. J. M. F. Kokkelmans, and C. Salomon. Experimental study of the BEC-BCS crossover region in lithium 6. *Phys. Rev. Lett.*, 93:050401, 2004.
- [31] M. Bartenstein, A. Altmeyer, S. Riedl, S. Jochim, C. Chin, J. Hecker Denschlag, and R. Grimm. Crossover from a molecular Bose-Einstein condensate to a degenerate Fermi gas. *Phys. Rev. Lett.*, 92:120401, 2004.

- [32] S. Jochim, M. Bartenstein, A. Altmeyer, G. Hendl, S. Riedl, C. Chin, J. Hecker Denschlag, and R. Grimm. Bose-Einstein condensation of molecules. *Science*, 302:2101, 2003.
- [33] T. Kraemer, M. Mark, P. Waldburger, J. G. Danzl, C. Chin, B. Engeser, A. D. Lange, K. Pilch, A. Jaakkola, H.-C. Nägerl, and R. Grimm. Evidence for Efimov quantum states in an ultracold gas of caesium atoms. *Nature*, 440:315, 2006.
- [34] I. Bloch. Ultracold quantum gases in optical lattices. *Nature Phys.*, 1:23, 2005.
- [35] D. Jaksch, C. Bruder, J. I. Cirac, C. W. Gardiner, and P. Zoller. Cold bosonic atoms in optical lattices. *Phys. Rev. Lett.*, 81:3108, 1998.
- [36] I. Bloch, J. Dalibard, and W. Zwerger. Many-body physics with ultracold gases. *Rev. Mod. Phys.*, 80:885, 2008.
- [37] M. Greiner, O. Mandel, T. Esslinger, T.W. Hänsch, and I. Bloch. Quantum phase transition from a superfluid to a Mott insulator in a gas of ultracold atoms. *Nature*, 415:39, 2002.
- [38] T. Stöferle, M. Henning, C. Schori, M. Köhl, and T. Esslinger. Transition from a strongly interacting 1D superfluid to a Mott insulator. *Phys. Rev. Lett.*, 92:130403, 2004.
- [39] I. B. Spielman, W. D. Phillips, and J. V. Porto. Mott insulator transition in a two-dimensional atomic Bose gas. *Phys. Rev. Lett.*, 98:080404, 2007.
- [40] R. Jördens, N. Strohmaier, K. Günter, H. Moritz, and T. Esslinger. A Mott insulator of fermionic atoms in an optical lattice. *Nature*, 455(7210):204, 2008.
- [41] T. Lahaye, C. Menotti, L. Santos, M. Lewenstein, and T. Pfau. The physics of dipolar bosonic quantum gases. *Rep. Prog. Phys.*, 72:126401, 2009.
- [42] H. P. Büchler, E. Demler, M. Lukin, A. Micheli, N. Prokof'ev, G. Pupillo, and P. Zoller. Strongly correlated 2D quantum phases with cold polar molecules: Controlling the shape of the interaction potential. *Phys. Rev. Lett.*, 98:060404, 2007.
- [43] A. Micheli, G. K. Brennen, and P. Zoller. A toolbox for lattice-spin models with polar molecules. *Nature Phys.*, 2:341, 2006.
- [44] Jean-Philippe Uzan. The fundamental constants and their variation: Observational and theoretical status. *Rev. Mod. Phys.*, 75:403, 2003.
- [45] S. Ospelkaus, K.K. Ni, D. Wang, M. H. G. De Miranda, B. Neyenhuis, G. Quémener, P. S. Julienne, J. L. Bohn, D. S. Jin, and J. Ye. Quantum-state controlled chemical reactions of ultracold potassium-rubidium molecules. *Science*, 327:853, 2010.
- [46] R. Barnett, D. Petrov, M. Lukin, and E. Demler. Quantum magnetism with multicomponent dipolar molecules in an optical lattice. *Phys. Rev. Lett.*, 96:190401, 2006.
- [47] E.S. Shuman, J.F. Barry, and D. DeMille. Laser cooling of a diatomic molecule. *Nature*, 467:820, 2010.
- [48] D. S. Petrov, C. Salomon, and G. V. Shlyapnikov. Weakly bound dimers of fermionic atoms. *Phys. Rev. Lett.*, 93:90404, 2004.

- [49] H. L. Bethlem, G. Berden, and G. Meijer. Decelerating neutral dipolar molecules. *Phys. Rev. Lett.*, 83:1558, 1999.
- [50] E. Narevicius, A. Libson, C. G. Parthey, I. Chavez, J. Narevicius, U. Even, and M. G. Raizen. Stopping supersonic oxygen with a series of pulsed electromagnetic coils: A molecular coilgun. *Phys. Rev. A*, 77:051401, 2008.
- [51] J. D. Weinstein, R. deCarvalho, T. Guillet, B. Friedrich, and Doyle J.M. Magnetic trapping of calcium monohydride molecules at millikelvin temperatures. *Nature*, 395(6698):148, 1998.
- [52] A. Fioretti, D. Comparat, A. Crubellier, O. Dulieu, F. Masnou-Seeuws, and P. Pillet. Formation of cold Cs_2 molecules through photoassociation. *Phys. Rev. Lett.*, 80:4402, 1998.
- [53] W. C. Stwalley, Y.-H. Uang, and G. Pichler. Pure long-range molecules. *Phys. Rev. Lett.*, 41:1164, 1978.
- [54] C. M. Dion, C. Drag, O. Dulieu, B. Laburthe Tolra, F. Masnou-Seeuws, and P. Pillet. Resonant coupling in the formation of ultracold ground state molecules via photoassociation. *Phys. Rev. Lett.*, 86:2253, 2001.
- [55] R. Wynar, R.S. Freeland, D.J. Han, C. Ryu, and D.J. Heinzen. Molecules in a Bose-Einstein condensate. *Science*, 287:1016, 2000.
- [56] J. Herbig, T. Kraemer, M. Mark, T. Weber, C. Chin, H.C. Nägerl, and R. Grimm. Preparation of a pure molecular quantum gas. *Science*, 301:1510, 2003.
- [57] M. W. Zwierlein, C. A. Stan, C. H. Schunck, S. M. F. Raupach, S. Gupta, Z. Hadzibabic, and W. Ketterle. Observation of Bose-Einstein condensation of molecules. *Phys. Rev. Lett.*, 91:250401, 2003.
- [58] K. Bergmann, H. Theuer, and B. W. Shore. Coherent population transfer among quantum states of atoms and molecules. *Rev. Mod. Phys.*, 70:1003, 1998.
- [59] A. D. Lercher, T. Takekoshi, M. Debatin, B. Schuster, R. Rameshan, F. Ferlaino, R. Grimm, and H. C. Nägerl. Production of a dual-species Bose-Einstein condensate of Rb and Cs atoms. *Eur. Phys. J. D*, page 1.
- [60] M. Debatin, T. Takekoshi, R. Rameshan, L. Reichsöllner, F. Ferlaino, R. Grimm, R. Vexiau, N. Bouloufa, O. Dulieu, and H. C. Nägerl. Molecular spectroscopy for ground-state transfer of ultracold RbCs molecules. *Phys. Chem. Chem. Phys.*, 2011.
- [61] K.K. Ni, S. Ospelkaus, M.H.G De Miranda, A. Pe'er, B. Neyenhuis, J.J. Zirbel, S. Kotochigova, P.S. Julienne, D.S. Jin, and J. Ye. A high phase-space density gas of polar molecules. *Science*, 322:231, 2008.
- [62] J. G. Danzl, M. J. Mark, E. Haller, M. Gustavsson, R. Hart, J. Aldegunde, J. M. Hutson, and H.-C. Nägerl. An ultracold high-density sample of rovibronic ground-state molecules in an optical lattice. *Nature Phys.*, 6:265, 2010.
- [63] H.-C. Nägerl, M.J. Mark, E. Haller, M. Gustavsson, R. Hart, and J.G. Danzl. Ultracold and dense samples of ground-state molecules in lattice potentials. *Journal of Physics: Conference Series*, 264:012015, 2011.

- [64] T. Volz, N. Syassen, D. M. Bauer, E. Hansis, S. Dürr, and G. Rempe. Preparation of a quantum state with one molecule at each site of an optical lattice. *Nature Phys.*, 2:692, 2006.
- [65] D. Jaksch, V. Venturi, J. I. Cirac, C. J. Williams, and P. Zoller. Creation of a molecular condensate by dynamically melting a Mott insulator. *Phys. Rev. Lett.*, 89:040402, 2002.
- [66] A. Klinger. Master thesis, 2011.
- [67] E. Kuznetsova, P. Pellegrini, R. Côté, M. D. Lukin, and S. F. Yelin. Formation of deeply bound molecules via chainwise adiabatic passage. *Phys. Rev. A*, 78:021402, 2008.
- [68] J.G. Danzl, M.J. Mark, E. Haller, M. Gustavsson, N. Bouloufa, O. Dulieu, H. Ritsch, R. Hart, and H.-C. Nägerl. Precision molecular spectroscopy for ground state transfer of molecular quantum gases. *Faraday Discuss.*, 142:283, 2009.
- [69] M.J. Mark, J.G. Danzl, E. Haller, M. Gustavsson, N. Bouloufa, O. Dulieu, H. Salami, T. Bergeman, H. Ritsch, R. Hart, and H.-C. Nägerl. Dark resonances for ground-state transfer of molecular quantum gases. *Appl. Phys. B.*, 95:219, 2009.
- [70] J. Aldegunde and J. M. Hutson. Hyperfine energy levels of alkali-metal dimers: Ground-state homonuclear molecules in magnetic fields. *Phys. Rev. A*, 79:013401, 2009.
- [71] M. Broyer, J. Vigué, and J. C. Lehmann. Effective hyperfine Hamiltonian in homonuclear diatomic molecules. Application to the B state of molecular iodine. *J. Phys. (Paris)*, 39:591, 1978.
- [72] W. Pauli. Zur frage der theoretischen Deutung der Satelliten einiger Spektrallinien und ihrer Beeinflussung durch magnetische Felder. *Naturwissenschaften*, 12:741, 1924.
- [73] E. Fermi. Über die magnetischen Momente der Atomkerne. *Phys. A*, 60:320, 1930.
- [74] R. A. Frosch and H. M. Foley. Magnetic hyperfine structure in diatomic molecules. *Phys. Rev.*, 88:1337, 1952.
- [75] L. D. Landau and E. M. Lifschitz. *Lehrbuch der theoretischen Physik, Bd.3, Quantenmechanik*. Wissenschaftlicher Verlag Harri Deutsch GmbH, 2007.
- [76] C. Cohen-Tannoudji, B. Diu, and F. Laloe. *Quantenmechanik, Teil 1*. Walter de Gruyter GmbH & Co. KG, 1999.
- [77] C. Cohen-Tannoudji, B. Diu, and F. Laloe. *Quantenmechanik, Teil 2*. Walter de Gruyter GmbH & Co. KG, 1999.
- [78] A.R. Edmonds. *Drehimpulse in der Quantenmechanik*. Bibliographisches Institut, 1964.
- [79] J.M. Brown and A. Carrington. *Rotational Spectroscopy of Diatomic Molecules*. Cambridge University Press, 2003.
- [80] G. Herzberg. *Molecular Spectra and Molecular Structure*. Van Nostrand Reinhold Company, 1950.

- [81] W. Demtröder. *Molecular physics: theoretical principles and experimental methods*. Wiley-VCH Verlag GmbH & Co.KGaA, 2005.
- [82] B. Ji, C.C. Tsai, and W.C. Stwalley. Proposed modification of the criterion for the region of validity of the inverse-power expansion in diatomic long-range potentials. *Chem. Phys. Lett.*, 236:242, 1995.
- [83] M. Marinescu and A. Dalgarno. Dispersion forces and long-range electronic transition dipole moments of alkali-metal dimer excited states. *Phys. Rev. A*, 52:311, 1995.
- [84] M. Marinescu and A. Dalgarno. Analytical interaction potentials of the long range alkali-metal dimers. *Z. Phys. D*, 36:239, 1996.
- [85] M. Blume and R. E. Watson. Theory of spin-orbit coupling in atoms. I. Derivation of the spin-orbit coupling constant. *P. Roy. Soc Lond. A Mat.*, 270:127, 1962.
- [86] J. Verges and C. Amiot. The Cs_2 $A^1\Sigma_u^+ \rightarrow X^1\Sigma_g^+$ fluorescence excited by the Ar^+ 1.09 μm laser line. *J. Mol. Spectrosc.*, 126:393, 1987.
- [87] F. Xie, D. Li, L. Tyree, L. Li, V. B. Sovkov, V. S. Ivanov, S. Magnier, and A.M. Lyyra. Observation and calculation of the Cs_2 $2^3\Delta_{1g}$ and $b^3\Pi_{0u}$ states. *J. Chem. Phys.*, 128:204313, 2008.
- [88] M. Aymar and O. Dulieu. Calculation of accurate permanent dipole moments of the lowest $1,3\Sigma^+$ states of heteronuclear alkali dimers using extended basis sets. *J. Chem. Phys.*, 122:204302, 2005.
- [89] U. Diemer, J. Gress, and W. Demtröder. The $2^3\Pi_g \leftarrow X^3\Sigma_u$ triplet system of Cs_2 . *Chem. Phys. Lett.*, 178:330, 1991.
- [90] N. Spies. Ph.D. thesis, 1989.

Danksagung

Am Ende will ich mich noch bei allen Menschen bedanken, die mich durch die vergangenen sieben Jahren des Studiums begleitet haben. Ich durfte mit euch eine wunderschöne Zeit erleben. Außerdem habt ihr mir unter die Arme gegriffen, wenn ich Hilfe benötigt habe. Ohne euch wäre ich nicht in der Lage gewesen diese Diplomarbeit zu schreiben.

An erster Stelle will ich mich bei meinem Betreuer Hanns-Christoph Nägerl bedanken. Er hat mich während der gesamten Zeit, in der ich unter ihm gearbeitet habe, gut unterstützt. Besonders bedanken will ich mich natürlich dafür, dass ich im Rahmen der Diplomarbeit nach Orsay fahren durfte! Weiters will ich mich bei Rudolf Grimm bedanken. Er hat unsere Forschungsgruppe aufgebaut und ist hauptverantwortlich dafür, dass die ultrakalten Quantengase in Innsbruck untersucht werden.

Außerdem will ich mich bei Olivier Dulieu, Nadia Bouloufa und Anne Crubellier für die Zeit in Orsay bedanken. En vous je n'ai pas trouvé seulement des bons enseignants, mais aussi des nouveaux amis! J'ai bien joui l'ambiance cordiale au LAC. Bien sûr, je veux remercier aussi les autres qui m'ont aidé au LAC. Merci Mireille, Maxence, Romain, Maurice,...

Dank gilt auch dem gesamten CsIII Team. Vor allem Johann Danzl, der Freund der guten Küche, der immer Zeit hatte, wenn ich mit Fragen zu ihm kam. Nicht vergessen will ich auch Lukas Reichsöllner, Elmar Haller, Manfred Mark, Mohamed Rabie und Andreas Klinger für die schöne Zeit in der Uni. Dank für einige willkommene Ablenkungen und viele Süßigkeiten gilt natürlich auch den Kollegen aus meinem Büro: Raffael Rameshan, Markus Debatin und Tetsu Takekoshi.

Jetzt ist es auch an der Zeit mich bei Daniel Nigg und Vinzenz Bittner zu bedanken. Mit Daniel habe ich mindestens 4.800 Praktikumsversuche und Sommerpraktika gemeistert. Vom ersten Tag an waren wir ein super Team. Wir konnten immer¹ aufeinander bauen. Mit Vinzenz bin ich in Anjuna Beach vor Hunden davon gelaufen und ich habe auch auf unzählige Prüfungen mit ihm gelernt. Ohne euch zwei wäre das mit Sicherheit ein ganz anderes Physikstudium gewesen. Motivation beim Lernen hat auch Daniel Hauser des öfteren gebracht. Zusammen bilden wir vier die *Banditos* (stimmts?). Einige der genialsten Abende in Innsbruck (vor allem 11er Haus) habe ich mit den Banditos verbracht. Danke auch an alle meine anderen Freunde für eine geniale Zeit!

Am meisten bedanken möchte ich mich bei meiner Familie - vor allem bei meinen Eltern. Danke.

¹Naja, Ok, bis auf einmal... aber wer will schon 500 PTR-MS Spektren auf einmal auswerten?-das kann man mir nicht vorwerfen...